UTTAC-70, 2002

ANNUAL REPORT

April 1,2001 – March 31, 2002

TANDEM ACCELERATOR CENTER
UNIVERSITY OF TSUKUBA

http://www.tac.tsukuba.ac.jp/

PREFACE

This annual report describes research activities in UTTAC during the period from April 2001 to March 2002. The 12 UD Pelletron tandem accelerator was successfully operated until the end of February 2002. Total beam time used for experiments was 1729 hours. This time is about 64 % of that in the last year. The decrease of the beam time was due to the fact that we were forced to stop the accelerator every weekend from the lack of manpower. The duoplasmatron source of the tandetron accelerator was improved to produce negative helium-ions more stably.

In nuclear physics, we obtained a new experimental data on the proton polarization in the ^{208}Pb(d,p)^{209}Pb$_{gs}$ reaction at 20 MeV, and on the analyzing powers in the ^{6}Li(d,p)^{7}Li reaction at 90 keV. Further investigation was made on the anomaly in the total-reaction cross section for protons on Si nuclei near the (p,n) threshold. An extension of our CDCC analysis yielded a new prediction of triple differential cross sections for the ^{208}Pb(d,pn) reaction at 56 MeV with polarized deuterons. Nuclear structure studies were performed on ^{116}I and ^{117}I. A polarized proton beam was applied to investigate the transient magnetic field applied on fast ions moving through magnetized foils.

Ion-induced secondary electron spectroscopy, atomic cluster physics, NMR studies on electronic states of 3*d* transition-metal oxides, Moessbauer experiments and the elastic property of metals after proton irradiation were continuously performed since the last year. A new technique was developed on a method of real-time analysis of deuterium atoms introduced into solid material by deuteron ion implantation. An experiment was initiated towards the fabrication of microstructures by heavy-ion bombardment.

A systematic investigation was carried out on the transmission of atomic and molecular negative ions through the 12UD Pelletron tandem accelerator. The development of a microprobe system for hydrogen analysis initiated in the last year was continued. In addition to resonant nuclear reaction analysis, we developed an elastic recoil coincidence analysis using proton-proton scatterings at around 20 MeV. The high penetrability of protons with high-energy and low stopping power has opened the analysis of hydrogen which is confined in fluid inclusions in silicate samples over the thickness of 0.2 mm. We tested a method of the suppression of nuclear gamma-ray background in NRA for thick silicate samples. In order to provide experimental data for the neutron dosimetry of Hiroshima atomic bomb, AMS measurements of ^{36}Cl were performed for samples that were taken at several places in Hiroshima city.

K. Furuno

Kohei Furuno

CONTENTS

1. ACCELERATOR AND EXPERIMENTAL FACILITIES

2. NUCLEAR PHYSICS

3. ATOMIC AND SOLID STATE PHYSICS, AND CLUSTER SCIENCE

4. ION BEAM APPLICATION

1.1 Accelerator operation 2001

K. Sasa, S. Ishii, H. Kimura, H. Oshima, Y. Tajima, T. Takahashi, Y. Yamato,
T. Komatsubara, K. Shima and K. Furuno

The operation of the 12UD Pelletron tandem accelerator was very stable for the period from April in 2001 to March in 2002. The total operating time and the experimental beam time were 2223.1 and 1729.0 hours, respectively. The operating time decreased by about 36 % as compared with that in 2000, because we did not operate the accelerator every Saturday and Sunday. Fig.1 shows the distribution of operation hours every month. The beam time at various terminal voltages is shown in Fig.2. Fig.3 presents the summary of accelerated ions and fractions of their beam time for three ion sources. Fig.4 shows the percentage of experimental beam times for research fields.

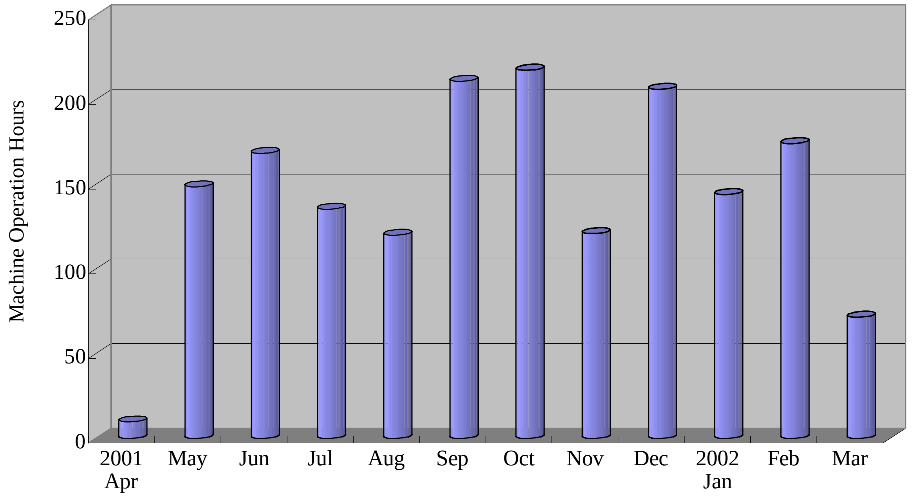

Fig.1 Accelerator operation hours per month from April in 2001 to March in 2002.

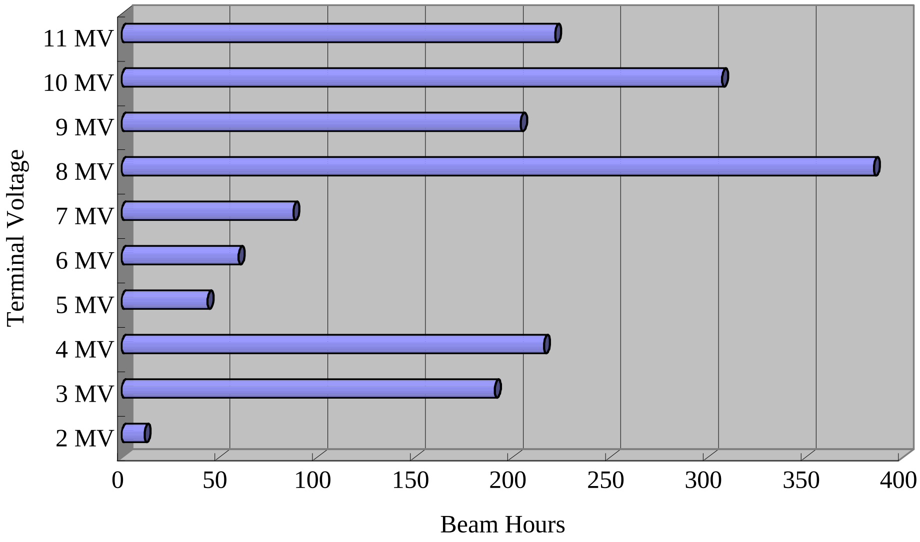

Fig.2 Beam time summed up every 1 MV of terminal voltages.

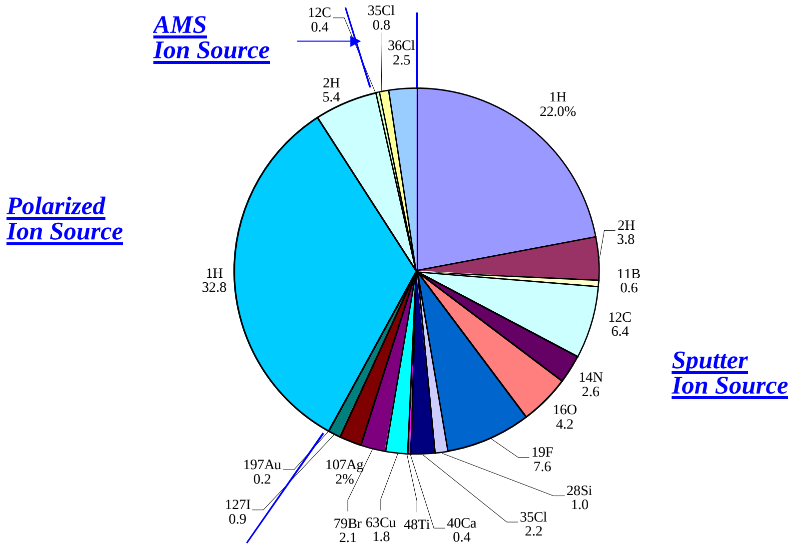

Fig.3 Accelerated ions and fractions of their beam time for three ion sources.

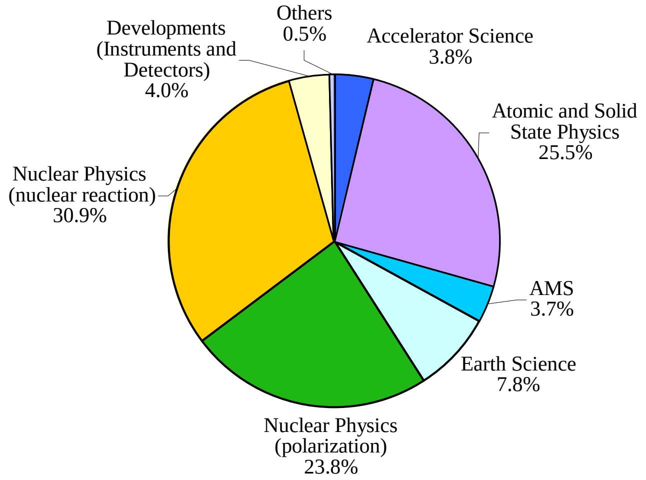

Fig.4 Percentage of experimental beam times for research fields.

The scheduled maintenance was finished on April 6 in 2001. After voltage conditioning and beam transport tests, we provided beams for experiments from May 9. In the year of 2001, some modifications of beam lines were carried out. In the first target room, the crystal ball and the heavy-ion post accelerator on the 0° beam line were shut down. A new microprobe system for hydrogen analysis of mineral samples was set up instead of these equipments [1]. A small general-purpose scattering chamber and a polarized deuteron target were constructed on the D-beam line (1-D). The latter was developed by the research group of Nagoya University as a joint project. A new experimental chamber for the measurement of the total reaction cross section was set on the B-beam line (2-B) in the second target room. The study of proton irradiation effect on metal at low-temperature was reopened on the D-beam line (2-D). Fig.5 shows the present beam courses.

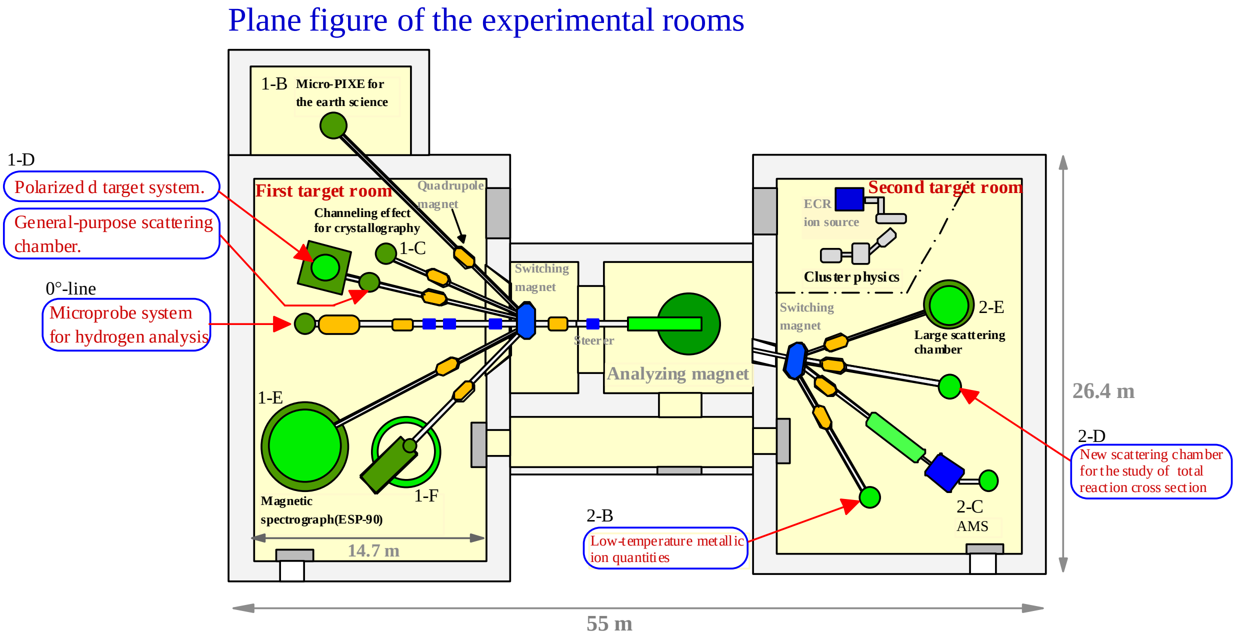

Fig.5 The present outline of each beam course.

In the year of 2000, we lost SF_6 gas by 656 kg in the operation of the gas handling system. This was a serious problem for us, so that we repaired the seal of the connecting rod of the SF_6 gas compressor. It was the main part of the gas leak found on May in 2000 and on January in 2002. After this repair, the gas leakage was decreased. The total gas leakage was however still 277 kg in the year of 2001.


(a) (b)

Fig.6 (a) The bearing points of the corona needle shaft under repairing.
(b) The leaking test of the repaired corona needle shaft using high-pressure N_2 gas.

The scheduled maintenance in the spring of 2002 was started from March 7 and finished on April 4. The major works of this maintenance were as follows. All corona points were replaced along the column and the accelerating tube. Stripper foils in A and B foil changers were also replaced by new foils. We repaired or replaced the oiling system, the shorting rod contacts, the insulating tire of the chain pulley. We found several leak points of SF_6 gas on the main accelerator tank. The leak at viewing port flanges and at the feedthrough of the corona needle shaft were large. We replaced the flanges and repaired the feedthrough. Fig.6 shows the leak test of the repaired corona needle shaft using high-pressure N_2 gas. We added 1000 kg SF_6 gas to the main accelerator tank at this time.

The total operating time of the 1 MV Tandetron accelerator was 350 hours for the period of 2001. The duoplasmatron ion source for He^- production was frequently shut down since 1999 [2]. It was caused by thinning down and breaking of the lead wire connected to the solenoid coil in the duoplasmatron ion source. We modified the lead wire using thicker wire and operated carefully. Since the purity of present cooling water is not so high, we are preparing to replace it by electrolysis-free organic coolant (ethylene-glycol).

References

[1] K. Sasa et al., Hydrogen analysis of mineral samples at University of Tsukuba, Nuclear Instruments and Methods B 190 (2002) 287-290.
[2] K. Sasa et al., UTTAC68 (1999) 1.

1.2 Calibration of the beam analyzing magnet with the adjustment of the image slit

K. Sasa, T. Komatsubara, S. Ishii, Y. Yamato, H. Oshima, T. Takahashi, H. Kimura, Y. Tajima,
K. Shima and K. Furuno.

A serious problem in our beam transport system has been the movement of focus produced by the quadrupole doublet in front of the switching magnet. This movement was due to the misalignment of beam emerging from the image slit of the analyzing magnet to the axis of the quadrupole doublet. It was serious to carry out microbeam experiments and precise measurements of nuclear reactions. We performed beam transport tests for the first and second target room. The walk of the focused beam was minimized by the displacement of opening in the image slit of the analyzing magnet. We displaced the center of the opening in the image slit by 1 mm upward for the first target room, and by 1.5 mm for the second target room. The opening position was adjusted by observing movements of the focus on a ZnS plate. The displacements of openings necessitated a new energy calibration of the analyzing magnet.

The energy calibration was performed by measuring excitation functions of the elastic and inelastic scattering of $^{12}C(p, p)^{12}C$ and $^{12}C(p, p')^{12}C$ in the vicinity of the resonance at 14.233 MeV [1]. The natural width of this is 0.86 ±0.12 keV [2]. Yields of scattered protons were measured by a silicon surface-barrier detector which was set at a laboratory angle of 160° in a scattering chamber. The scattered proton energies were 10.28 MeV for the grand state and 6.35 MeV for the 1st excited state. The targets used were self supporting carbon foils. For the first experimental room, the thickness was 15 $\mu g/cm^2$. The proton energy loss at 14.233 MeV was estimated to be 0.48 keV. For the second experimental room, a 6 $\mu g/cm^2$ thick carbon foil was prepared. The proton energy loss was estimated to be 0.18 keV. The openings in the image and object slit of the analyzing magnet were decreased to 0.5 ±0.05mm. The design values of the radius of curvature and the dispersion are ρ=1280 mm and D=3.8, respectively. The resolving power of the beam analyzing magnet is 9.4×10^3. The energy resolution is calculated to be 1.5 keV.

The measured yield curves are shown in Fig.1. Table 1 shows the experimental results. The proton energy was varied by changing the field of the analyzing magnet in steps of 0.1 Gauss. The calculated magnetic field is 4276.14 Gauss for the resonance energy of 14.233 MeV. For the first experimental room, the width of the yield curve was estimated to be 1.7 keV. This value is in agreement with a calculated width of 1.8 keV including the natural width, the energy loss in the target and the energy resolution of the analyzing magnet. The experimental magnetic fields corresponding to the resonance energy of the first and second experimental room were estimated to be 4276.30 ±0.07 and 4276.70 ±0.07 Gauss, respectively. The estimated error comes from an uncertainty of ± 0.05 Gauss in reading the resonance point on the yield curve and an accuracy of ± 0.05 Gauss in the NMR Gauss meter. From above values, new radii of curvatures for the analyzing magnet have been estimated to be 127.99 and 127.98 mm for the first and second experimental room, respectively.

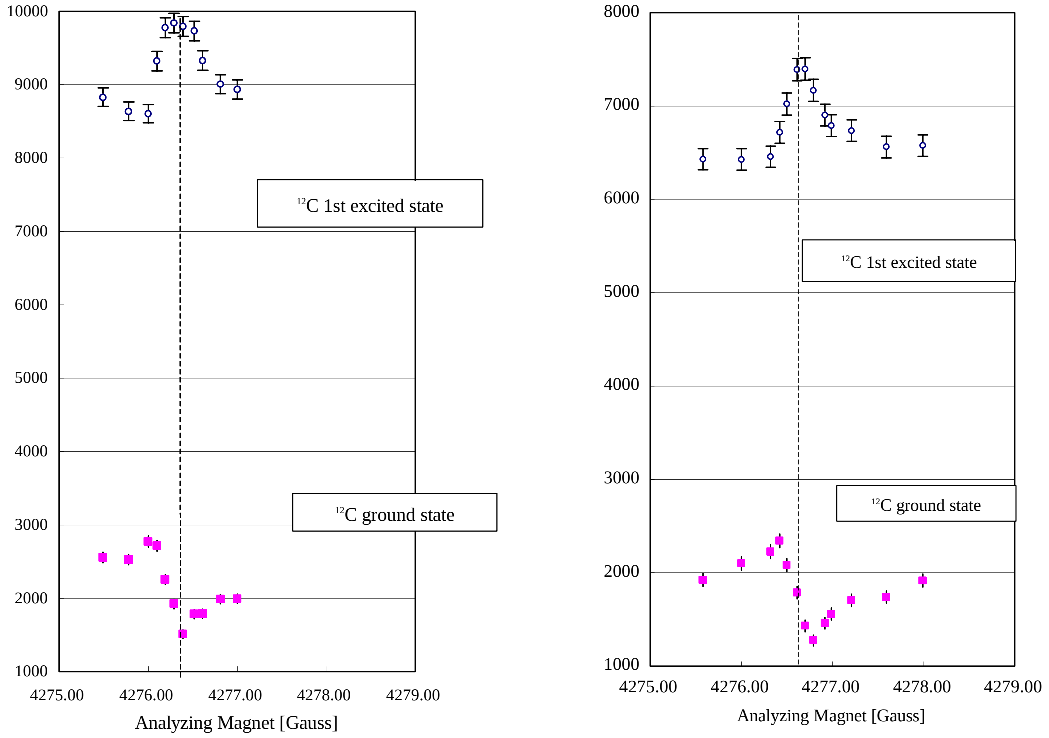

(a) (b)

Fig.1 Yields of scattered protons from the elastic scattering ^{12}C(p, p)^{12}C and the inelastic scattering ^{12}C(p, p')^{12}C. The data plotted in (a) is for the first experimental room. The data for the second experimental room is shown in (b).

Table 1 Experimental results of energy calibrations since 1977.

	Magnetic field [Gauss]	Radius of curvature [cm]
Calculated value	4276.14	128.00
1977 [3]	4275.10 ±0.07	128.03
1983 [4]	4278.1	127.92
2001 (this work)		
First experimental room	4276.30 ±0.07	127.99
Second experimental room	4276.70 ±0.07	127.98

References

[1] E. Huenges, H. Rosler and H. Vonach, Phys. Lett. B46 (1973) 361.

[2] Table of Isotopes 8th Edition, Vol.1 (1996) 13.

[3] K. Furuno et al., Calibration of the Beam Analyzing Magnet, UTTAC-2 (1977) 16.

[4] Y. Aoki, T. Komatsubara ; private communication.

1.3 Transmission of ions in 12UD Pelletron tandem accelerator for the injection of negative single atomic ions and of negative molecular ions

K.Shima, T.Takahashi, S.Ishii, and K.Sasa

For the last several years, the transmission data of ions in 12UD Pelletron tandem accelerator have been accumulated for the injection of negative single atomic ions as well as of negative molecular ions over the wide range of ion species, ion energies and stripper foil thickness. As the result, some systematic trends of transmission have been revealed.

1. Definition

By referring to Fig.1 showing the beam transportation system of 12UD Pelletron tandem accelerator, two transmissions *Tr(tank)* and *Tr(FC5)* are defined.

[a] *Tr(tank)*: the ratio of the number of atoms transmitting a tank to the number of atoms before injection into tank, which is expressed by $Tr(tank) = I_{FC3}/q_b/I_{FC2}$. Here, I_{FC3} and I_{FC2} are respectively ion beam currents at Faraday cup 3 and Faraday cup 2, and q_b means the mean charge of ions colliding with stripper installed at the terminal.

[b] *Tr(FC5)*: the ratio of number of atoms summed over all charge states, q, observed at the Faraday cup 5(FC5) placed at the downstream of analyzing magnet to the number of atoms before injection into tank. *Tr(FC5)* is given as $\Sigma_q\{I_{FC5}(q)/q\}/\, I_{FC2}$, where $I_{FC5}(q)$ is the beam current of ions with charge state q at FC5.

Two quantities *Tr(tank)* and *Tr(FC5)* are each other related by,

$$Tr(FC5) = Tr(tank)\, f(FC3/FC5), \qquad (1)$$

where *f(FC3/FC5)* indicates the transportation efficiency of ions from FC3 to FC5.

2. Transmission

[a] *Terminal voltage V_T and carbon stripper thickness dependence*

As was described in detail in ref. [1], *Tr(tank)* values are higher for increasing V_T values and for decreasing thickness of carbon stripper down to 2 μg/cm^2 except for the acceleration of light ions such as H, He ions. As an example, Tr(tank) values of ^{19}F ions are shown in Fig.2 for V_T = 10 MV and 3.5MV.

[b] *Tr(tank) and Tr(FC5)*

Generally, the 12UD tandem accelerator is operated by keeping the object slit width to be 2mm×2mm, and the imaging slit width to be 2mm. After passing through these two slits, ion beams are collected at the FC5, and *Tr(FC5)* values are measured. Fig.3 shows the observed values of *Tr(tank)* and *Tr(FC5)* versus atomic number of projectiles, Z, when V_T=10MV . Generally, $Tr(tank) \backsim Tr(FC5)$ for light ions such as H and Li, whereas the ratio *Tr(FC5)/ Tr(tank)* decreases with heavier or lower velocity ions and with thicker stripper foils. This is the result of beam broadening due to the multiple scattering and energy straggling occurred at the collision with charge stripper.

[c] *Single atomic ion injection and molecular ion injection into tank*

In the acceleration of ions by using a tandem accelerator, some atoms have to be injected into a tank in the form of negative molecular ions because of the electron affinity is small or zero. In Table 1, observed values of Tr(tank) or Tr(FC5) for ^{16}O and ^{28}Si ions are listed for the injection of O^- and Si^- ions at V_T=5MV, and O_2^- and Si_2^- ions at V_T=10MV. It is intended to compare the transmission of O^- and O_2^- (and of Si^- and Si_2^-) under the condition that they collide with a charge stripper at the same velocity. Table shows that the Tr(tank) or Tr(FC5) values of atoms for the injection of molecular ions are smaller than those for the injection of atomic ions. This is because the coulomb explosion of molecular ions during the collision with charge stripping atoms causes an additional disturbance of projectile momentum both in forward and perpendicular directions of beams, and hence the transmission of ions decreases. In fact, if we observe the Si ion beam profile at an imaging slit (see Fig.1) by changing the slit width in the above mentioned collisions, the intensity distribution of Si ions originated from Si_2^- is seen to be broader than that originated from Si^-, which is drawn in Fig.4.

Transmission data for the incidence of negative molecular ions have been accumulated over the wide range of ion species. As the result, an empirical formulae for Tr(FC5) has been evaluated by using the similar procedure described previously [2].

Table 1. Transmission of ions for the injection of $^{16}O^-$ and $^{16}O_2^-$, and $^{28}Si^-$ and $^{28}Si_2^-$.

^{16}O ions				^{28}Si ions			
Injected ion	Terminal V_T(MV)	Tr(tank)	Tr(FC5)	Injected ion	Terminal V_T(MV)	Tr(tank)	Tr(FC5)
$^{16}O^-$	5	78 %	28 %	$^{28}Si^-$	5	68 %	18 %
$^{16}O_2^-$	10	50 %	16 %	$^{28}Si_2^-$	10	41 %	9 %

3. Beam currents on target

The beam currents, $I_q(E)$, of ions having charge q and energy E at the target position, can be written as,

$$I_q(E) = I_{FC2}\, qF(q)\, Tr(FC5)\, f(transportation), \qquad (2)$$

where I_{FC2} is the beam current at FC2 placed at the upstream of the tank, $F(q)$ means the charge fraction of ions at the terminal colliding with the charge stripper, and $f(transportation)$ means the transportation efficiency of ions between FC5 and the target position. As mentioned above, *Tr(FC5)* is empirically known and the data of I_{FC2} have been accumulated over the wide range of Z for single atomic ions as well as molecular ions. F(q) is also well established values when the charge states are equilibrium. Hence, by using these quantities, it is possible to estimate the beam current at the target position within a factor 2 for the incidence of single atomic ions and a factor 3 for the incidence of molecular ions, once Z, mass number, q and E of accelerated ions are given.

References

[1] K.Shima, S.Ishii, T.Takahashi and I.Sugai, Nucl. Instrum. Methods A460 (2001)233.

[2] T.Takahashi, K.Shima, T.Ishihara and M.Yamanouchi, UTTAC Annual Rep. 1987, p.8.

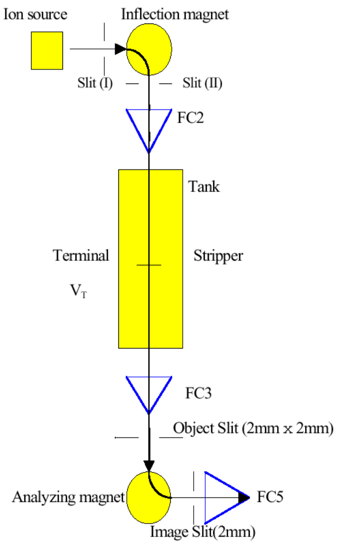

Fig.1. Transportation system of ions in 12UD Pelletron tandem accelerator.

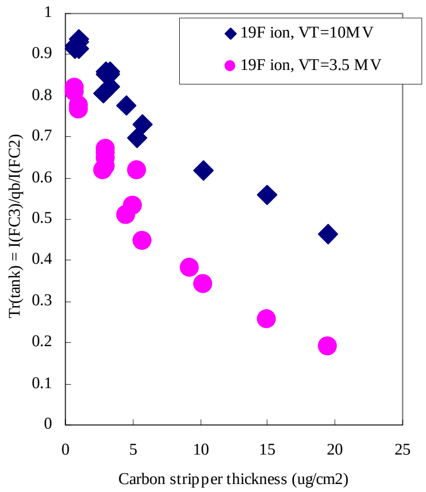

Fig.2. Transmission, Tr(tank), of ^{19}F ions versus stripper foil thickness at the terminal voltage V_T=10 MV and 3.5 MV.

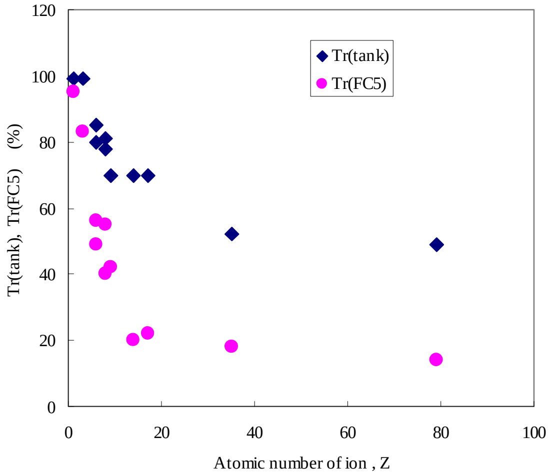

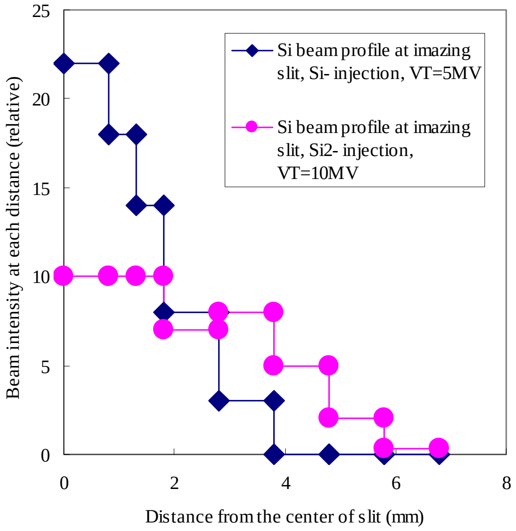

Fig.3. Transmissions Tr(tank) and Tr(FC5) plotted as a function of Z (atomic number of accelerated ions). The terminal voltage V_T=10 MV for all ions.

Fig.4. Beam intensity distribution of Si ions observed at the imaging slit for the incidence of Si^- and Si_2^- colliding with a charge stripping foil at the same velocity (V_T=5 MV for Si^- and V_T=10 MV for Si_2^-).

1.4 Microprobe system for hydrogen analysis of mineral samples

K. Sasa, Y. Yamato, H. Oshima, T. Komatsubara and K. Furuno.

[1] Construction of the microbeam line.

The construction of the microprobe system has been continued during the last year. The design was described in the annual report 2000 [1]. Fig.1 shows the present layout of the beam line. The total length of this system is 14.25 m between the first slit and the target. The working distance from the exit of the focusing lens to the target is chosen to be 0.33 m. In microbeam experiments, the opening of the image slit is decreased to 1.0 mm. The beam is collimated with the double slit consisting of the first and second slit. The diameters of the first and second slit are 0.4 mm and 2.0 mm, respectively. The third slit is placed in front of the Russian quadruplet. The diameter of the third slit is 9.0 mm. The chamber slit is placed on the exit of the Russian quadruplet. The diameter of the chamber slit is 4.2 mm. Fig.2 shows a photograph of the main part of the microbeam line.

The geometrical axis of the four quadrupole magnets in the Russian quadruplet is adjusted to be coaxial each other within 50 μm. The output of the power supplies for the Russian quadruplet is controlled by a 16bit DAC module to obtain the resolution of output currents as small as 0.5 mA.

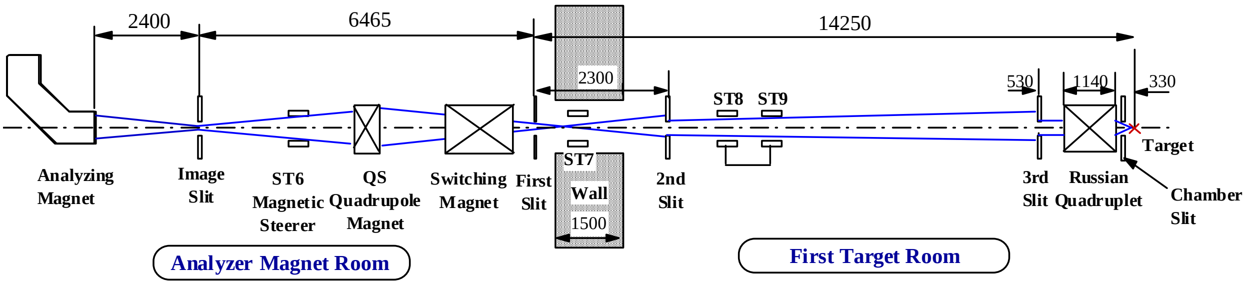

Fig.1 Present layout of the microbeam system.

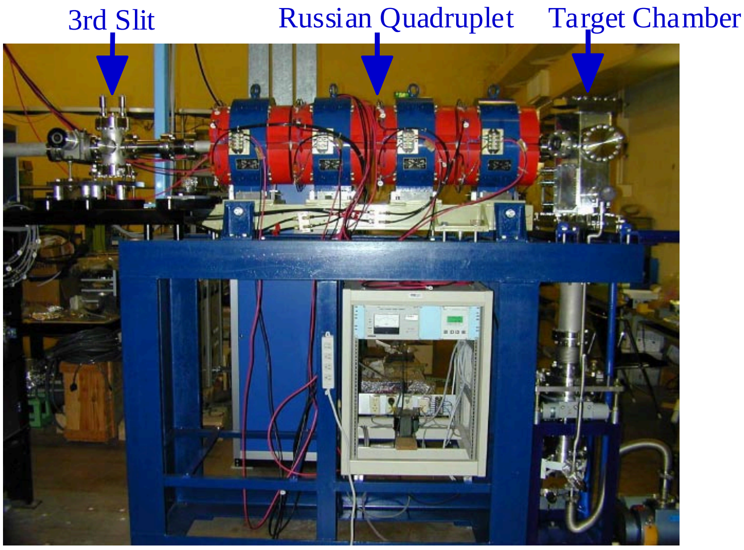

Fig.2 A photograph of the main part of the microbeam line.

Fig.3 The computer screen of the control console.

[2] Control system.

Power supplies for quadrupole magnets and steering magnets are controlled by means of a personal computer. To make execution most efficient, the control program is developed with Visual C++ operated on Windows 2000. Fig.3 shows the computer screen of the control console. When we change optical parameters, we select an optical element on the computer screen using a mouse click. The output of the power supply can be adjusted manually by turning the mouse wheel. Suitable transport parameters can be recorded in the computer. The recorded transport parameters can be read out and reset the suitable values within about 30 seconds automatically. Beams can be well focused by the parameters reproduced with this automatic setting. We can observe pictures from a CCD camera on the computer screen also.

[3] Microbeam formation.

The beam is finally focused on the target by means of the Russian quadruplet [2]. Beam optical calculations were carried out with the computer program TRACE-3D [3]. A demagnification of 16.7 can be expected for this microprobe system. The diameter of the focused beam spot is expected to be 24 µm. In the year of 2001, several tentative experiments were performed to estimate the size of microbeam spots. We focussed an 18 MeV proton beam on an Al coated quartz plate as thick as 2 mm. The projected range of 18 MeV proton is 1.85 mm in the quartz, so that all protons were stopped in the quartz. The focused beam spot was observed with a microscope set just behind the quartz target. The microscope had a CCD camera with 660×480 channels. Fig.4 shows a focused beam spot area. The beam spot is measured to be 72 µm in diameter. The beam current is 0.5 nA.

Table 1 shows a comparison of calculated exciting currents of the Russian quadruplet with experimental currents. The outer and the inner quadrupole magnets of the Russian quadruplet have the same exciting currents for each combination. The relative errors between the calculated and experimental exciting current of RQ 1 – 4 and RQ 2 – 3 are 3.6 % and 2.7 %, respectively.

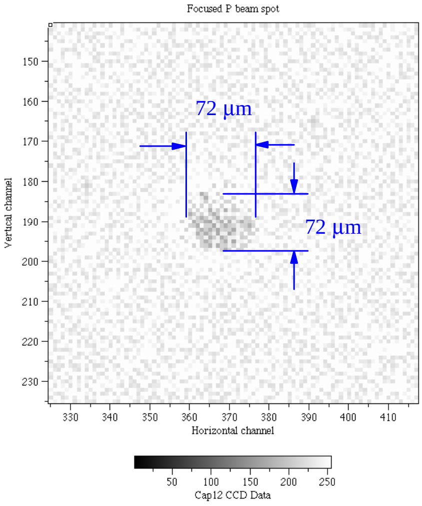

Fig.4　　A focused beam spot for the 18 MeV proton beam. The beam current is 0.5 nA.

Table 1　A comparison between the calculated and the experimental exciting current for the 18 MeV proton beam.

	Calculated magnetic field [kG /cm]	Calculated exciting current [A]	Experimental exciting current [A]
RQ 1 - 4	0.4425	3.404	3.526
RQ 2 - 3	-1.0609	8.161	8.385

[4] Beam transmission

A test of the beam transmission was performed for proton and $^{19}F^{5+}$ beams. There are five slits from the image slit of the beam analyzing magnet to the target camber slit on the microbeam line (Fig.5). The aperture of the first slit is 0.4 mm in diameter. FC5 is set just after the image slit of the beam analyzing magnet. FC6 is placed between the first and the second slit. FC7 is placed behind the second slit. The experimental results are summarized in Table 2.

The beam transmission from FC5 to the target is about 2 %. The beam current of this microprobe system would be sufficient to perform hydrogen analysis of mineral samples.

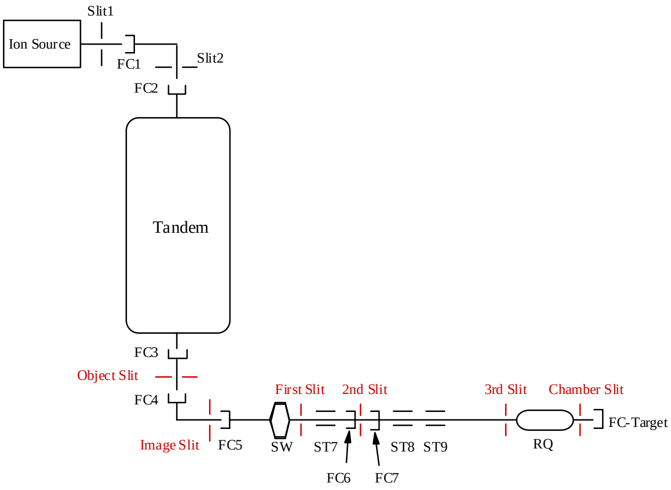

Fig.5　　A schematic setting of the Faraday cups (FC) for the measurement of beam current.

Table 2 Experimental results of the beam transmission for proton and $^{19}\mathrm{F}^{5+}$ beams.

Beam current [nA]	FC2	FC5	FC6	FC7	FC-target
$^{15}\mathrm{F}^{5+}$ [30 MeV]	150	90	5.8	0.5	-
P [20 MeV]	300	120	5.0	2.0	-
P [18 MeV]	132	25	0.62	0.54	0.48

Acknowledgement

This work is supported in part by the Grand-in-Aid for Scientific Research (A) of the Ministry of Education, Science, Sports and Culture.

References

[1] K. Sasa et al., UTTAC-69 (2000) 5.

[2] A. D. Dymnikov, T. Ya. Fishkova and S. Ya Yavor, Sov. Phys. Tech. Phys. 10 (1965) 340.

[3] K. Crandall and D. Rusthoi, “TRACE-3D Documentation”, third edition, Los Alamos National Laboratory Report LA-UR-97-886(1997).

1.5 Solution for the pulse height defect of MSTPC

H. Ishiyama[1], T. Kawamura[2], T. Hashimoto[2,3], T. Ishikawa[2], T. Furukawa[4], M. H. Tanaka[1], N. Yoshikawa[1], H. Miyatake[1], S. C. Jeong[1], T. Nomura[1], T. Komatsubara and Y. Tagishi

Rate dependencies of the pulse height from the KEK gas chamber called “ Multi-Sampling and Tracking Proportional Counter (MSTPC) [1] have been measured with the ^{14}N-beam (E = 30 MeV) from the Tandem accelerator. Possible solutions for the pulse height shifts observed in the MSTPC are discussed.

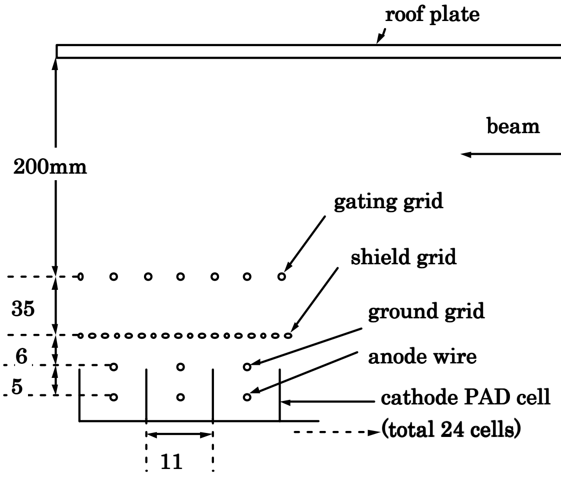

Fig. 1 Schematic Cross-sectional view of the MSTPC.

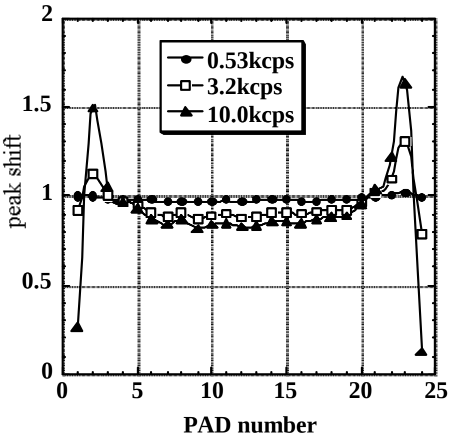

Fig. 2 Peak shifts of the MSTPC.

Fig. 1 shows the cross-sectional view of the MSTPC. The MSTPC can measure a three-dimensional track of a charged particle and the energy loss along its trajectory. Electrons produced by the incoming charged particle in the drift space are drifted through the three type grids toward the proportional region, which consists of 24 cathode PAD cells with anode wires. The gas inside the MSTPC (90% He and 10% CO_2) works both as a counter gas and a gas target. Using the MSTPC, an experimental program to determine astrophysical reaction rates for (α, n) with light neutron-rich radioactive nuclear beams is in progress.

The large peak shift of the energy loss signals from each PAD was observed under high injection rates (< 10^4 pps) of low-energy heavy ions. Fig. 2 shows the systematic change of the peak shift for various injection rates of ^{15}N particles (E = 2 MeV/u). The horizontal axis shows the PAD number, which corresponds to the distance in unit of cm from the beam injection point. The pulse height is normalized by one obtained under the injection rate about 200 pps. The sudden change of pulse heights around both edges of the MSTPC was found to be a charge-up on the G10 frames of the girds. In order to avoid this

---

[1] High Energy Accelerator Research Organization, Oho1-1, Tsukuba-shi, 305-0801 Japan.
[2] Tokyo University of Science, Yamazaki 2641, Noda-shi, Chiba-ken, 278-8510 Japan.
[3] Research Fellow of the Japan Society for the Promotion of Science.
[4] Osaka University, 1-1 Machikaneyama, Toyonaka-city, Osaka, 560-0043, Japan.

charge-up effect, we covered these frames by metal plates.

The pulse height defect around the center of the MSTPC is supposed to come from the space charge gain limitation near the anode wire. As a solution, we have therefore installed a gating grid [2] as shown in Fig. 1. Alternate wires of the gating grid are connected two separate voltage sources and the transparency of the gating grid plane is controlled by changing the potential difference of alternate wires. The gating grid plane is normally kept opaque so that electrons do not reach anode wires. When an external trigger, for example, generated by neutron counters in the case of our experiment, signals a nuclear reaction event, the gating grid makes transparent for the time so that the drift electrons reach anode wires. With these possible improvements, we tested effects of the gating grid experimentally using a sample beam ^{14}N.

The ^{14}N-beam (E = 30 MeV) was provided by Pelletron 12UD. The ^{14}N particles elastically scattered from a thin Au-target were transported to the MSTPC by a QDQ spectrometer. The gating grid was triggered by signals from a SSD at the end of the MSTPC. The trigger rate was reduced by a down scalar.

Fig. 3 shows peak shifts of the output signals versus counting rates without the gating grid. The vertical axis shows the pulse height normalized by one when the injection rate is a few pps. The horizontal axis shows the PAD number. The sudden change of the peak shift is clearly disappeared and the shift is so smooth in contract to fig. 2. When the injection rate is 3.6 kpps, the pulse height defect becomes about 15% around the center of MSTPC. This value is nearly the same to the case of ^{15}N-beam.

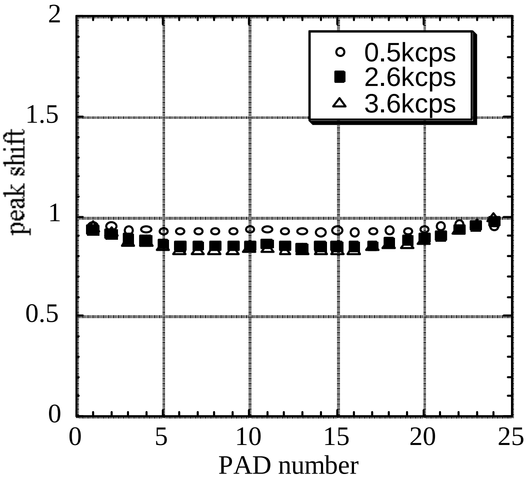

Fig.3. Peak shifts without the gating grid.

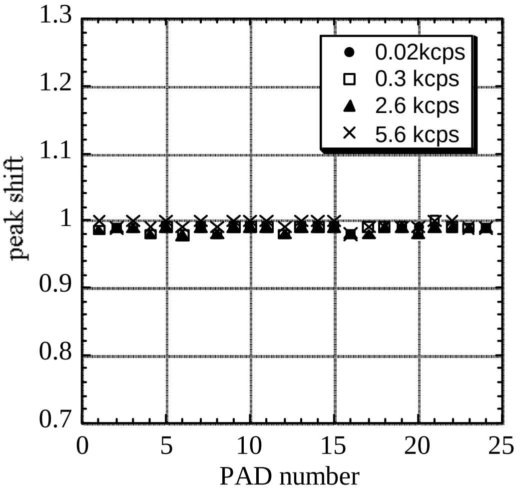

Fig. 4. Peak shifts using the gating grid

Fig.4 shows peak shifts using the gating grid. The trigger rate of the gating grid was fixed to be 20 cps for various injection rates. This value is a realistic one when our measurements of (α, n) reaction cross sections is performed. The peak shifts are suppressed within 2% up to the 5.6 kpps injection rate. This value is small enough to detect nuclear reactions of our interest.

As mentioned above, an origin of the pulse height defect around the center of the MSTPC is supposed to be the space charge gain limitation at the anode wire due to numerous ions generated by the proportional multiplication process. The growth in the avalanche process of a positive ion sheath around the anode wire causes the local reduction of the electric field to reduce the proportional multiplication. Following the formulation of the space charge limitation by Hendricks[3], we can evaluate the pulse height shift. The estimated value of the pulse height defect becomes 9% when the injection rate is 3.6 kcps. This value is consistent with the measured value. But the rather small reduction of the pulse height defect around both edges of the MSTPC can not be explained by the space charge gain limitation. A further investigation is therefore needed.

References

[1] Y. Mizoi, et. al., Nucl. Instrum. A 431(1999)112.
[2] P. Nemethy, et. al., Nucl. Instrum. Meth. A 212(1983)73.
[3] R. W. Hendricks, Rev. Sci. Instrum. 40(1969)1216.

1.6 Effect of minimum strength of mirror magnetic field on production of highly charged ions from RIKEN liquid He free super conducting Electron Cyclotron Resonance Ion Source (RAMSES)

H. Arai, M. Imanaka, T. Nakagawa[1], I. Arai and S.M. Lee

We have newly constructed two superconducting electron cyclotron resonance ion sources (ECRISs), which are 18GHz ECRIS (RAMSES) at RIKEN [1] and 14GHz ECRIS (SHIVA) at our laboratory [1-3]. From these sources, intense beams of highly charged heavy ions were successfully extracted. Typical results are 5eμA of Kr^{27+} and 2eμA of Kr^{29+} from RAMSES[1] and 10eμA of Xe^{30+} and 1eμA of Xe^{36+} from SHIVA[1-3].

Recently, it was reported that the optimum value for minimum strength of mirror magnetic field (B_{min}) exists to maximize the beam intensity of Xe^{20+} produced from ECRIS at Laboratorio Nazionale Sud, Catania (SERSE) [4]. However, the effect of B_{min} on the beam intensity of various charge states is still unclear. To clarify this effect and to optimize the magnetic configuration to maximize the beam intensity of various charge state heavy ions extracted from ECRIS, we need further investigation. Especially, it is important to measure the beam intensity of various heavy ions systematically as a function of magnetic field. From this point of view, we measured the beam intensity of various heavy ions as a function of B_{min}.

We used RAMSES at RIKEN for this experiments. Fig. 1 shows a cross-sectional view of RAMSES. For studying effect of B_{min} on the beam intensity, we changed B_{min} from 0.25T to 0.6 T without changing the maximum magnetic field strengths on both the beam extraction side and the microwave injection side (B_{ext} and B_{inj}), respectivety as shown in Fig.2. In this experiment, B_{ext} and B_{inj} were fixed at 1.13 and 1.7 T, respectively. The injected microwave power was 500 W. The extraction voltage was 12 kV. The gas pressure, position and negative voltage of biased electrode were changed to maximize the beam intensity. We did not use the gas mixing method for simplicity the experiment.

To determine the optimum B_{min} for various ions, we measured beam intensities of $O^{5,6+}$ and $Ar^{7\sim 11+}$ ions as function of B_{min}. Fig. 3 shows the beam intensity of Ar^{7+} and Ar^{11+} as a function of B_{min}. In case of both Ar^{7+} and Ar^{11+}, the beam intensity gradually increased with increasing B_{min} up to 0.45T and then gradually decreased. Furthermore, we measured that the optimum B_{min} for maximizing the beam intensity in case of the other ions were almost the same as the value 0.45T in case of Ar^{7+} and Ar^{11+}.

References

[1] T. Nakagawa et. al., Rev. Sci. Instrum., 73 (2002) 513.
[2] T. Kurita et. al., Nucl. Instrum. Methds B (to be published).
[3] T. Kurita et. al., UTTAC Annual Report 2000, Tandem Accelerator Center, University of Tsukuba.
[4] D. Hitz, et. al., Rev. Sci. Instrum. 73 (2002) 509.

---

[1] The Institute of Physical and Chemical Research (RIKEN)

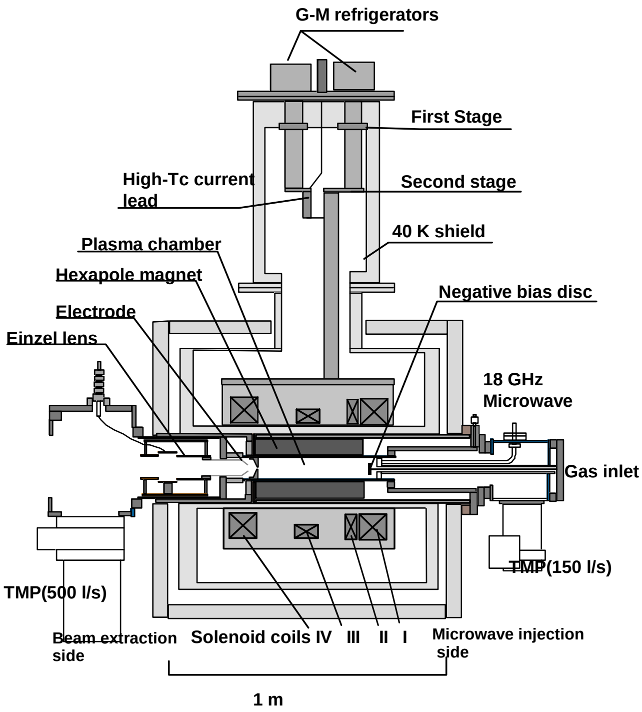

Fig.1 Cross sectional view of RAMSES

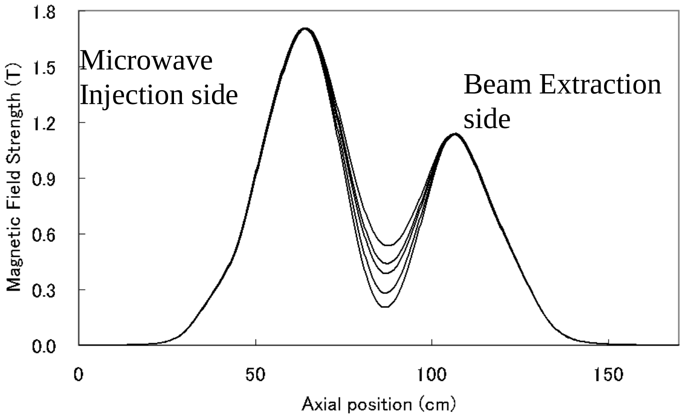

Fig.2 Magnetic configuration of RAMSES

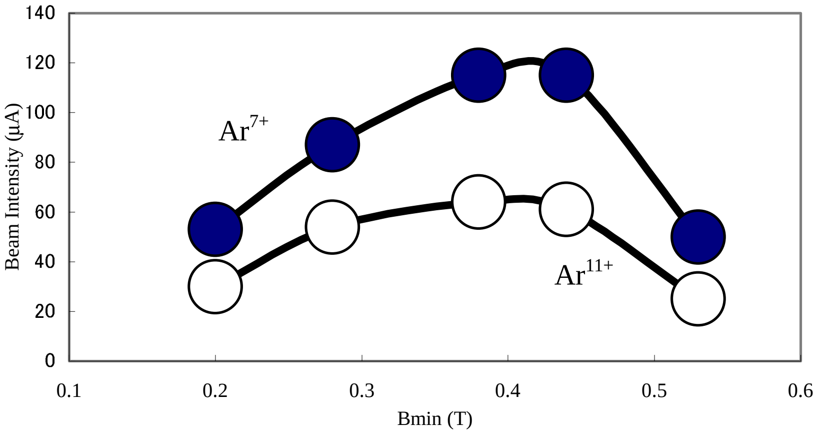

Fig.3 Measured beam intensities of Ar^{7+} and Ar^{11+} as a function of B_{min}; B_{ext} and B_{inj} were fixed at1.13 and 1.7 T, respectively.

1.7 Radiation safety at tandem accelerator center

T. Komatsubara, K. Shima, K. Sasa, T. Katabuchi, Y. Yamato, S. Ishii, T. Takahashi, H. Kimura, H. Oshima, Y. Tajima, and K. Furuno

In the new Japanese regulation in accordance with ICRP90 recommendation, the annual effective dose limit has been decreased. For the safety of radiation control at the Tandem Accelerator Center, a new evaluation of effective dose by gamma and neutron radiations has been done.

Neutron dose rates were measured by a BF_3 neutron dose survey meter ALNOR 2202D. The tube of the BF_3 proportional counter is surrounded by a shield made of polyethylene and boron plastics in order to degrade fast neutrons. The survey meter indicates effective dose and also provides pulse signals for counting integration measurements. The survey meter is calibrated by using ^{241}Am+Be neutron source of 357MBq in which intensity of emitting neutron is $2.7{\times}10^4$ [n/sec]. Corresponding neutron dose is calculated to be 0.32 [μSv/h] at 1[m] from the source by using the effective dose coefficient $\Gamma = 1.19 \times 10^{-5}$[$\mu$Sv/h·m^2/(n/sec)]$^{1)}$. The results of the calibration are shown in Table 1 depending on the direction for the survey meter.

Gamma rays were measured by an ionization chamber survey meter Aloka IC-311. The results of the calibration are shown in Table 2 by using ^{137}Cs source of 371.4 kBq. The effective dose coefficient of $\Gamma = 0.0779$ [μSv/h/MBq·m^2] $^{1)}$ is used.

As the results of the measurements which were briefly reported in reference 2, Table 3 shows measured dose rates for the 1MV tandetron and Table 4 for the 12UD pelletron. For the 1MV tandetron, proton beam was accelerated up to 1.6 MeV by 0.8 MV terminal voltage. Beam current was 0.1 μA irradiated on a thick tantalum beam stopper. No radiation exceeding back ground has been measured at any position in the tandetron experimental room. For the 12UD pelletron accelerator, the radiation measurement has been done by using proton beam accelerated up to 22 MeV by 11 MV terminal voltage. The ion beam was irradiated on a beam stopper of thick tantalum plate located in the counting room shown in figure 1. Neutron effective dose were measured with beam of 0.45 and 0.7 μA, in the target room and outside of shielding wall, respectively. Small flux of neutrons through the concrete shielding wall have been measured as shown in Table 4. By normalizing beam intensity and distance from the irradiation point, the effective dose penetration rate can be determined to be 3.1×10^{-6} for the 1.2 m thick normal concrete of 2.3 g/cm^3 density.

In the new evaluation of radiation dose, effective dose by neutrons and gammas has been calculated. For operation of the 12UD tandem accelerator we assume that thick tantalum targets at the 2nd target room and in the vacuum chamber of analyzing magnet are irradiated by 3 μA and 1.5 μA, respectively. Reaction cross sections are calculated as a function of incident beam energy by using CASCADE program. Effective thickness of the tantalum stopper is estimated by considering stopping power$^{3)}$. Since neutron energy spectrum is similar to those for ^{241}Am+Be neutron source, penetration factors$^{1)}$ for neutron of the ^{241}Am+Be neutron source are used to evaluate effective dose. Since the calculated dose is over estimated for 1.2m concrete shield, we introduce correction factor $G_n = 0.023$ from a comparison between the calculation and the neutron measurements. For the 1MV tandetron, we assume that the accelerator is under operation of 1MV with 3μA beam. The only X-rays from stray electrons are important. Furthermore, several radioactive source are assumed to be stored in a storage room. As the results of the calculation, estimated effective dose are shown in Table 5. Working hours and accelerator operation are estimated to be 40h/week and 144h/week. The 3 months correspond to 13 weeks. The effective dose are lower than the limitation of the new Japanese regulation for all calculated points.

In Table 6, 7 and 8, effective dose measurement by area monitoring system are shown for this fiscal year. The measured results on border of control area are small enough which should be lower than the regulated limit of 1300μSv/3months.

Since an effective dose can be proportional to a beam intensity and operation hours, products of beam intensities and beam hours are evaluated for the 12UD tandem accelerator as shown in Table 9. Under our regulation the beam intensity is limited to be 3μA and operation hours should be less than 144hours/week. When we multiply the regulated value a limit of the product is introduced to be 1728 [μA·h] for a month. For every month, the product is much smaller than the limitation.

Reference

1) Practical manual of shielding calculations for radioisotope facility, 2000, Nuclear Safety Technology Center, Hakusan 5-1-3-101, Bunkyo-ku, Tokyo, Japan
2) T. Komatsubara, K. Shima, K. Sasa, T. Katabuchi, Y. Yamato, S. Ishii, T. Takahashi, H. Kimura, H. Oshima, Y. Tajima, K. Furuno, PROGRESS REPORT, INDC(JPN)-189/U, JAERI, Tokai, (2002), p89-91, "private communication"
3) Program SRIM (2000) J.F. Ziegler, IBM-Research

ALNOR 2202D distance [mm]	^{241}Am+Be calculation [μSv/h]	θ=0 [μSv/h]	θ=90 [μSv/h]	θ=0 pulse [cpm]	θ=90 pulse [cpm]
200	8.0	10	6	203	130
250	5.1	5	3	125	88
300	3.6	3	2	83	68
coefficient		1.0	1.6	0.69 $\times 10^{-3}$ [μSv/pulse]	0.95 $\times 10^{-3}$ [μSv/pulse]

Table 1 Result of calibrations for BF_3 neutron dose survey meter, ALNOR 2202D. θ indicates angle of source position with respect to symmetry axis of the survey meter.

Aloka IC-311 distance [mm]	^{137}Cs calculation [μSv/h]	measure [μSv/h]
100	2.9	3.7
150	1.3	1.7
200	0.7	1.2
Back ground		0.2
coefficient		0.81

Table 2 Result of calibrations for gamma survey meter of ionization chamber, Aloka IC-311

location	distance [m]	beam current [μA]	gamma IC-311 [μSv/h]	neutron ALNOR 2202D [μSv/h]	neutron pulse
scattering chamber	0.3	0.1	0	0	0/4min
switching magnet	3.3	0.1	0	0	0/4min
control desk	8.0	0.1	0	0	0/4min
entrance	5.2	0.1	0	0	0/4min

Table 3 Gamma and Neutron dose rates during the ion beam experiment of the 1 MV tandetron

location	distance [m]	beam current [μA]	gamma IC-311 [μSv/h]	neutron ALNOR 2202D [μSv/h]	neutron pulse [cpm]
Target room	8.0	0.45	200	9600	
Outside of wall	8.6	0.7	0	0.04	30/30min

Table 4 Gamma and Neutron dose rates during the ion beam experiment of the 12 UD tandem accelerator

location	effective dose
The 2nd experimental room	0.09 [μSv/week]
Tandetron experimental room	0.02 [μSv/week]
Entrance of storage room	0.54 [μSv/week]
Northern border of control area	73 [μSv/3months]
Entrance of the 1st experimental room	22 [μSv/3months]
Entrance of tandetrom experimental room	3.6 [μSv/3months]
Western border of university of Tsukuba	5.8 [μSv/3months]

Table 5 Sum of calculated effective dose by accelerator operations of the 12UD tandem and the 1M tandetron and the storage of several RI sources.

	A1	A2	A3	A4	A5	A6
April	0	0	0	0	0	0
May	0	0	0	0	0	0
June	27	22	0	0	0	0
July	26	0	0	0	0	0
August	1000	296	0	0	0	0
September	36	7260	0	0	0	0
October	2	62	0	0	0	0
November	0	284	0	0	0	0
December	0	3490	0	0	0	0
January	0	191	0	0	0	0
February	97	483	0	0	0	0
March	7475	0	0	0	0	0

Table 6 Gamma-ray and X-ray radiation exposures measured inside of the building. The values are shown in units of μSv/month.

	N1	N2	N3	N4	N5	N6
April	2	10	0	0	0	0
May	3	41	0	0	0	2
June	331	884	0	0	0	2
July	440	0	0	0	0	0
August	16330	5068	0	0	0	0
September	298	227	0	0	0	0
October	109	2843	0	0	0	4
November	79	93	0	0	0	2
December	34	40100	0	0	0	0
January	29	4115	0	0	0	0
February	840	16950	0	0	0	0
March	81290	0	0	0	0	42

Table 7 Neutron radiation exposures measured inside of the building in units of μSv/month.

	NP1	NP2	NP3
April	0	0	0
May	0	0	0
June	0	0	0
July	0	0	0
August	5	0	0
September	0	0	0
October	0	0	0
November	0	0	0
December	0	0	0
January	0	0	0
February	0	0	0
March	0	0	0

Table 8 Neutron radiation exposures measured outside of the building on the border line of control area. The values are shown in units of μSv/month.

	Beam current × Operation hours [μ A $\cdot$h]
April	0
May	5.6
June	8.6
July	3.3
August	11.3
September	6.5
October	2.8
November	2.7
December	33.0
January	3.2
February	7.3
March	33.2

Table 9 Beam current multiplied by operation hours [μA$\cdot$h] for the accelerator operation of 12UD tandem accelerator.

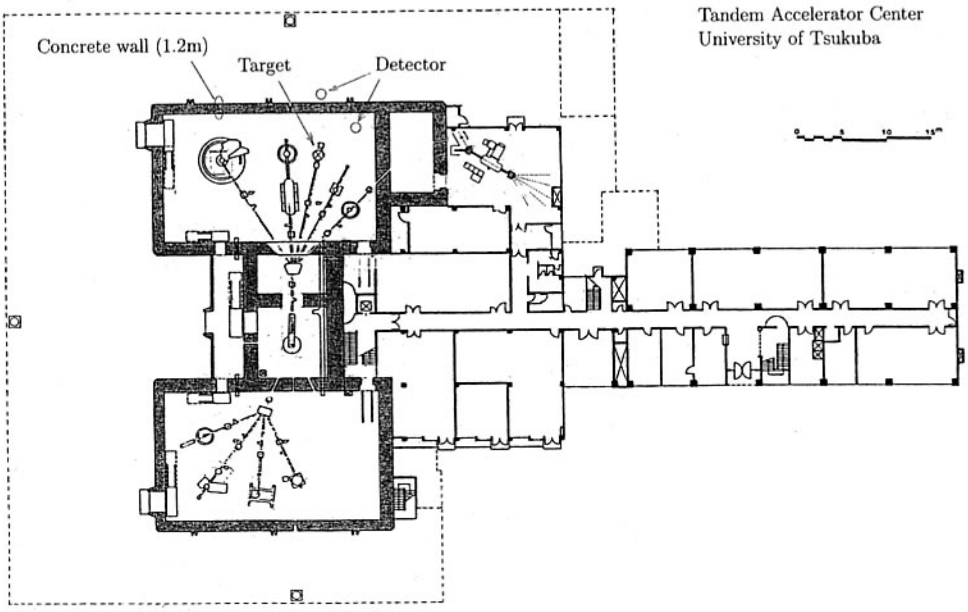

Figure 1. Location of a radiation target and detection positions for the 12UD pelletron experiment.

2.1 Elastic and inelastic scattering protons on $^{nat}\mathrm{Si}$ at $^{28}\mathrm{Si(p,n)}$ threshold energy region

N.Okumura, T.Joh and Y.aoki

Last year, we reported that the energy dependence of proton total reaction cross sections on ^{28}Si had resonance like behavior around the $^{28}\mathrm{Si(p,n)}$ threshold energy (15.7 MeV) [1]. The depth and width of the dip are about 60 mb and 300 keV, respectively. The width corresponds to 2×10^{-21} sec. The presence of this marked energy dependence may reveal a reaction mechanism of the proton elastic scattering, incident proton may temporarily be captured by a target nucleus, for instance. Partial wave analysis of the elastic phase shift should be correlated to what orbital angular momentum is really related with this phenomenon. Energy dependence of the phase shift should be related the time delay of the outgoing wave packet. Austern showed the time delay $Q_{\alpha\beta}$ of the reaction (α, β) is related with the energy derivative of the phase shift as,

$$Q_{\alpha\beta} = 2\hbar \frac{\partial \delta}{\partial E_\alpha}, \tag{1}$$

[3]. Hirota measured elastic data of $^{28}\mathrm{Si(p,p)}$ reaction and analyzed by using an optical model approach [2]. We believe that the coupled channels effect may be important.

Differential cross sections $(\sigma(\theta))$ and analyzing powers $(\mathrm{Ay}(\theta))$ of $^{28}\mathrm{Si(p,p)}$ and $\mathrm{(p,p')}$ reaction were measured by using polarized protons accelerated between 15.1 and 16.7 MeV. The silicon target was about 1.45 mg/cm^2 thick $\mathrm{SiO_2}$ plate. Protons elastically scattered off the target were detected by two pairs of 3 mm thick solid state Li drift detectors located on either side of the beam line. These detectors subtended solid angles of 0.3 to 1 msr. Proton polarization was monitored continuously by a polarimeter located 45 cm downstream of the target position. Analyzer reaction is $^4\mathrm{He}(\vec{\mathrm{p}},\mathrm{p})$ elastic scattering to 112°.

Fig. 1 summarized the $\sigma(\theta)/\sigma_R(\theta)$ and $\mathrm{Ay}(\theta)$ of elastic scattering at some incident proton energies. The inelastic scattering cross sections and analyzing powers leading to the $^{28}\mathrm{Si}(2^+)(E_x = 1.78\ \mathrm{MeV})$ and $^{28}\mathrm{Si}(4^+)(E_x = 4.6\ \mathrm{MeV})$ of 15.9 MeV protons are shown in fig. 2. The phase shift analysis using these data is in progress.

References

[1] N. Okumura, T. Joh, Y. Honkyu, K. S. Itoh and Y. Aoki, UTTAC annual report 21(2001).

[2] K. Hirota, K. Miura, K. Koyama, N. Okumura, K. Kishita, Y. Mukouhara, S. Nakagawa, M. Masaki, Y.Tagishi and Y.Aoki, UTTAC annual report 13(1995)

[3] Norman Austern, DIRECT NUCLEAR REACTION THEORIES, INTERSCIENCE MONOGRAPHS AND TEXTS IN PHYSICS AND ASTRONOMY, *Vol.* XXV, *chap.1*(1970).

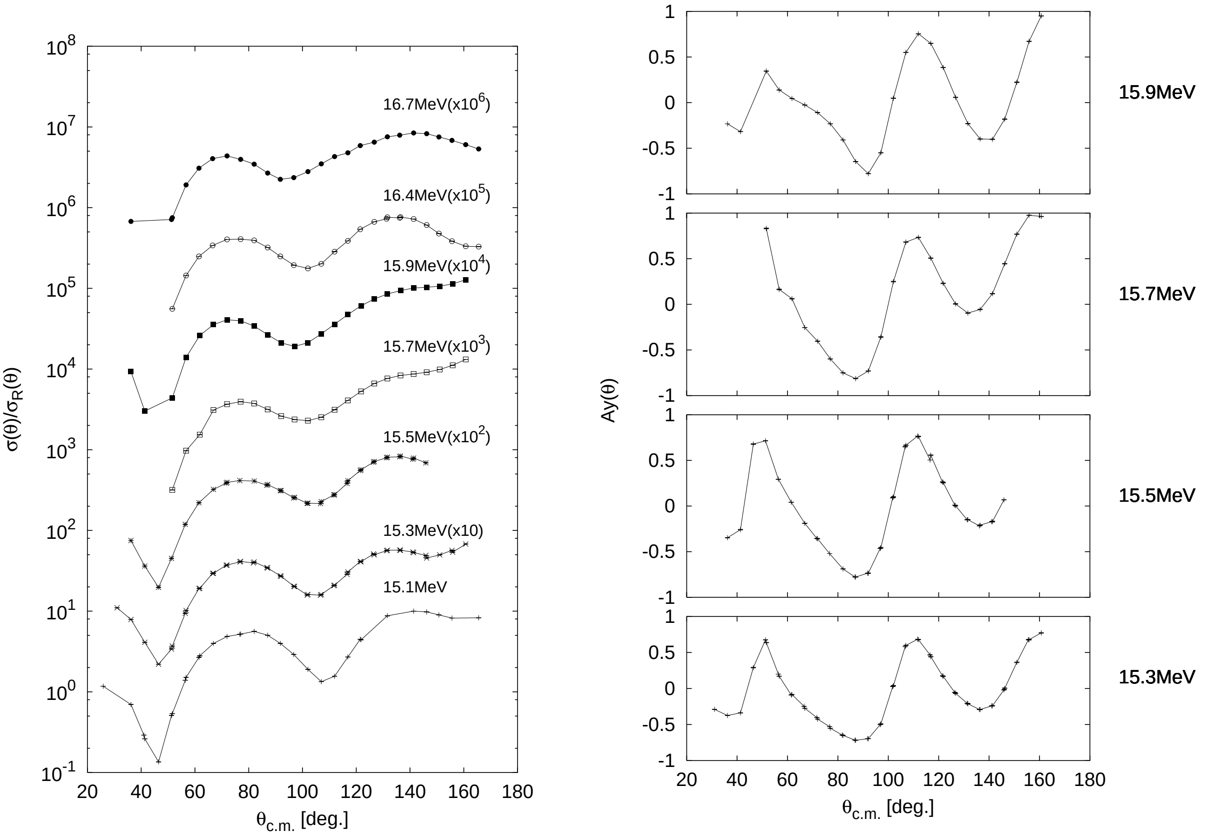

Fig. 1. Proton elastic cross sections and analyzing powers. The each line is shown for guide eyes.

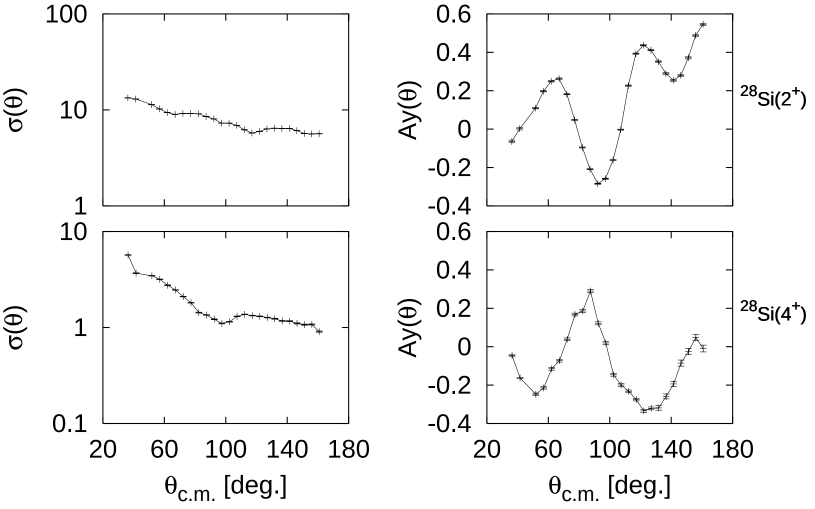

Fig. 2. Inelastic scattering cross sections and analyzing powers of 15.9MeV protons.

2.2 CDCC analysis of triple differential cross section of ^{208}Pb(d,pn) reaction at E$_d$=56 MeV

Y. Aoki, N. Okumura, T. Jho and Y. Iseri[a]

As an extension of an CDCC analysis, triple differential cross sections of deuteron elastic break up process is studied.

The concept of Continuum Discretized Coupled Channels (CDCC) approach of deuteron elastic scattering and breakup process is spelled out by Kawai and co-workers in ref. [1]. A brief description is given here just to remind the concepts of the ingredients. The CDCC Hamiltonian may be written as follows,

$$H = T_p + V_p + T_n + V_n + V_{pn},$$

where T_p and T_n are kinetic energy operator of a proton and a neutron, which are bound to form a deuteron in the incident channel. They interact with each other by the potential V_{p-n}. Continuum states are discretized by wave number binning. We assumed that the spin flip process may be negligible and the spin singlet states are neglected. Scattering states really taken into the analyses are, $^3S_1 - {}^3D_1$, $^3D_{2,3}$, $^3P_{0,1}$ and $^3P_2 - {}^3F_2$ states. Wave number k_{p-n} of the relative p-n motion are binned by 10 bins of $k_{p-n} = 0 - 0.1\ , \cdots\ 0.9 - 1.0 fm^{-1}$. Reid soft core potential [2] is assumed whenever it is available. Gaussian potential, which reproduce the phase shift, is assumed for the $^3D_3$ states.

Proton and a neutron interaction with a target nucleus are given by potentials of V_p and V_n. No explicit excitation of target nucleus and rearrangement reactions are taken into account. Nucleon optical potential, CH89 [3], of half the deuteron kinetic energy $E_p = E_n = E_d/2$ are assumed in the present analyses. Proton in the deuteron interact with the target nucleus via Coulomb potential, which are assumed to be due to uniformly charged sphere. Because deuteron is a bound state of proton and a neutron, antisymmetrization correction is necessary even if we assume that the phenomenological optical potential takes care of the exchange effect of incident nucleon and nucleons in the target. This antisymmetrizaton correction is phenomenologically taken into account by reducing(increasing) the real(imaginary) central part of the optical potential.

Proton and neutron coordinates $\mathbf{r}_p,\ \mathbf{r}_n$ are expressed by the center of mass and relative coordinates by the following relation,

$$\mathbf{R} = (\mathbf{r}_n + \mathbf{r}_p)/2, \quad \mathbf{r} = (\mathbf{r}_n - \mathbf{r}_p)$$

Coupled channels equation for the R coordinates are written by partial wave expansion, solved numerically and S-matrices are obtained. In handling the nucleon spin-orbit potential, terms with $(\mathbf{s}_p - \mathbf{s}_n)$ are neglected.

A detailed data of elastic scattering by Matsuoka [4] and triple differential cross sections by Okamura [5] are taken into account and the case of 56 MeV deuteron + ^{208}Pb are considered.

Elastic differential cross section and other polarization observables are calculated from the elastic S-matrices. Differential cross section of experimental data and the present analysis are compared in fig. 1.

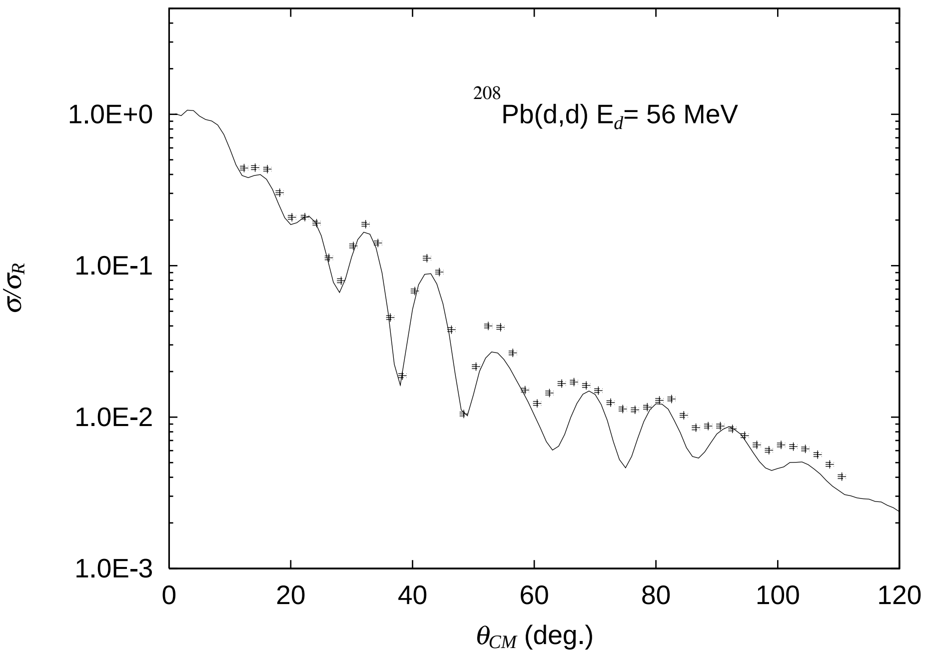

Fig. 1 Comparison of elastic of ^{208}Pb(d,d) at E_d=56 MeV

A reasonable reproduction can be seen. This is also true for the polarization observables. Phase relation, peaks and valleys of the angular distribution pattern, can be reproduced well by introducing the antisymmetrization correction.

Triple differential cross section $\dfrac{d^3\sigma}{d\Omega_n\, d\Omega_p\, dE_p}$ are calculated by the following relation,

$$\frac{d^3\sigma_{\nu_p\nu_n}}{d\Omega_n d\Omega_p dE_p} = \frac{2\pi}{\hbar v_{p+n-T}}|T_{fi}|^2 \rho_1(E_p) = \frac{2\pi}{\hbar}\frac{\mu_{p+n-T}}{P_{p+n-T}}|T_{fi}|^2 \rho_p(E_p). \tag{1}$$

Spin orientations of ν_p and ν_n are included in this expression. Proton state density $\rho_p(E_p)$ are given in the literature [6].

Expression of T-matrix (T_{fi}) is somewhat complicated because of the recoupling of p-n state wave functions and many angular momenta involved in the analysis and is not written here.

Triple differential cross sections measured by Okamura is a proton energy spectrum measured at $\theta_p = \theta_n = 0°$. At very forward angles, many partial waves interfere constructively and make a very sharp peak. Average over the proton and neutron detectors should be made to explain the experimental energy spectrum.

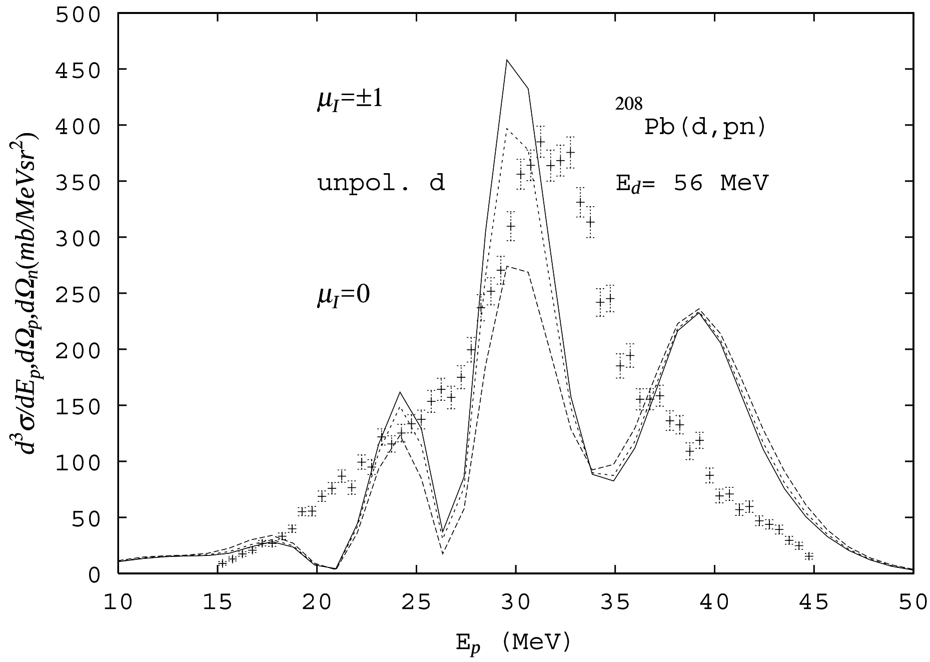

Fig. 2 Comparison of experimental and CDCC triple differential cross sections at $\theta_n = \theta_p = 0^\circ$

Fig. 2 compares the experimental data with the averaged triple differential cross sections for polarized and unpolarized deuterons. Polarization axis is along the beam direction.

One can see a large peak at $E_p = 30$ MeV, while experimental peak is located at about $E_p = $ 31-32 MeV. Large valleys can be seen on both sides of the peak, which are not seen in the experimental data. The origin of these valleys can be ascribed to the destructive interference of nuclear and Coulomb contributions for this reaction. This statement can be confirmed by limiting the maximum angular momentum and drawing an energy spectrum.

Importance of continuum coupling can also be confirmed as follows.

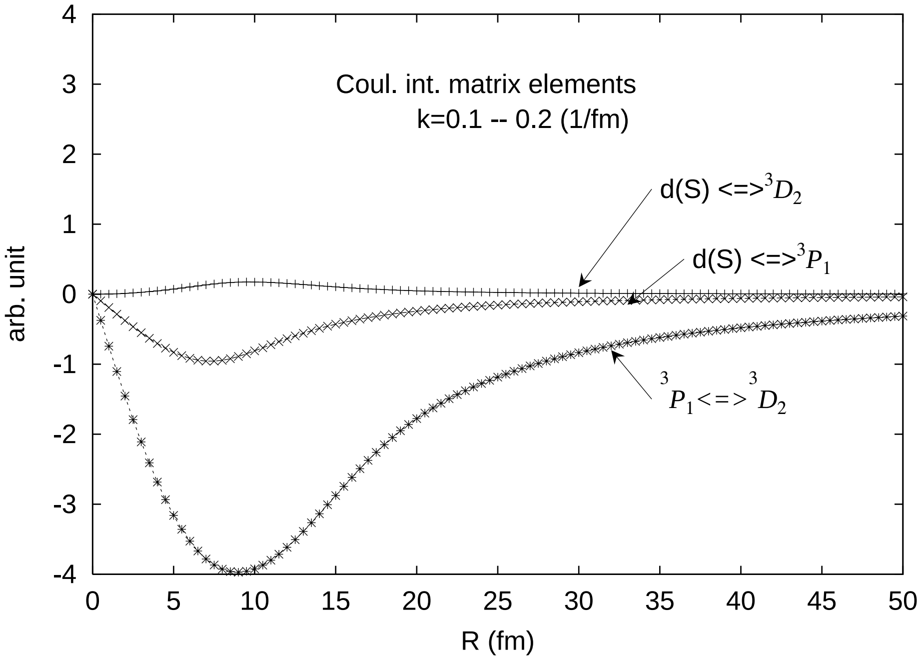

Fig. 3 Typical Coulomb matrix elements

Fig. 3 compares three matrix elements, which connect three states in p-n system,the S-state of the deuteron, ${}^3P_1$ and ${}^3D_2$. Wave number of these scattering states are $k_{p-n} = 0.1 - 0.2\,fm^{-1}$. Continuum-continuum coupling, in this case, is much larger than the direct break up matrix elements. We can study the elastic break-up cross section by plotting the following quantity,

$$\frac{10\pi}{3K^2_{p+n}}(2J+1)|S^J(break-upchannel)|^2$$

By using this quantity, we can compare quantitatively at what J and to what breakup channel, the incident flux is actually directed. Ratio of positive to negative parity break up can be studied by changing the amplitudes of these off diagonal matrix elements.

References

1 M. Kamimura, M. Yahiro, Y. Iseri, Y. Sakuragi, H. Kameyama and M. Kawai, Prog. Theor. Phys. **89** 1986

2 R.V. Reid, Jr., Ann. Phys.**50**(1968) 411

3 R.L. Varner, W.J. Thompson, T.L. McAbee, E.J. Ludwig and T.B. Clegg, Phys. Rep. **201**(1991) 59

4 N.Matsuoka, H.Sakai, T. Saito, K. Hosono, M. Kondo, H. Ito, K. Hatanaka, T. Ichihara, A. Okihana, K. Imai, K. Nishimura, Nucl. Phys. **A455** (1986) 413

5 H.Okamura, A.Ishida, N. Sakamoto, O.Otsu, T. Uesaka, T. Wakasa, H. Sakai, T. Niizeki, H. Toyokawa, Y. Tajima, H. Ohnuma, M. Yosoi, K. Hatanaka and T. Ichihara, Phys. Rev. **C58** (1998) 2180

6 G.G. Ohlsen, Nucl. Instr. Meth. **37**(1965) 240.

2.3 Analyzing powers for the $^{6}\mathrm{Li}(\vec{d},p)^{7}\mathrm{Li}$ reaction at an incident energy of 90keV

N.Yoshimaru, T.Iiduka and Y.Tagishi

In order to obtain the information of the reaction mechanism of $^{6}\mathrm{Li}(\vec{d},p)^{7}\mathrm{Li}$ reaction at low energy region, we measured analyzing powers of this reaction at incident deuteron energy of 90keV. The ^{6}Li target is the same as that used in the $^{6}\mathrm{Li}(\vec{d},\alpha)^{4}\mathrm{He}$ reaction described in this annual report. The emitted particles were detected by four silicon photodiodes (HAMAMATSU S3204). Four analyzing powers, iT_{11}, T_{20}, T_{21} and T_{22}, were measured for laboratory angles from 0- to 105-degree with 15-degree step. A typical energy spectrum is shown in Fig.1, where the number 1, 2, 3, and 4 are corresponding to the emitted particles from reactions $^{2}\mathrm{H}(\vec{d},p)^{3}\mathrm{H}$, $^{6}\mathrm{Li}(\vec{d},p_{1})^{7}\mathrm{Li}$, $^{6}\mathrm{Li}(\vec{d},p_{0})^{7}\mathrm{Li}$ and $^{6}\mathrm{Li}(\vec{d},\alpha)^{4}\mathrm{He}$, respectively. The measured analyzing powers are shown in Fig.2. An interesting thing is that the vector analyzing power has negative values of around –0.1, although those for $^{6}\mathrm{Li}(\vec{d},\alpha)^{4}\mathrm{He}$ are zero within the statistical errors as described in this annual report. A further analysis is now in progress.

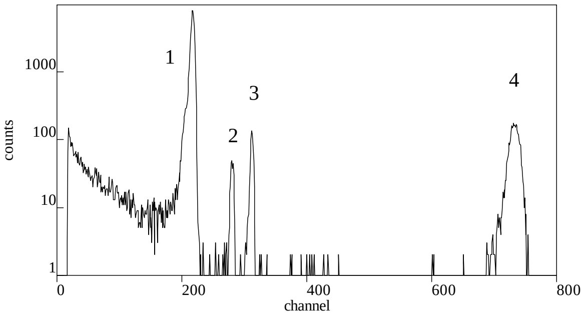

Fig.1 Energy spectrum of the emitted particles.

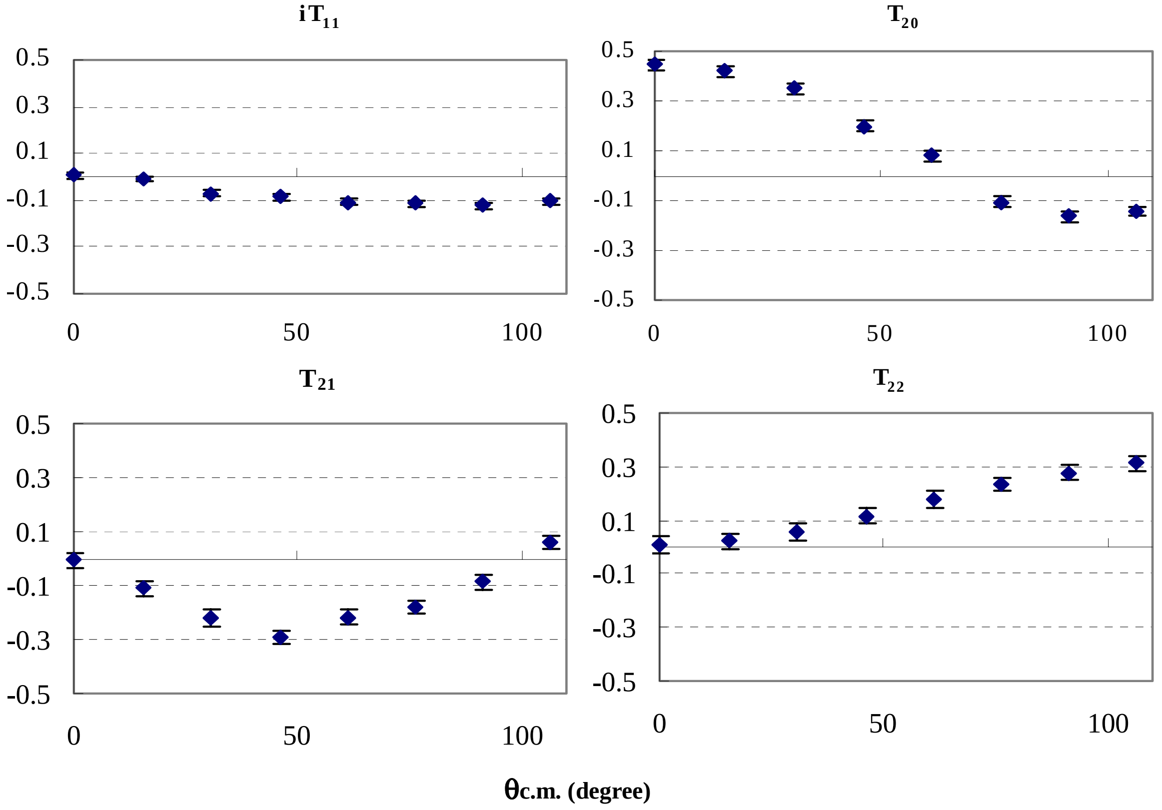

Fig.2 Analyzing powers iT_{11}, T_{20}, T_{21} and T_{22}.

2.4 Measurement of proton polarization in ^{208}Pb(d,p)^{209}Pb reaction at incident energy of 20 MeV

M.Yamaguchi, N.Kawachi, T.Iizuka, N.Yoshimaru, K.Shiga and Y.Tagishi

The polarization of emitted protons from the ^{208}Pb(d,p)^{209}Pb reaction to the $\frac{9}{2}^+$ ground-state was measured by a high efficiency proton-polarimeter[1]. The experiment was performed at the Tandem Accelerator Center, University of Tsukuba (UTTAC). The incident deuteron energy was 20.5 MeV. The target was a self supporting ^{208}Pb foil with a thickness of 40 mg/cm^2. The deuteron beam loses a part of its energy in the target and the deuteron energy takes about 20 MeV at the center of the target. Typical value of the beam intensity at the target was about 400 nA. The emitted protons from ^{208}Pb(d.p) reactions were momentum-analyzed by QDQ magnetic analyzer system[2] and focused on the polarimeter target. The horizontal and vertical angular spreads of emitted protons were $\pm 2°$ and $\pm 1°$, respectively. A spectrum of emitted protons is shown in Figure 1. The spectrum was obtained by changing the magnetic field of the Dipole magnet of the QDQ-magnet analyzing system. The peak corresponding to the transition to the ground state of ^{209}Pb was separated from the transition to the first exciting state.

Figure 2 shows a comparison of the present experimental data with a finite-range DWBA and continuum discretized coupled channel (CDCC(d,p)) calculations. These calculations predicted negative values at forward angles, however, the experimental values were zero within the statistical uncertainties. At present we could not predict the measured proton polarization.

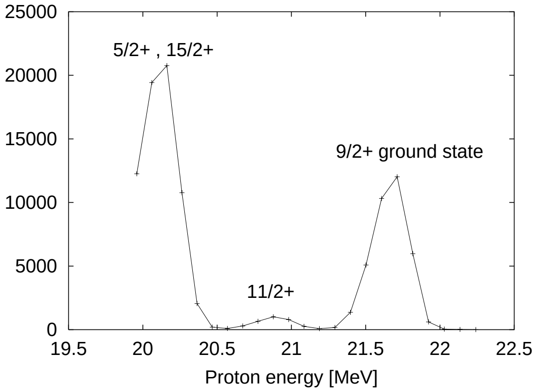

Fig. 1. Energy spectrum of the protons coming from the ^{208}Pb(d,p) reactions.

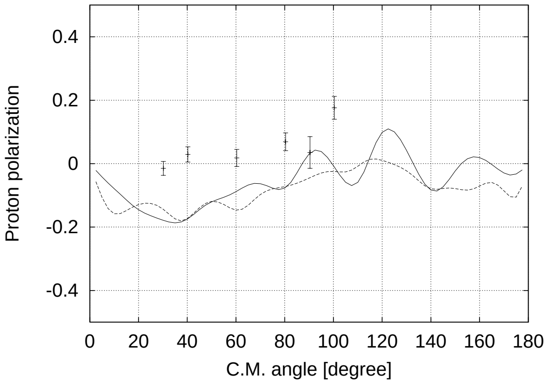

Fig. 2. Polarizations of the emitted protons from the ^{208}Pb(d,p)^{209}Pb reaction to $\frac{9}{2}^+$ ground-state. Solid line represents the result of DWBA calculations. Dashed line shows the CDCC(d,p) calculation.

References

[1] M. Yamaguchi, T.Katabuchi, N,Yamada, N.Kawachi, Y.Tsuchiya, K.Sawada, T.Takizawa, K.Takagi, K.Masuno and Y.Tagishi, UTTAC Annual Report 66, 7(1997)

[2] Y. Aoki, S. Hiroki, M. Tomizawa, Y. Tagishi and K. Yagi, UTTAC Annual Report 52, 5(1987)

2.5 The ^{6}Li(d,α)^{4}He reaction at an incident energy of 90 keV

T. Iizuka, M. Yamaguchi, N. Kawachi, N. Yoshimaru, K. Shiga and Y. Tagishi

The reaction ^{6}Li(d,α)^{4}He at energies below the Coulomb barrier has been studied to understand nucleosynthesis in the early universe [1]. The experimental data of the cross sections suggested that the ^{6}Li(d,α)^{4}He reaction might be dominated at low energies by a broad 2^+ subthreshold resonance in the compound nucleus ^{8}Be [2]. In the present works, we have measured the analyzing powers iT_{11}, T_{20}, T_{21} and T_{22} fro the ^{6}Li(d,α)^{4}He reaction at an incident energy of 90 keV for more understanding of the reaction mechanism for this reaction at energies below the Coulomb barrier.

The emitted alpha particles were detected simultaneously by eleven silicon photodiodes (HAMAMATSU S2744) placed in a scattering chamber at every 20°from +90°to +90°-90°and 0°in the laboratory system. Each anode of photodiodes placed at θ=+90°to +10°and –90°to –10°was connected in series with resistances and each cathode was also connected in series without resistance. As shown in Fig. 1, we could clearly distinguish signals from each counter by applying a position detecting method with charge division. The solid angle of each counter was 20 msr, which corresponded to a detector angular acceptance of $\Delta\theta$=3°. Experiments were performed with 90 keV polarized deuteron beam from a Lamb-shift type polarized ion source at UTTAC. The ^{6}Li target was prepared by vacuum evaporation of ^{6}Li$_2$CO$_3$ onto a 15 μm thick aluminum foil, whose thickness was about 10 μm/cm^2. The energy loss of the incident deuterons in the ^{6}Li$_2$CO$_3$ target was estimated about 8 keV.

Angular distributions of the four analyzing powers are shown in Fig. 2. All the measured vector analyzing powers are zero within the statistical errors. However, three tensor analyzing powers (T_{20}, T_{21} and T_{22}) present large angular distributions. The differential cross sections have almost constant values of about 20 μb/sr for all scattering angles. We compared present data with the calculations of the compound reaction model [3]. In this model, we considered formation of a single resonance state of 2^+ of ^{8}Be with s-wave incident deuterons. Results of calculations are shown in Fig. 2 as solid lines. All the measured tensor analyzing powers are well reproduced by these calculations.

References

[1] R. A. Malaney et al., Phys. Rep. 229, 145 (1993)
[2] K. Czerski et al., Phys. Rev. C55, 1517 (1997)
[3] F. Seiler, Nucl. Phys. A286, 1 (1977)

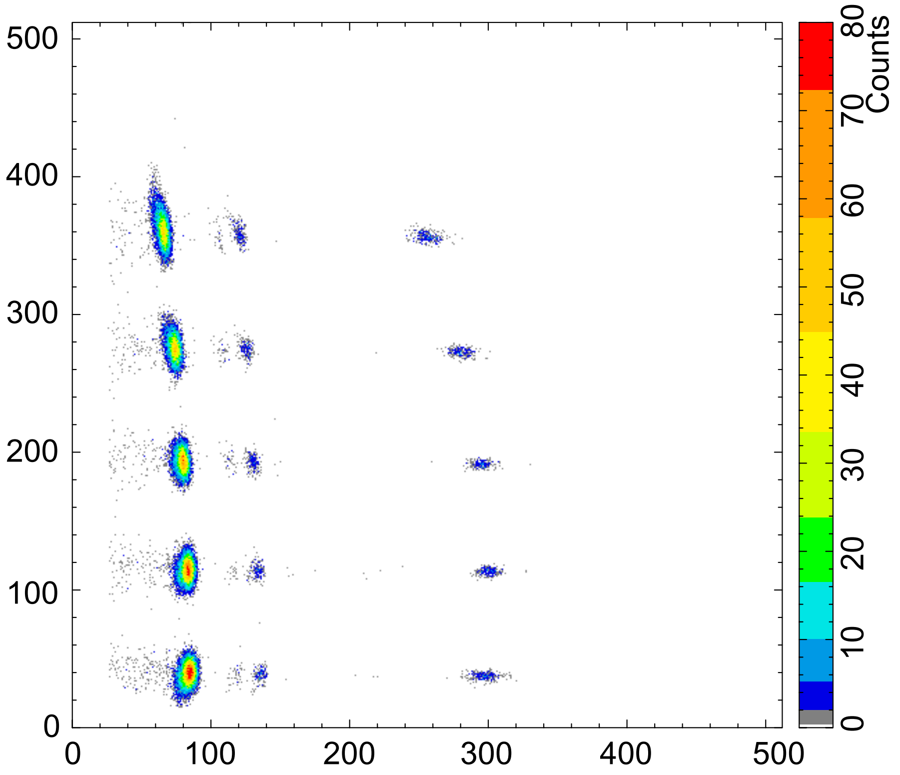

Fig.1. Two dimensional spectrum between energy and position. In the energy spectrum, alpha particles for each counter are correspond to around 300 channel.

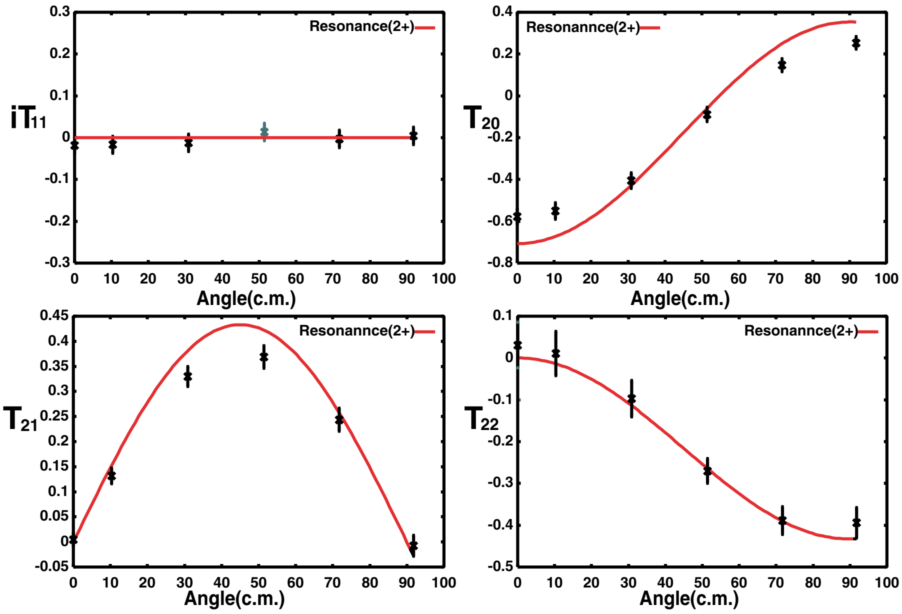

Fig.2. Comparison of analyzing power of the ^{6}Li(d,α)^{4}He reaction at an incident energy of 90 keV. The solid curves are results of the compound reaction model.

2.6 Spin precession measurement of polarized proton ions by transient magnetic field

T. Komatsubara, K. Sasa, T. Katabuchi, M. Yamaguchi, T. Iizuka, H. Oshima, Y.J. Ma, Y. Sasaki, S. Yokose, M. Ishizuka, Y. Tagishi, K. Furuno, T. Koyano [1]

Transient magnetic field (TMF) is known as hyperfine interaction between a magnetized foil and a fast traveling nucleus[1]. Since the first observation of the TMF by Borchers[2], nuclear magnetic moments for many nuclei in a wide range of mass region were measured by using the TMF of several thousand tesla.

The magnitude of TMF can be calculated from Fermi contact field B_0 multiplied by the charge fraction $q_{(1s)}$ of a hydrogen like atom and the spin polarization $p_{(1s)}$ of 1s electron, as the following formula.

$$B = B_0 \cdot p_{(1s)} \cdot q_{(1s)}.$$

The Fermi contact field B_0 can be calculated as $B_0 = 16.7Z^3$ [tesla] without relativistic correction. The strength of TMF depends on the ion velocity. When the ion velocity is the same order of magnitude as the 1s electron velocity $v = Zv_0$, where v_0 denotes Bohr velocity $v_0 = \frac{c}{137}$, TMF interaction is supposed to be most effective. In the lower velocity region, velocity dependence of TMF is well studied. However, a few measurements were reported for the higher velocity region. Brennan[3] reported very small amplitude of TMF for μ^+ ions whose velocity is 0.69c.

In order to detect TMF for the higher velocity region spin precession measurements were performed by using a polarized proton beam at the 12UD tandem accelerator center of University of Tsukuba. A magnetized iron foil of 50 μm in thickness was irradiated by 7MeV polarized protons. Because of stopping power in the iron foil for the traveling protons, the energy of ejected proton ions is degraded to be 5 MeV. For the measurements of the spin precession, two polarimeters were installed at upstream and downstream of the iron foil. Two 2mg/cm^2 carbon foils were used as scattering targets of the polarimeters located at 80 mm upstream and 60 mm downstream of the iron foil. Asymmetries of elastically scattered protons were measured by using left and right Si detectors at angles of $+50°$ and $-50°$, respectively. The analyzing powers depending on the the proton energy were measured to be -0.27 and -0.87 for the 7.0 and 5.0 MeV, respectively. Initial direction of the polarized proton was chosen to be parallel to the beam axis. When magnetic field is added in the foil along to horizontal plane, asymmetry of the scattered protons appears proportional to the spin precession.

Two kinds of experiments were done by using the magnetized iron foils. In the first experiment, an electro-magnet shown in Fig. 1 was used to change the polarity of the external magnetic field by the electric current. The number of turns of the coil 150. When the coil was excited by a current of 1.0 A, magnetic field in the thin iron foil was saturated. The saturation was detected by the rf electro-magnetic induction coils described in our previous report[6]. However, fringing magnetic field also appeared around the gap space. In order to reduce the fringing field, iron tubes were installed to cover beam axis shown in Fig. 1. The tubes work as magnetic field cramps to cut the fringing field to be 35 gauss on the iron foil.

In another experiment, thin iron foils were prepared as permanent magnetic strips shown in Fig. 2. The strips were magnetized by strong magnetic field. The magnetic field density B inside of the magnetized foils were deduced from integral of induction voltage measured by digital oscilloscope (DSO) as shown in Fig. 2. When we dropped the strip through a pick up coil of 80

---

[1] Cryogenics Center

turns induction voltage was appeared as shown in an envelope of Fig. 3(a). The time integral of the voltage shown in Fig. 3(b) corresponds to 1.2 tesla.

In Fig. 4, shift angles with the magnetized iron foils are indicated as "Fe−B" and "Fe+B" for the opposite directions of the magnetization. In order to evaluate fringing field, reference measurements were done by using a copper foil of the same thickness as the iron foil. Results for the copper foil are shown as "Cu−B" and "Cu+B". For the zero field measurement, a copper foil was used without external magnetic field. However, the result for the zero field shown as "Cu" in the Fig. 4 is not consistent to the other data with magnetic field. Unexpected stray field could affect the result. When an internal magnetic field of 1.2 tesla is subtracted, the measured value of the TMF can be deduced as 1.2 ± 3.2 tesla.

Fig. 5 shows the results for the permanently magnetized strips. Data points indicated as "Fe−B" and "Fe+B" show shift angles by the magnetized iron foils. Reference measurements with copper and iron foils are shown as "Cu" and "Fe". The "Cu" data agrees as zero magnetic field. However, the result "Fe" is not the center between "Fe−B" and "Fe+B". This result could be explain by unexpected small magnetization of the foil. When an internal magnetic field of 1.2 tesla is subtracted, the measured value of the TMF can be 0.9 ± 2.4 tesla.

Consequently, significant strength of TMF was not observed by both experiments. Both results can not be account for spin precession by TMF beyond error bars. Reason of the absence could be explained by high velocity of protons. When the ions travel through the iron foil where the average velocity is 15.4 v_0 in the unit of Bohr velocity, electric charge state of the proton is +1. This means that no electron exists to create TMF at position of nucleus. If we extend more significant region to detect the TMF, more heavier ion could be candidate as shown in Fig. 6 where ion energies corresponding to $v_0 \cdot Z$ velocity are compared with the maximum energies at UTTAC.

References

[1] N.B. Koller, M. Hass, J. Sak, Ann. Rev. Nucl. Part. Sci. 30 (1980) 53

[2] R.R. Borchers, J.D. Bronson, D.E. Murnick, L. Grodzins, Phys. Rev. Lett. 17 (1966) 1099

[3] J.M. Brennan, N Benczer-Koller, M. Hass, W.J. Kossler, J. Lindemuth, A.T. Fiory, D.E. Murnick, R.P. Minnich, W.F. Lankford, C.E. Stronach, Phys. Rev B18 (1978) 3430

[4] M.P. Robinson, A.E. Stuchbery, E. Bezakova, S.M. Mullins, H.H. Bolotin, Nucl. Phys. A647 (1999) 175

[5] S.J. Moss and W. Haeberli, Nucl. Phys. 72 (1965) 417

[6] T. Komatsubara, K. Sasa, T. Katabuchi, M. Yamaguchi, K. Kudo, K. Sawada, I. Masuno, T. Iizuka, H. Oshima, Y.J. Ma, Y. Sasaki, K. Yamada, S. Yokose, M. Ishizuka, M. Yoshimoto, Y. Tagishi, K. Furuno, T. Koyano, UTTAC annual report 2000, UTTAC-69, (2001), 43

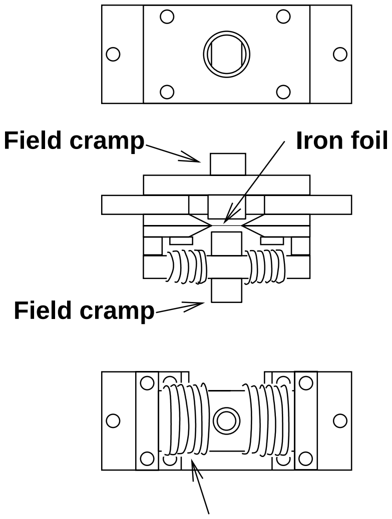

Fig. 1. A magnetic circuit with electric coils, return yoke and a thin iron foil. In order to reduce fringing magnetic field, field cramps made of iron pipes were located entrance and exit for the foil on the beam axis.

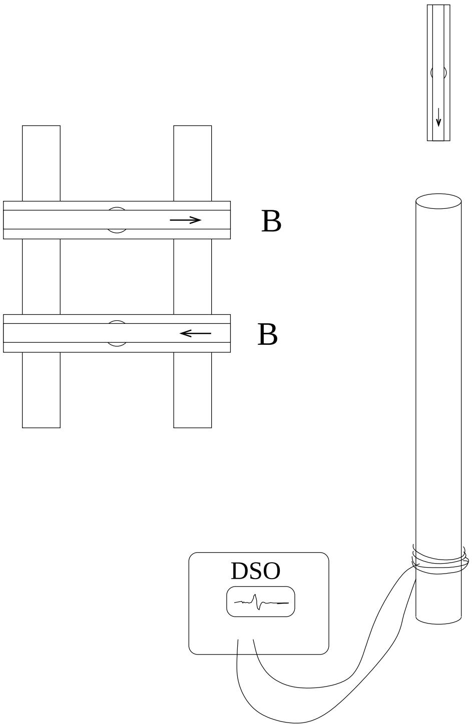

Fig. 2. Two strips of permanently magnetized iron foils. A detecting device for the magnetization consisting of a digital oscilloscope (DSO) and a pickup coil is also shown. When a strip of foil is dropped along to the guide pipe and passes through the pickup coil, inducted voltage can be recorded by the DSO.

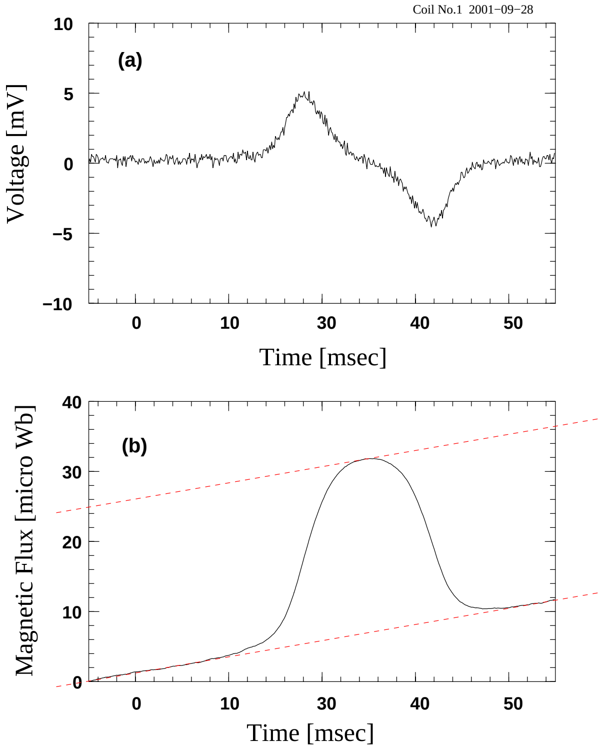

Fig. 3. (a) Inducted voltage and (b) its time integral recorded by the DSO shown in Fig. 2.

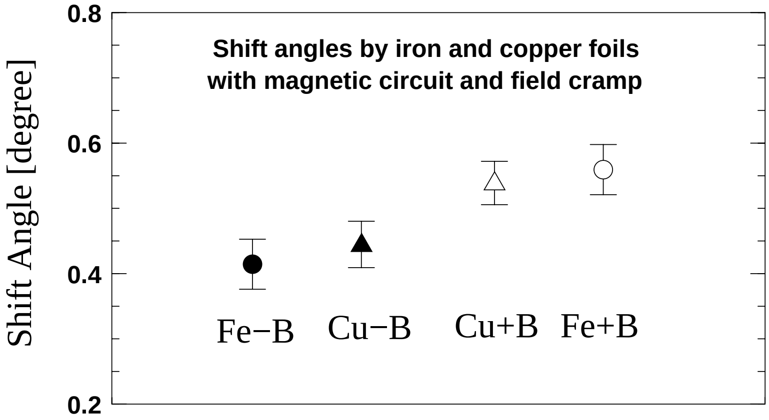

Fig. 4. Results of spin precession for the electric-magnetic experiments.

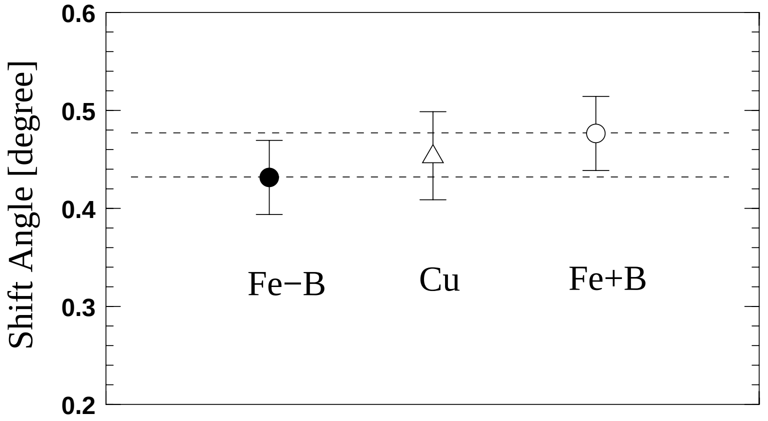

Fig. 5. Spin precessions measured for the stripped foils of permanently magnetized iron foils.

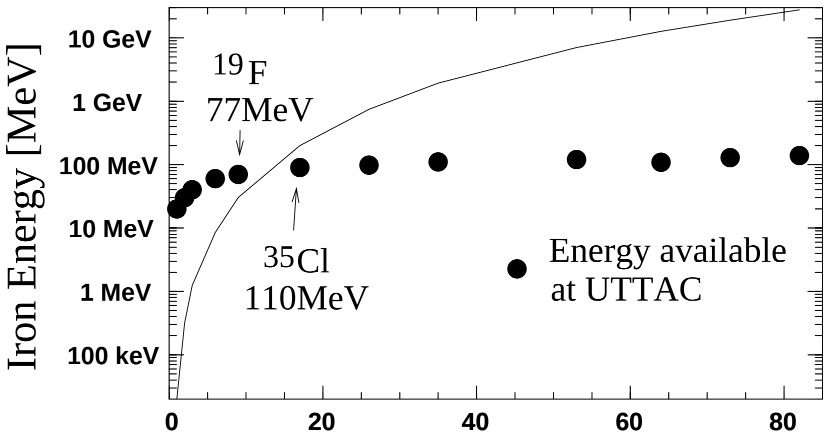

Fig. 6 A solid line shows ion energies corresponding to Bohr velocity. Closed circles indicate the maximum energy available at UTTAC.

2.7 High-spin states in ^{127}I

Y. H. Zhang[1], Y. J. Ma, Y. Sasaki, K. Yamada, H. Ohshima, S. Yokose, M. Ishizuka,
T. Komatsubara, and K. Furuno

Excited states of transitional nuclei $^{117\text{-}127}$I have been investigated previously in Refs. [1-4]. The collective features systematically observed in these nuclei are the occurrence of ΔI=2 bands with stretched $E2$ transitions based on $5/2^+$, $7/2^+$, and $11/2^-$ states, and a ΔI=1 band characterized by $M1$ cascade and $E2$ crossover transitions based on a $9/2^+$ state. The ΔI=1 band was explained as a rotational band based on a deformed $g_{9/2}$ proton hole state. The ΔI=2 bands, on the other hand, have been described as decoupled bands based on the band heads arising from $d_{5/2}$, $g_{7/2}$, and $h_{11/2}$ proton configurations [1-4], respectively. However, the inter-band $M1$+ $E2$ transitions between the members of proposed $d_{5/2}$ and $g_{7/2}$ bands have been found in the recent investigations on ^{121,123}I [5-7] and ^{125}I [7,8]. These authors attributed such coupled structures to the $\pi g_{7/2}$ configuration with admixture of $d_{5/2}$ quasiproton. An oblate shape associated with this band was also proposed [5,6] according to the calculations within the Strutinsky formulism using a Woods-Saxon potential. Calculations within the core-quasiparticle coupling model [9,10] predict the existence of two coupled bands in ^{123,125}I based $\pi g_{7/2}$ and $\pi d_{5/2}$ configurations at low excitation energies. A search for the $\pi d_{5/2}$ coupled band in ^{125}I has been made but no positive evidence has been observed [8]. A previous investigation on ^{127}I [3,4] shows the ΔI=2 sequences of levels based on $5/2^+_1$ (g.s), $7/2^+_1$, and $11/2^-_1$ states up to $21/2^+$, $19/2^+$, and $23/2^-$ respectively. In order to identify new levels and transitions, and for understanding the nature of various bands, the structure of ^{127}I has been reinvestigated by in-beam γ-ray spectroscopic measurements in this work.

The experiment was performed at the Tandem Accelerator Center of University of Tsukuba. We used the ^{124}Sn(^{7}Li,4n)^{127}I reaction to populate the yrast and near-yrast levels in ^{127}I. The ^{7}Li beam was provided by the tandem accelerator in the University of Tsukuba. The target was an enriched self-supporting ^{124}Sn metallic foil of 4 mg/cm^2 thickness. A γ-ray detector array composed of one planar detector and 9 BGO-Compton-suppressed Ge detectors was used for the in-beam γ-ray measurements. Five Ge detectors were positioned at 37^0 and the others near 90^0 with respect to the beam direction so that the DCO ratios (Directional Correlations of γ-ray de-exciting the Oriented states) could be deduced from the coincidence data. All the detectors were calibrated using standard ^{152}Eu and ^{133}Ba sources; typical energy resolution was 2.0~2.5 keV for the 1332 keV line from ^{60}Co source. The beam energy of 32 MeV was used during x-γ and γ-γ-t coincidence measurements. A total of 40 millions γ-γ-t and 3 millions x-γ coincidence events was accumulated. These coincidence events were sorted

---

[1] Institute of Modern Physics, the Chinese Academy of Sciences, Lanzhou 73000, P. R. China

into a symmetric and a non-symmetric (DCO sorting) matrix for off-line analysis.

From detailed analysis on the γ-γ coincidence relationships, γ-ray relative intensities, and DCO ratios, a new level scheme of ^{127}I has been established as shown in Fig. 1, which is largely extended comparing to the previous one [3]. In this work, some high-energy and close-lying double peaks have been identified, and the observed crossover transitions and γ-γ coincidence relationships support the placements of new γ-transitions in the present level scheme.

The negative-parity states labeled as (A) in Fig. 1 are extended from the $23/2^-$ level previously observed [3] up to $(35/2^-)$ state at 5243 keV excitation energy. The 374 keV line feeding to the $23/2^-$ level [3] has not been observed in this work. The deduced DCO ratios show stretched quadrupole characters for 982-, 1013-, and 601-keV γ-rays and dipole characters for 410- and 274-keV lines. These results support the spin and parity assignments for the levels above $23/2^-$ state. A sequence of levels based on $11/2^-$ state has been observed in $^{119\sim127}$I and explained as decoupled bands based on the $h_{11/2}$ proton configurations [1-4]. The decoupled nature of these bands is inferred from the similar energy level spacings with those of the corresponding even-even cores. This is really the case comparing the negative-parity states in ^{127}I with the ground-state band in ^{126}Te [11] which is presented in Fig. 1 by black dots. The similar level spacings suggest that the negative-parity levels from $11/2^-$ through $(27/2^-)$ are formed by coupling the aligned $h_{11/2}$ proton to the core states from 0^+ through 8^+.

The two ΔI=2 sequences of band (C) have been established previously [3] up to $19/2^+$ and $21/2^+$, respectively, by adding 880- and 934-keV transitions to the yrast $15/2^+$ and $17/2^+$ states. These two γ rays may be the 877- and 930-keV lines observed in this work. Several parallel crossover transitions de-exciting a new level at 2901 keV support the placements of the associated γ transitions and γ-ray energies determined in this work. Three new γ rays (912, 812, and 851 keV) are observed and placed in the level scheme extending the ΔI=2 sequences up to $(25/2^+)$ and $(23/2^+)$ respectively. The deduced DCO ratios show stretched quadrupole characters for 912-, 812-, 850- 545-, 930-, and 1171-keV γ rays, and dipole characters for 113-, 95-, 156-, and 294-keV lines supporting the spin and parity assignments shown in the figure. Above $(23/2^+)$ state at 2901 keV, a ΔI=1 cascade with weak crossover transitions has also been observed. This band is probably a 3-qp band.

The two ΔI=2 cascades of band (C) have been described in Refs. [1,4] as decoupled bands based on the bandheads arising from $d_{5/2}$ and $g_{7/2}$ proton configurations, respectively. The strong inter-band band transitions (593- and 550-keV γ rays) between these ΔI=2 sequences suggest that these ΔI=2 bands have similar configuration with a large overlap in their wave functions. Other inter-band transitions (214-, 396-, 481-, and 432-keV γ rays) are also observed connecting states up to $21/2^+$ at 2788 keV. Based on this and systematics of similar bands and decay patterns in the neighboring iodine nuclei [5-8], the two yrast ΔI=2 bands may be interpreted as signature partners of same configuration. The $\alpha=-1/2$ signature branch is favored in energy, therefore, the main component may be the $g_{7/2}$ proton configuration. The 651-keV transition is assigned as out-of-band decay as arranged in Fig. 1.

Apart from the yrast positive-parity band discussed above, two new ΔI=2 cascades labeled as band (B) have been newly observed feeding to the second $7/2^+$ and $9/2^+$ states. The linking transitions with $h_{11/2}$ decoupled band and $g_{7/2}$ band fix the ordering and the spin-parity of associated levels. On the other hand, weak inter-band transitions (116-, 562-, and 475-keV lines) are also observed. These two ΔI=2 cascades are very probably based on the $d_{5/2}$ proton configuration. The observation of both $\pi d_{5/2}$ and $\pi g_{7/2}$ bands is consistent with theoretical predictions within the core-quasiparticle coupling model [9,10].

References:

1) D. M. Gordon, M. Gai, A. K. Gaigalas et al., Phys. Lett. **B67**, 161 (1977)
2) U. Hagemann, H. J. Keller, and H. F. Brinckmann, Nucl. Phys. **A289**, 292 (1977)
3) R. E. Shroy, D. M. Gordon, M. Gai et al., Phys. Rev. **C26**, 1089 (1982)
4) M. Gai, D. M. Gordon, R. E. Shroy et al., Phys. Rev., **C26**, 1101 (1982)
5) Y. Liang, D. B. Fossan,, J. R. Hughes et al., Phys. Rev. **C45**, 1041 (1992)
6) Y. Liang, D. B. Fossan, J. R. Hughes et al, Proceedinds of the International Conference on High Spin Physics and Gamma-soft Nuclei, Saladin J X et al ed. (World Scientific Press, Sigapore) 1991. 308-314
7) R. Goswami, B. Sethi, P. Banerjee, Phys. Rev. **C47**, 1013 (1993)
8) H. Sharma, B. Sethi, R. Goswami et al., Phys. Rev. **C59**, 2446 (1999)
9) F. Donau, U. Hagemann, Z. Phys. **A293**, 31 (1979)
10) L. G. Kostova, W. Andrejtscheff, L. K. Kostov et al., Nucl. Phys. **A485**, 31 (1988)
11) C. T. Zhang, P. Bhattacharyya, P. J. Daly et al., Nucl. Phys. **A628**, 386 (1998)

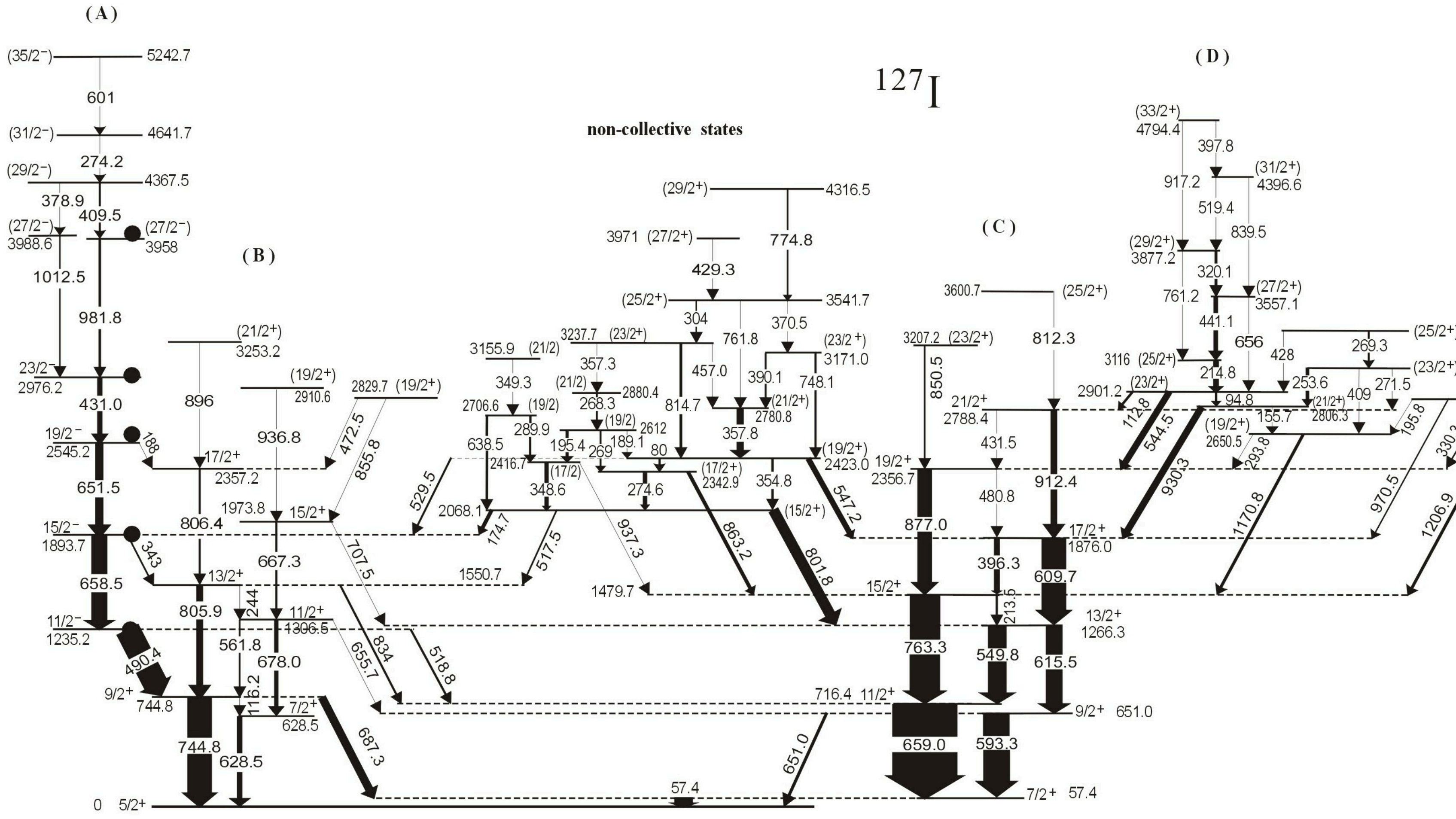

Fig. 1 Partial level scheme of ^{127}I deduced from the present work. Excitation energies of $0^+, 2^+, \ldots 8^+$ states in ^{126}Te [11] relative to $11/2^-$ level in ^{127}I are indicated as black dots.

2.8 Determination of excitation energies and level structure in high-spin states of ^{116}I

C.-B. Moon*, T. Komatsubara, T. Shizuma, Y. Sasaki, K. Uchiyama, K. Matsuura, M. Murasaki,
H. Takahashi and K. Furuno

* Department of Physics, Hoseo University, Chung-Nam 336-795, Korea
E-mail: cbmoon@office.hoseo.ac.kr

1. Introduction

A few years ago, a preliminary result about the in-beam spectroscopy of ^{116}I was given in this annual report [1] still leaving excitation energies to be unknown. Here, we report that the excitation energies of states in ^{116}I have been determined. Before the present work, the excitation energies for the observed deformed bands have been unknown, although several investigations for the level structure of ^{116}I by using in-beam spectroscopy were done [2-4]. Consequently, the bands observed in this nucleus could not be connected and thus remained to be isolated from each other,

The level structure was studied with the ^{103}Rh(^{16}O, 3n)^{116}I reaction at a beam of 80 MeV. The beam was provided by the 12UD tandem accelerator at the University of Tsukuba. The ^{103}Rh target was a foil of 1.0 mg/cm^2 in thickness on the Pb backing of 3 mg/cm^2 in thickness. The γ-ray spectra were taken with 7 high-purity (HP) Ge detectors with BGO anti-Compton shields (ACS). One of them was the low energy photon (LEP) detector to ensure sensitivity for important low-energy transitions at the bottom parts of γ-ray cascades. For the DCO ratios, the coincidence events were sorted into an asymmetric matrix with energies of γ rays detected in 5 detectors at 117^0 along one axis and energies of γ rays detected in a detector at 0^0 along the other axis. The intensities of $I_\gamma(117^0)$ and $I_\gamma(0^0)$ used to determine the DCO ratio, $R = I_\gamma(117^0)/I_\gamma(0^0)$, for the transitions of interest were extracted from spectra obtained by setting gates on the 117^0 and 0^0 axes of the γ–γ asymmetric matrix. Measured angular correlation ratios, $R = I_\gamma(37^0)/I_\gamma(79^0)$, are included in Table 1 together with excitation energies, relative intensities and spin-parity assignments of the transitions in ^{116}I.

2. Level scheme of ^{116}I

a. Low-spin states labeled 1

Fig.1 shows the level scheme of ^{116}I deduced from the present work. The ordering of the γ-ray transitions has been derived from coincidence relationships and relative intensities. Information on γ-ray multipolarities was obtained from DCO ratios as mentioned earlier.

The low-lying states labeled 1 between the ground 1$^+$ state and the (10$^+$) state at 1097.3 keV were definitely established in the present work. Thereby, excitation energies for the observed deformed rotational bands have been determined. It should be emphasized that there is no ambiguity in the transition order in these low-lying states because all the transitions are, as shown in Fig.1, intertwined with each other through the crossing-over transitions. The DCO ratios indicate that the 227-keV transition shows ΔI = 2 type of quadrupole in nature while the 114-keV transition of dipole character. Unlike other neighboring odd-odd isotopes with the ground state of 2$^-$, the spin-parity of the ground state of ^{116}I has been known to be 1$^+$. We propose that the state at 227 keV should be 3$^+$. By the intensity balance arguments for the 114-keV transition, the multipolarity is suggested to be E1 rather than M1 as shown in Table 2 and thus the spin-parity of the state at 341.1 keV is likely 4$^-$. The 149.5-keV transition feeding the 227-keV state by crossing over the 341.1-keV state was found to be of quadrupole character. So the spin-parity of the 376.5-keV state might be 5$^+$. This state was fed mainly by the 92-keV transition and weakly by the 195- and 142.5-keV transitions. The multipolarity for the 92-keV transition was indicative of dipole character in the DCO ratios. In the mean time, the spin-parity of the 468.5-keV state on which band 3 is built was assigned to be 8$^-$. As shown in Fig. 1, the 92-keV transition is depopulated from this state and thus its multipolarity should be E3. From the point of view about the intensity balance argument, however, E2 or M2 cannot be excluded.

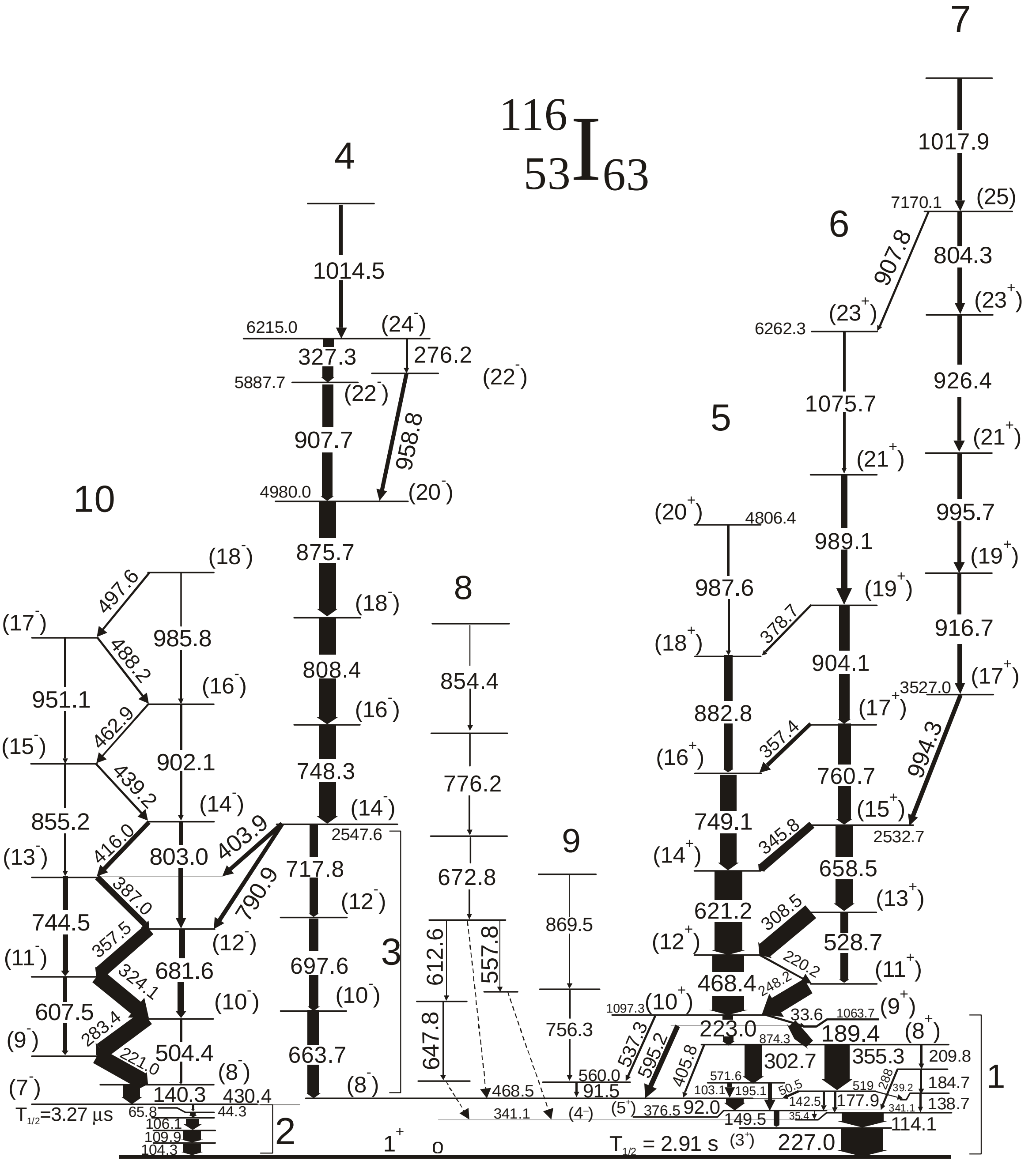

Fig.1 Level scheme of ^{116}I deduced from the reaction ^{103}Rh(^{16}O,3n)^{116}I at a beam energy of 80 MeV. Transition and excitation energies are given in keV.

Two strongly populated transitions, which are the 355.3- and 302.7-keV ones, from the 8^+ state at 874.3 keV are noticeable. Surprisingly, depopulating γ-rays from the states fed by these two transitions are fragmented into a lot of weak-intensity transitions among which the 50.5- and 39.2-keV ones are very low in energy. The DCO ratios indicate that these 355.3- and 302.7-keV transitions are of dipole character and thus the spin of the 519.0- and 571.6-keV states is likely 7. This means that the depopulating transitions would have quite high multipolarities, such as λ = 2 or 3. It is well known that γ-rays decaying from an isomer might be of high multipolarity transitions. The present result, therefore, opens a question that there would be some isomers in these low-lying states.

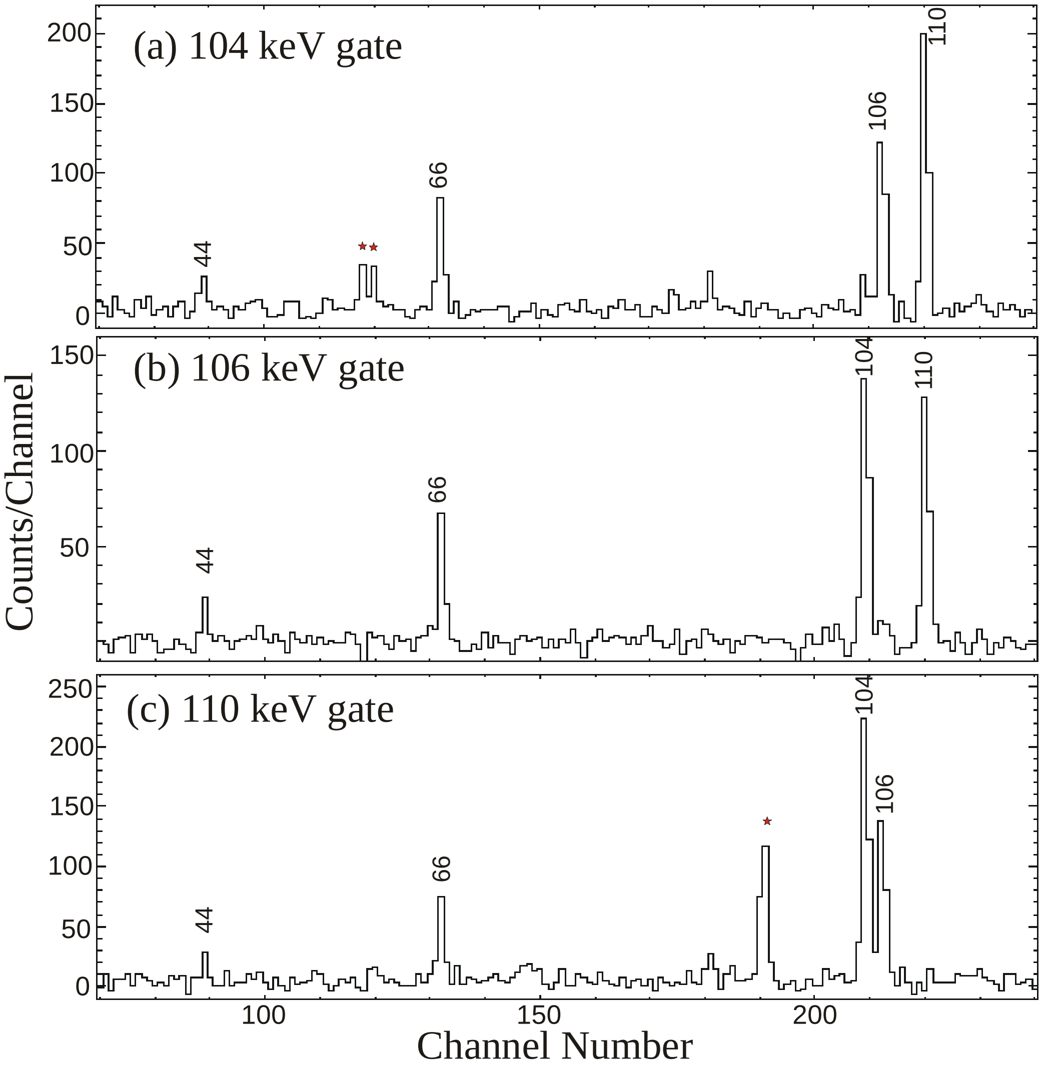

Fig.2. γ-ray spectra detected by a LEP in coincidence with the 104-, 106- and 110-keV transitions. Energies are given in keV.

b. Low-lying states labeled 2

Before the present work, the excitation energy of the 7^- isomer with half-life of 3.27 μs was not known. The spin-parity assignment for this state was made following the systematics of the $\pi g_{9/2}\nu h_{11/2}$ deformed bands observed in the neighboring heavier isotopes [4]. This isomer was identified and its life-time was measured by Wu et al [5]. Two independent branches associated with the decay of this isomer were observed [5]: one includes 65.4-,105-(a doublet), and 109.6-keV transitions and the other 114.2-and 227.2-keV transitions. In the present work, the excitation energy of this isomer was found to be 430.4 keV. This result came from the coincident relationship between band 3 built on the 8^- state at 468.5 keV and excited states built on this isomer (see Fig. 1). If this result is correct, a missing transition should be observed together with the 65.4-,105-(a doublet), and 109.6-keV transitions. In other words, the 44.3-keV transition that corresponds to the energy difference between the 430.4 keV and the sum energy, 386.1 keV, of the 65.8-, 104.3-, 106.1- and 109.9-keV transitions should exist below this isomer. It is noted that a doublet 105 keV transition could be separated into the 104.3- and 106.1-keV transitions. In the present work, such a 44.3-keV transition could be identified. As shown in Fig. 2, the 44-keV peak is clearly seen in spectra gated by the 104-, 106- and 110-keV transitions. Some useful informations for the transitions below this isomer are presented in Table 2 where relative intensities, experimental internal coefficients and theoretical internal coefficients are included. The present experimental internal coefficients were derived from the intensity balance arguments assuming the 110-keV transition that should be E2 since it was shown to be of dipole character in DCO ratios.

Closely looking at the summed delayed γ-ray spectrum in [5], we find two small peaks that were not noticed by the authors, which are the 89- and 150-keV peaks. Interestingly, the 89-keV peak is equivalent to the transition energy between the isomer at 430.4 keV and the 341.1-keV state. If this 89-keV peak is a real transition from this isomer, it is possible to explain the reason why the 227-and 114-keV transitions were observed in the delayed γ-ray spectrum in [5]. Furthermore, the 150-keV peak may correspond to the 149.5-keV transition from the 376.5-keV state to the 227-keV state.

c. Bands 3 and 4

Band 3, which comprises the 663.7-, 697.6-, and 717.8-keV transitions, was newly identified in the present work. As was already mentioned, the observation of this band made it possible to extract the excitation energy of the isomer to be 430.4 keV. The 14^- state at 2547.6 keV, on which more strongly populated transitions are built, might be based on the four-quasiparticle configuration. The spin-parity assignment for this state was suggested to be 13^- in a previous work [2]. We propose that, however, its spin-parity should be 14^-. The present spin-parity assignments are essentially based on the multipolarity of the interband transitions connecting band 10, namely the 403.9- and 790.9-keV transitions. The DCO ratios indicate that the 403.9 keV is $\Delta I=1$ transition with mixed M1/E2 while the 790.9-keV one is of quadrupole character indicating $\Delta I=2$ transition with E2. Furthermore, by taking into account of the γ-ray intensity at a given angular momentum in band 4 and band 10, the present assignment is more reliable than that of former result [2].

Band 4 was already identified in [2].

d. Bands 5 and 6

These bands built on the 8^+ state at 874.3 keV, to which we assign positive parity, are well developed into rotational structure above the 10^+ and 11^+ states. The positive-parity assignment could be made by assuming that they should be based on the $\pi h_{11/2}\nu h_{11/2}$ configuration. The present assignment can be justified by arguing the fact that negative-parity states based on the proton $h_{11/2}$ orbital was most strongly populated in the neighboring odd-A I, such as ^{115}I [6] and ^{117}I [7]. Interestingly, one can see a similar pattern in the positive-parity bands in odd-odd ^{120}Cs [8] and ^{122}Cs [9] where signature inversion feature was revealed at lower spin states. More higher-spin states in these bands were established by Paul et al. [3] using the Eurogam spectrometer and the positive-parity assignment was made to these bands with a $\pi h_{11/2}$ $\nu h_{11/2}$ structure on the basis of blocking arguments of a neutron $h_{11/2}$ pair and a proton $h_{11.2}$ pair alignments.

e. Band 7

This band is somewhat pecular. First, the transition intensity is all most the same by showing no side feeding transitions between the 3527- and 7170-keV states. Second, the transition energy is quite irregular that shows no rotational structure. Finally, this band is strongly correlated with the 23^+ state in band 6 through the 907.8-keV side-feeding transition.

The underlying physics involved in this band has not yet known. A possible explanation, however, may be put so that it might originate from correlations between the $\pi h_{11/2}\nu h_{11/2}$ configuration and the vibrational motion seen in the neighboring even-even Te core. Such a quasi γ-band built by the coupling of the proton $h_{11/2}$ orbital and the vibrational band were observed in odd-even ^{117}I [7]and ^{119}I [10].

f. Bands 8 and 9

Band 8 was newly identified but could not be established its excitation energy. The population intensity for band 8 was estimated to be about 8 % relative to that of the 227-keV transition. Band 9 was also newly observed in the present work. These two bands may be associated with the $\pi g_{7/2}\nu h_{11/2}$ configuration.

g. Band 10

This band has been well known as being based on the proton hole $g_{9/2}$ orbital coupled to the neutron $h_{11/2}$ orbital in previous works. In the present work, some more higher-lying transitions were identified.

References

[1] C.-B. Moon et al., Tandem Accelerator Center Annual Report, UTTAC-65 (1998).

[2] E.S. Paul, R.M. Clark, S.A. Forbes, D.B. Fossan, J.R. Hughes, D.R. LaFosse, P.J. Nolan, P.H. Regan, P. Vaska, R. Wadsworth and M.P. Waring, J. Phys. G: Nucl. Part. Phys. 19 (1993) 343.

[3] E.S. Paul, D.B. Fossan, K. Hauschild, I.M. Hibbert, H. Schnare, J.M. Sears, I. Thorslund, R. Wadsworth, A.N. Wilson, and J.N. Wilson, J. Phys. G: Nucl. Part. Phys. 21 (1995) 995.

[4] M.A. Quader, W.F. Piel, S. Vajda, W.A. Watson III, F.C. Yang, and D.B. Fossan, Phys. Rev. C 30 (1984) 1772.

[5] C.Y. Wu, M. Satteson, K. Wang, D. Cline, H.E. Gove, S.S. Hanna, M. Hass, R. Ibbotson and A.V. Ramayya, Phys. Rev. C 41 (1990) 1600.

[6] C.-B. Moon, T. Komatsubara and K. Furuno, Tandem Accelerator Center Annual Report, UTTAC-68 (2000), p.49.

[7] C.-B. Moon, T. Komatsubara, T. Shizuma, Y. Sasaki, H. Ishiyama, T. Jumatsu and K. Furuno, Eur. Phys. J. A 5 (1999) 13.

[8] C.-B. Moon, S.J. Chae, J.H. Ha, T. Komatsubara, Y. Sasaki, T. Jumatsu, K. Yamada, K. Satou and K. Furuno, Nucl. Phys. A 696 (2001) 45.

[9] C.-B. Moon, T. Komatsubara and K. Furuno, Nucl. Phys. A 674 (2000) 343.

[10] S. Törmänen, S. Juutinen, R. Julin, A. Virtanen, G.B. Hagemann, Ch. Droste, W. Karczyk, T. Morek. and J. Srebrny, Nucl. Phys. A 613 (1997) 282.

Table 1. Level energies, γ–ray energies, DCO ratios, and spin-parity assignments to ^{116}I following the ^{103}Rh(^{16}O,3n)^{116}I reaction at a beam energy of 80 MeV.

E_i (keV)	E_f (keV)	E_γ(keV)	I_γ[a]	R[b]	Multipolarity	Assignment
1097.3	1063.7	33.6			M1/E2	$(10^+)\rightarrow(9^+)$
376.5	341.1	35.4				$(5^+)\rightarrow(4^-)$
519.0	479.8	39.2				
519.0	468.5	50.5				$(7)\rightarrow(5^+)$
560.0	468.5	91.5*				
468.5	376.5	92.0*	285	0.6	dipole	$(8^-)\rightarrow(5^+)$
571.6	468.	103.			dipole	$(7)\rightarrow(8^-)$
341.1	227.0	114.1	925	0.4	E1	$(4^-)\rightarrow(3^+)$
479.8	341.1	138.7	97		dipole	
570.7	430.4	140.3	250	0.6	M1/E2	$(8^-)\rightarrow(7^-)$
519.0	468.5	142.5	26	0.6	dipole	$(7)\rightarrow(5^+)$
376.5	227.0	149.5	89	0.8	E2	$(5^+)\rightarrow(3^+)$
519.0	341.1	177.9	38	0.9		$(7)\rightarrow(4^-)$
664.5	479.8	184.7	75	0.6	dipole	
1063.7	874.3	189.4	455	0.4	M1/E2	$(9^+)\rightarrow(8^+)$
571.6	468.5	195.1	89	0.7		$(7)\rightarrow(5^+)$
874.3	664.5	209.8	38	0.4	dipole	
1505.7	1345.5	220.2	81		M1/E2	$(12^+)\rightarrow(11^+)$
791.7	570.7	221.0	285	1.0[c]	M1/E2	$(9^-)\rightarrow(8^-)$
1097.3	874.3	223.0	277	0.9	E2	$(10^+)\rightarrow(8^+)$
227.0	0	227.0	1000	1.0	E2	$3^+\rightarrow1^+$
1345.5	1097.3	248.2	210		M1/E2	$(11^+)\rightarrow(10^+)$
6215.0	5938.8	276.2	34		E2	$(24^-)\rightarrow(22^-)$
3872.9	3026.2	283.4	220	1.0[c]	M1/E2	$(10^-)\rightarrow(9^-)$
874.3	571.6	302.7	193	0.5	dipole	$(8^+)\rightarrow(7)$
1874.2	1505.7	308.5	225	0.4	M1/E2	$(13^+)\rightarrow(12^+)$
1399.2	1075.1	324.1	181	1.0[e]	M1/E2	$(11^-)\rightarrow(10^-)$
6215.0	5887.7	327.3	120	1.5[c]	E2	$(24^-)\rightarrow(22^-)$
2532.7	2186.9	345.8	142	0.5	M1/E2	$(15^+)\rightarrow(14^+)$

Table 1. Continued

E_i (keV)	E_f (keV)	E_γ (keV)^a	$I_\gamma{}^a$	R^b	Multipolarity	Assignment
874.3	519.0	355.3	382	0.5	dipole	$(8^+)\rightarrow(7)$
3293.4	2936.0	357.4	74	0.5	M1/E2	$(17^+)\rightarrow(16^+)$
1756.7	1399.2	357.5	164	1.1^c	M1/E2	$(12^-)\rightarrow(11^-)$
4197.5	3818.8	378.7	33		M1/E2	$(19^+)\rightarrow(18^+)$
2143.7	1756.7	387.0	98	1.1^c	M1/E2	$(13^-)\rightarrow(12^-)$
2547.6	2143.7	403.9	51	1.1^c	M1/E2	$(14^-)\rightarrow(13^-)$
874.3	468.5	405.8	26	1.1		$(8^+)\rightarrow(8^-)$
2559.7	2143.7	416.0	56	1.2^c	M1/E2	$(14^-)\rightarrow(13^-)$
2998.9	2559.7	439.2	21	1.1^c	M1/E2	$(15^-)\rightarrow(14^-)$
3461.8	2998.9	462.9	21	1.1^c	M1/E2	$(16^-)\rightarrow(15^-)$
1565.7	1097.3	468.4	614	1.1	E2	$(12^+)\rightarrow(10^+)$
3950.0	3461.8	488.2	17		M1/E2	$(17^-)\rightarrow(16^-)$
4447.6	3950.0	497.6	12		M1/E2	$(18^-)\rightarrow(17^-)$
1075.1	570.7	504.4	35	1.7^c	E2	$(10^-)\rightarrow(8^-)$
1874.2	1345.5	528.7	104	1.0	E2	$(13^+)\rightarrow(11^+)$
537.3	560.0	537.3	45	0.6	(E1)	$(10^+)\rightarrow(9^-)$
1063.7	468.5	595.2	85	0.5	(E1)	$(9^+)\rightarrow(8^-)$
1399.2	791.7	607.5	55	1.4^c	E2	$(11^-)\rightarrow(9^-)$
2186.9	1565.7	621.1	405	1.0	E2	$(14^+)\rightarrow(12^+)$
2532.7	1874.2	658.5	197	1.1	E2	$(15^-)\rightarrow(13^-)$
1132.2	468.5	663.7	183	1.0	E2	$(10^-)\rightarrow(8^-)$
1756.7	1075.1	681.6	71	1.8^c	E2	$(12^-)\rightarrow(10^-)$
1829.8	1132.2	697.6	157	1.0	E2	$(12^-)\rightarrow(10^-)$
2547.6	1829.8	717.8	101	1.0	E2	$(14^-)\rightarrow(12^-)$
2143.7	1399.2	744.5	66	1.7^c	E2	$(13^-)\rightarrow(11^-)$
3295.9	2547.6	748.3	270	1.0	E2	$(16^-)\rightarrow(14^-)$
2936.0	2186.9	749.1	210	1.1	E2	$(16^+)\rightarrow(14^+)$
3293.4	2532.7	760.7	160	1.1	E2	$(17^+)\rightarrow(15^+)$
2547.6	1756.7	790.9	59	1.7^c	E2	$(14^-)\rightarrow(12^-)$
2559.7	1756.7	803.0			E2	$(14^-)\rightarrow(12^-)$
7170.1	6365.8	804.3	80	1.1	E2	$(25)\rightarrow(23)$
4104.3	3295.9	808.4		1.0	E2	$(18^-)\rightarrow(16^-)$

Table 1. Continued

E_i (keV)	E_f (keV)	E_γ (keV)	I_γ[a]	R[b]	Multipolarity	Assignment
2998.9	2143.7	855.2	32		E2	$(15^-)\rightarrow(13^-)$
4980.0	4104.3	875.7	220	1.1	E2	$(20^-)\rightarrow(18^-)$
3818.8	2936.0	882.8	98	0.9	E2	$(18^+)\rightarrow(16^+)$
3461.8	2559.7	902.1			E2	$(16^-)\rightarrow(14^-)$
4197.5	3293.4	904.1	105	1.1	E2	$(19^+)\rightarrow(17^+)$
5887.7	4980.0	907.7	128	1.0	E2	$(22^-)\rightarrow(20^-)$
7170.1	6262.3	907.8	80	0.9	E2	$(25^+)\rightarrow(23^+)$
4443.7	3527.0	916.7	93	1.0	E2	$(19^+)\rightarrow(17^+)$
6365.8	5439.4	926.4	66	1.0	E2	$(23^+)\rightarrow(21^+)$
3950.0	2998.9	951.1	18		E2	$(17^-)\rightarrow(15^-)$
5938.8	4980.0	958.8	50		E2	$(22^-)\rightarrow(20^-)$
4447.6	3461.8	985.8	9		E2	$(18^-)\rightarrow(16^-)$
4806.4	3818.8	987.6	27		E2	$(20^+)\rightarrow(18^+)$
5186.6	4197.5	989.1	82	1.1	E2	$(21^+)\rightarrow(19^+)$
7229.5	6215.0	1014.5	67			
8188.0	7170.1	1017.9	82	0.5	dipole	
6262.3	5186.6	1075.7	40		E2	$(23^+)\rightarrow(21^+)$

a: Error are estimated to be less than 10% of the quoted values for the transitions with $I_\gamma > 100$ and less than 25% for the weaker ones. The values are normalized to 1000 for the 227-keV transition.

b: $R=Y_\gamma(0^0)/Y_\gamma(117^0)$

c: DCO ratios from the gate on 140 keV M1/E2 transition.

* γ ray is a doublet.

Table 2. Intensity, experimental and theoretical internal conversion coefficients for the transitions below the 7^- isomer in ^{116}I.

E (keV)	I_γ[a]	Experimental Conversion Coefficients[b]	Theoretical Internal Conversion Coefficients						
			E1	E2	E3	E4	M1	M2	M3
44.3	4(1)	9.66	1.63	10.2	39.7	140	6.86	130	920
65.8	11(3)	1.13	0.579	4.31	24.1	129	2.24	30.7	248
104.3	31(3)	0.386	0.157	1.07	6.10	30.7	0.581	5.33	37.1
106.1	21(3)	1.13	0.151	1.02	5.54	29.1	0.557	5.06	35.0
109.9	28(2)	0.507	0.136	0.914	4.94	25.7	0.507	4.50	30.6

a: Intensity has been derived from the spectrum gated on Iodine X-ray of 28 keV.

b: Assume that the 110-keV transition should be M1.

2.9 Detection of Rn-flux in the atmosphere

K. Shiga and Y. Tagishi

The most part of the daughter nuclei produced from radioactive decay of radon (^{222}Rn) and thoron (^{220}Rn) are positively charged. Therefore these nuclei can be collected electro-statically by supplying negative voltage. We applied first to the silicon solid-state detector (SSD) for the direct detection of these alpha particles [1]. A PIN silicon photodiode from HAMAMATSU (active area of 48×48 mm^2, S4276-2) is used by applying a bias of –100 V on the front surface of the detector. We can obtain energy signals of the alpha particles from radioactive decay of the daughter nuclei of radon and thoron.

In order to obtain the absolute values of the radon content in the air, we measured the collecting efficiency of positively charged ^{218}Po ions (daughter nuclei of radon, $T_{1/2}$=3 min.) on the surface of the silicon detector. The silicon detector was mounted in a chamber (350 mm in diameter and 200 mm in depth) filling with 1-atm air of the target room at UTTAC. Counting rate of the alpha particles emitted from ^{218}Po (energy of 6.0 MeV) was measured by varying the pressure inside the chamber from 1 to 0.1 atm. Results are shown in Fig. 1, where x-axis presents various pressures in the chamber and y-axis presents yields of alpha particles emitted from ^{218}Po divided by the pressure in the chamber. At lower pressures the yields divided by the pressure inside the chamber saturate to the constant values. Because at the lower pressures the mean-free path of the ^{218}Po ion increases, the most of the ^{218}Po ions reach to the surface of the detector. Then the saturate values are corresponding to the whole numbers of ^{218}Po ions in the chamber under pressure of 1-atm. We estimated the collection efficiency of ^{218}Po ions to be 28% at 1-atm in the chamber.

Next we checked the linearity of the detected yields of the alpha particles with energy of 6.003MeV to the quantity of the ^{218}Po ions. First the chamber was filled with 1-atm N_2 gas containing ^{222}Rn. We measured yields of alpha particles with energy of 6.003MeV. We controlled the number of Rn in the chamber as follows: First, we evacuated the chamber to about 0.8-atm. Second, we filled the chamber with pure N_2 gas (no concentration of Rn) to 1-atm. Third, we measured yields of alpha particles. By repeating these processes, we obtained the yields of detecting alpha particles for various Rn density in the chamber with 1-atm. Results are shown in Fig. 2. We made sure that we could measure the Rn-flux by filling the chamber with various atmosphere.

References

[1] T. Iizuka, M. Aida and Y. Tagishi, UTTAC annual report (1999) 33

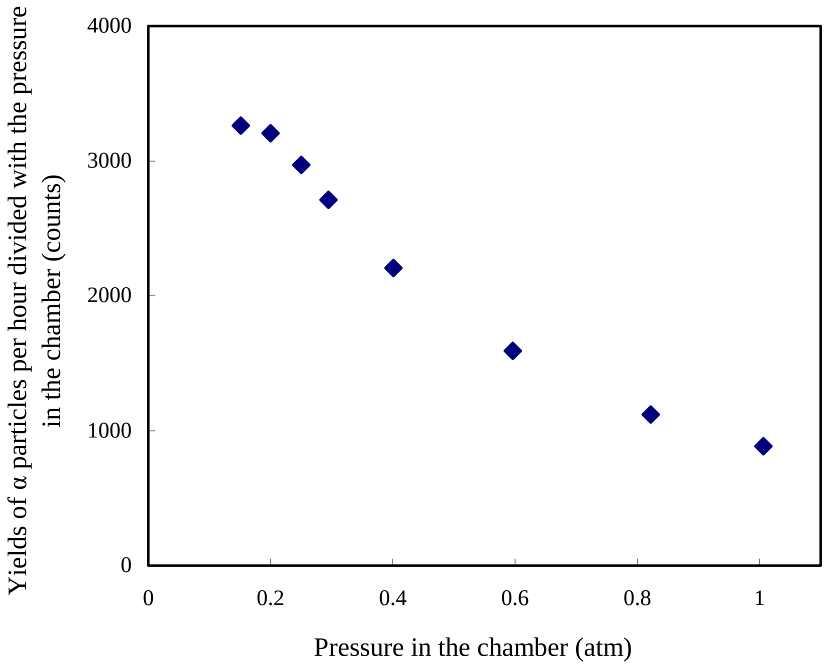

Fig. 1. Relation between various pressures in the chamber and the corresponding yields of alpha particles with energy of 6.003 MeV divided with pressure in the chamber.

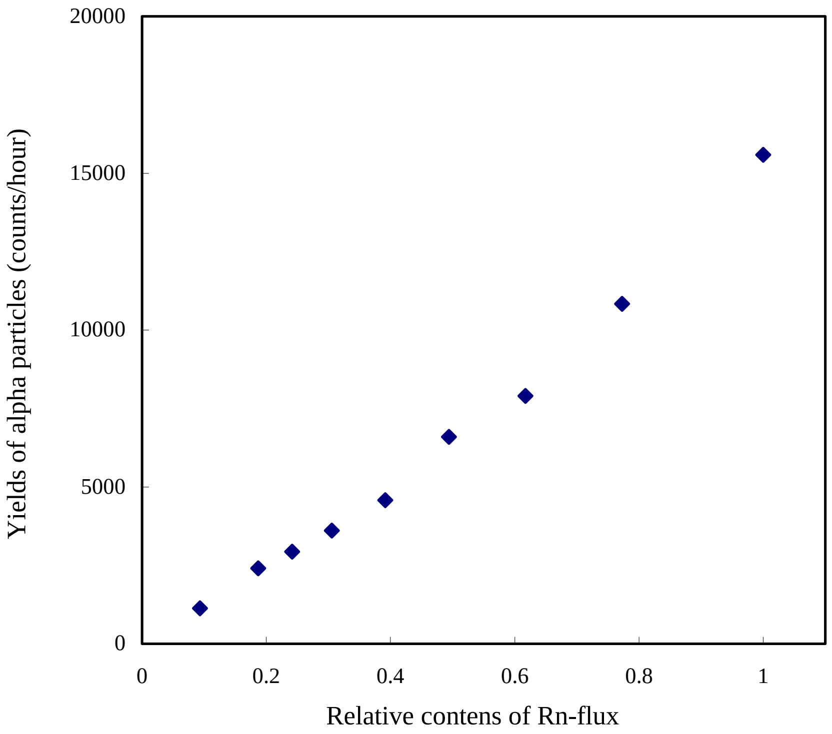

Fig. 2. Relation between the density of ^{222}Rn-flux and yields of alpha particles from ^{218}Po.

3.1 Resonant ionization of channeled dressed ions in a crystal field

H. Kudo, K. Takeda, W. Iwazaki, T. Suguri, C. Sakurai, S. Numazawa, I. Arano, S. Seki[1]

When partially ionized ("dressed") ions are incident on solids, some of the bound electron(s) of the ions are stripped when the input charge is lower than the equilibrium charge in the solid, which depends mainly on the velocity of the ions. The released electrons are referred to as loss electrons. The kinetic energy of the loss electrons are distributed around the loss-peak energy E_L, which is equal to the kinetic energy of the electron moving at the same speed as the ion. We have recently measured loss electrons emitted from crystal targets. The aim of the study is to observe the resonant ionization as a result of the resonant coherent excitation (REC, or the *Okorokov effect*) due to a periodical electrostatic field in a crystal lattice. Technically, this is the first attempt to observe REC in a backward direction, in contrast to the transmission experiments or specular-reflection measurements so far adopted for the REC studies. [1, 2, 3]

The C^{4+} and C^{6+} beams in the MeV/u energy range were obtained at UTTAC. The electron energy spectra emitted from Si and Ge crystals were measured at 180° with respect to the beam direction [4], using the 45° parallel-plate spectrometer of the double deflection type under the pressure of $\sim 3\times 10^{-7}$ Pa. This layout has a characteristic feature that the continuum energy spectrum is independent of the tilt angle of the target surface.

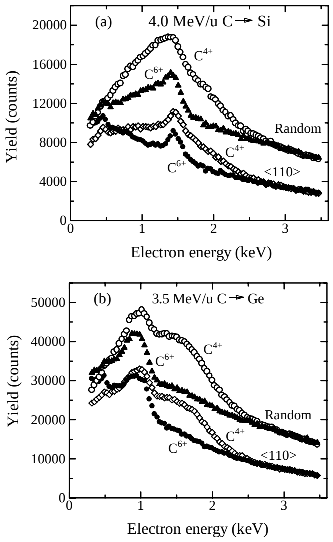

Figure 1: Energy spectra of secondary electrons emitted from Si and Ge, bombarded by the dressed and fully-stripped ions.

Figure 1 shows energy spectra of the secondary electrons induced by 3.5 and 4.0 MeV/u C^{4+} and C^{6+} for $\langle 110\rangle$ and random incidence on Si and Ge crystals. The electron yields are normalized to a same number of the incident ions. Each pair of the spectra in Fig. 1 are shown so that the yields in the high energy side (3.0–3.5 keV) are the same. Indeed, the high energy side of the observed spectra for C^{4+} and C^{6+} are overlapped typically within an uncertainty of ±10%. Since $E_\mathrm{L} = 1.91$ and 2.18 keV for 3.5 and 4.0 MeV/u C ions, respectively, the measured spectra cover most of the electron energy range to which the loss electrons contribute.

The fully stripped C^{6+} hardly capture target electrons and, therefore, the electron yield results mainly from the binary-encounter processes between the ion and target electrons. Accordingly, we may assume

---

[1] SSL Tsukuba

that the loss electron yield is approximately given by the difference between the yield for C^{4+} and C^{6+} in Figs. 1(a) and (b), respectively. It should be noted that there is a cross point at 0.5–0.8 keV in each pair of the spectra for $\langle 110 \rangle$ and random cases. Furthermore, the cross-point energy is slightly higher for the $\langle 110 \rangle$ than for the random case. This is due to the lower production cross sections of the binary-encounter electrons for C^{4+} than for C^{6+} in soft collisions with target atoms. Actually, in the low-energy limit of the electron energy, the ratio of the cross sections for C^{6+} to C^{4+} can be roughly estimated as $(6/4)^2 = 2.25$, from the projectile-charge dependence of the production cross section of binary-encounter electrons [5]. The production cross section of the low-energy electons should be lower for the channeling case since soft collisions are dominant in contrast to the random case, which gives rise to the higher cross-point energy than in the random case.

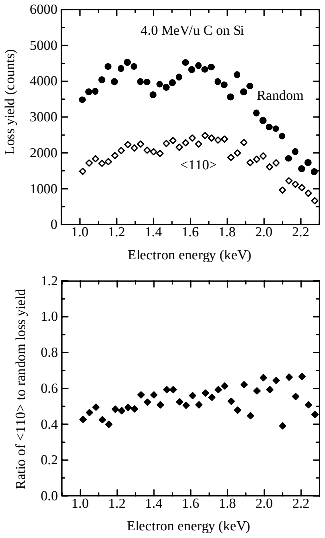

Figure 2: Energy spectra of the loss electrons (top), and the ratio of the loss yiled for $\langle 110 \rangle$ to the random case (bottom).

Figure 2 shows energy spectra of the loss electrons, i.e., the C^{4+} yield subtracted by the C^{6+} yield, and the ratio of $\langle 110 \rangle$ to random loss yield. The ratio is 0.5-0.6 in the energy range 1.0–2.0 keV in consideration. This value is consistent with a previous work [4], in which it was concluded that C^{4+} typically loses 1 electron when it is channeled, while ∼2 electrons are lost in the random case.

Axially channeled ions experience periodic electric field with a frequency of v/d, where v is the ion velocity and d is the atomic spacing along the axial direction. RCE is therefore expected to occur when the electron excitation energy of the dressed ions, ΔE, satisfies $\Delta E = Nv/d$ ($N = 1, 2, 3, \ldots$).

In the present analysis, the electron yield was integrated in the energy range where the electron yield for C^{4+} is greater than for C^{6+}, as seen in Fig. 1. The relative loss electron yield is defined by the integrated loss electron yield divided by the integrated C^{6+} yield. Fig. 3 shows the dependence of the relative loss electron yield for Si$\langle 110 \rangle$ on the incident ion energy. We see that the relative loss electron yield increases sharply at ∼3.5 MeV/u with increasing the ion energy. This value is in good agreement with the resonance energy of 3.44 MeV/u, corresponding to the 1s to 2p transition ($\Delta E = 277.4$ eV) of C^{4+} under the RCE condition for $d = 3.84$ Å (Si$\langle 110 \rangle$) and $N = 1$. The observed sharp increase of the loss electron yield is attributed to the enhanced ionization of the excited 2p electron, resulting from the decreased binding energy (283.8 down to 6.4 eV) and the widely spaced distribution of the 2p electron, compared with the 1s electron.

In further studies of RCE in a backward direction, planar, rather than axial, RCE would provide detailed resonance profiles. Planar RCE can be measured by tilting the crystal along a planer direction

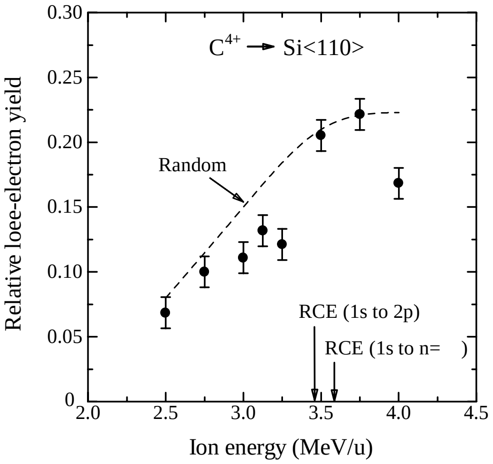

Figure 3: Dependence of the relative loss electron yield for Si⟨110⟩ on the ion energy.

of interest [1]. Angular dependence of the loss electron yield is typically easier to measure than the projectile-energy dependence obtained in the present experiments. Measurements of planar RCE by the present observation technique are now being planned to develop a new technical approach to RCE.

References

[1] H. F. Krause, S. Datz, Adv. At. Mol. Opt. Phys. 37 (1996) 139.

[2] K. Kimura, H. Ida, N. Fritz, M. Mannami, Phys. Rev. Lett. 76, (1996) 3850.

[3] C. Auth, H. Winter, Phys. Rev. A 62 (2000) 012903.

[4] H. Kudo, *Ion-Induced Electron Emission from Crystalline Solids*, ’Springer Tracts in Modern Physics, vol. 175’, Springer-Verlag, Berlin, Heidelberg, 2002.

[5] M. E. Rudd, Y. -K. Kim, D. H. Madison, T. J. Gay, Rev. Mod. Phys. 64 (1992) 441.

3.2 Electron emission from Si crystals bombarded by fast Ag ions

H. Kudo, M. Nagata, M. Suzuki, I. Arano, S. Numazawa, C. Sakurai, W. Iwazaki, T. Suguri, S. Seki[1]

When solids are bombarded by ions in the MeV/u energy range, most of the energetic electrons emitted from the surface are produced originally in the binary-encounter processes [1]. Studies of ion-induced electron emission under channeling incidence conditions of fast ions have so far been reported for ions of atomic numbers Z_1 up to 17 (^{35}Cl) [2, 3]. It is of fundamental interest to investigate whether the present understanding of the phenomenon still holds for projectile ions of much high Z_1 values. In response to the above question, the present experimental work provides data for high Z_1, using Ag ions ($Z_1 = 47$).

We have studied energy spectra of electrons emitted from Si and Ge single crystals bombarded by 1 MeV/u Ag ions under channeling and nonchanneling (random) incidence conditions. The electrons were measured at 180° with respect to the ion beam direction. Detection of electrons at 180° is advantageous for the purpose of avoiding errors associated with misalignment of the spectrometer.

The experimental conditions were similar to those reported elsewhere. Figure 1 shows energy spectra of secondary electrons emitted from Si and Ge bombarded by 1 MeV/u Ag^{10+} and Ag^{11+} under $\langle 110\rangle$ and random incidence conditions. In this case, the binary-encounter peak energy E_B is 2.18 keV. We see in Fig. 1 that the channeling yield differs remarkably from the random yield at electron energies higher than $E_\mathrm{B} = 2.18$ keV. This difference is due to shadowing of Si L-shell electrons, and of Ge M-shell electrons, as pointed out previously. Furthermore, there is no essential difference in the yiled for Ag^{10+} and Ag^{11+}.

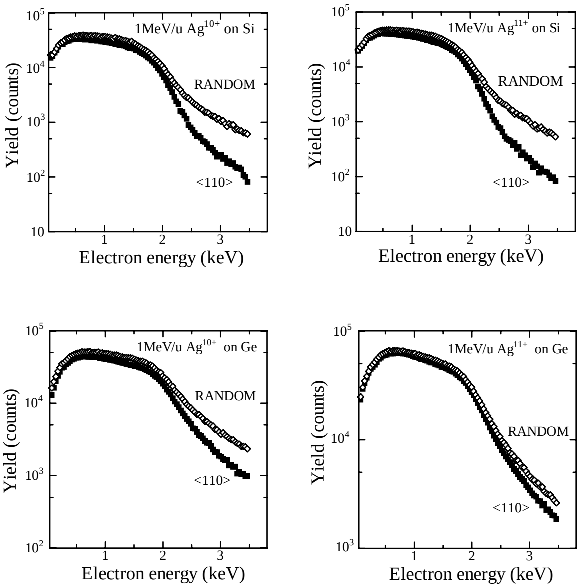

Figure 1: Energy spectra of secondary electrons emitted from Si and Ge bombarded by $\mathrm{Ag}^{10+,11+}$ under $\langle 110\rangle$ and random incidence conditions.

The ratios of $\langle 110\rangle$ to random yield, i.e., the normalized $\langle 110\rangle$ yields are shown in Fig. 2. We may compare the values of the Si$\langle 110\rangle$ normalized yield W_0 at an electron energy of $\sim (E_\mathrm{B} + E_\mathrm{L})/2$, with E_L being the loss-peak energy, with the previously measured values for the equal-velocity He^{2+}. The value of $W_0 = 0.78 \pm 0.04$ for Ag^{10+} and Ag^{11+} is greater than $W_0 = 0.59 \pm 0.02$ for He^{2+}, by a factor of 1.3. This difference is due the screened neclear charge of the Ag ions, since in this velocity range roughly 50% of the total electrons of Ag are in the bound state (charge state 25+) in solids [4]. Screening of the nuclear

---

[1] SSL Tsukuba

charge of the ion gives rise to the enhanced normalized yield by (i) the reduced shadowing effect, and (ii) the enhanced recoil effect, according to previous works [3].

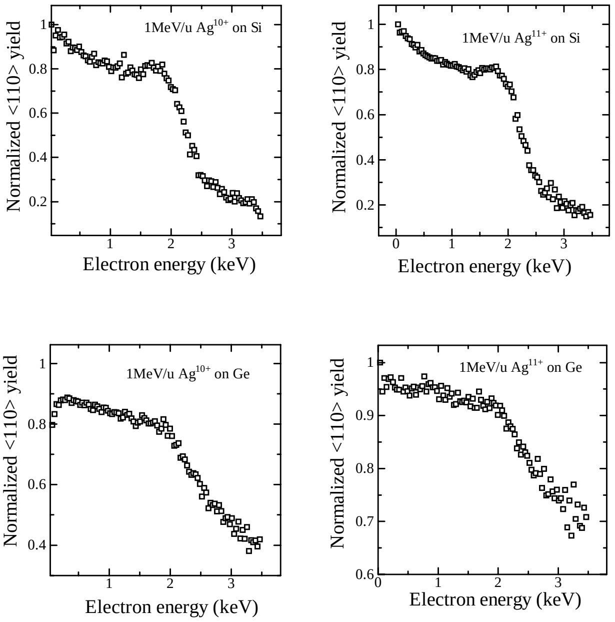

Figure 2: Normalized $\langle 110 \rangle$ electron yields for Si and Ge.

The experimental results are summarized as follows:

- The present work demonstrates that even for high-Z_1 projectiles, such as Ag, the energy spectra of ion-induced electrons emitted from crystals can be accounted for in terms of the high-energy shadowing effect on specific inner-shell electrons of the crystal atoms.
- For high-Z_1 ions, screening of the projectile nucleus by the bound electron(s) is a key factor for understanding the degraded shadowing effect compared with that for highly ionized ions.

References

[1] M. E. Rudd, Y. -K. Kim, D. H. Madison, T. J. Gay, Rev. Mod. Phys. 64 (1992) 441.

[2] H. Kudo, A. Tanabe, T. Ishihara, S. Seki, Y. Aoki, S. Yamamoto, P. Goppelt-Langer, H. Takeshita, and H. Naramoto, Nucl. Instr. and Meth. B 115 (1996) 125, and references therein.

[3] H. Kudo, *Ion-Induced Electron Emission from Crystalline Solids*, ’Springer Tracts in Modern Physics, vol. 175’, Springer-Verlag, Berlin, Heidelberg, 2002.

[4] K. Shima, N. Kuno, M. Yamanouchi, H. Tawara, At. Data Nucl. Data Tables 51 (1992) 173.

3.3 Anomalous elastic property of nanocrystalline gold

H. Tanimoto, Y. Koda, T. Yamada, S. Sakai, H. Mizubayashi,
Institute of Materials Science, University of Tsukuba

1. Introduction

When the ultrafine particles are mechanically consolidated, the disordered grain boundaries (GBs) can be formed to accommodate the neighboring ultrafine crystallites. Characteristic properties of the nanocrystalline (n-) metals prepared through such an athermal root may be associated with the disordered GBs as well as an increased volume fraction of the GB regions [1]. By the progress in thecnique, the n-metals with the density more than 98 % of the bulk density have been prepared. Surprisingly, the moduli measured for the pore- and contamination-free n-metals are found to be very close to those of the conventional polycrystalline (p-) metals, suggesting that the local density of the GB regions in the n-metals are not so different from the bulk density [2-4]. On the other hand, very recently, the interesting anelastic response is found for the high-density n-metals. For n-Au specimens prepared by the gas deposition method, the strong anelastic strain due to a certain GB process can be observed above 200 K [5]. In order to modify the GB state and to survey the change in the elastic property, anelastic measurement was conducted for the high-density n-Au irradiated by electron at low-temperature.

2. Experimental Procedure

The high-density n-Au specimen was prepared by the gas-deposition method [4]. The mean grain size and the density of the specimen used were about 20 - 25 nm and more than 99 % of the p-Au, respectively. The 20MeV proton irradiation was carried out by using the tandem accelerator of University of Tsukuba. The 2MeV electron irradiation was carried out at 10 K by using the 3MeV single-ended electrostatic accelerator of TIARA, JAERI. The anelastic measurement was performed by the flexural vibrating-reed method, where the resonant frequency, f, and internal friction, Q^{-1}, were measured by using the specially designed cryostat during and after irradiation.

3. Results and Discussion

Figure 1 shows the strain amplitude, ε, dependence (SAD) in the modulus observed for n-Au before and after 2MeV electron irradiation. It is noted that f^2 is proportional to Young's modulus, E. In the ε range in between 10^{-6} to 5×10^{-3}, E typically shows a decrease by about 1 % with increasing ε up to ~ 1×10^{-3}, and then turns to increase for ε above ~ 1×10^{-3} showing a saturation at ε ~ 5×10^{-3} (not shown here). It is noted that the internal friction, Q^{-1}, shows a slight increase for ε below ~ 1×10^{-3} and then a steep increase for ε above ~ 1×10^{-3}. No change was observed for these unique SAD of n-Au after 2MeV electron irradiation.

On the other hand, a large increase in f was found during the low-temperature irradiation. Figure 2 depicts the normalized change in f at 6 K observed during the irradiation, where the Frenkel-pair concentration was estimated from the electron dose. It is known that the modulus shows a slight decrease by the accumulation of the radiation defects (the bulk effect), and its rate per unit Frenkel-pair concentration is reported to be about -10 for the low-temperature electron irradiation of refractory BCC metals [6]. The increased *f* by the irradiation showed a recovery by about 50 % after warm-up to room temperature. The features observed for the anelastic measurements of n-Au were quite same between the 2MeV electron irradiation experiment and 20 MeV proton irradiation experiment.

These results indicate that the radiation defects would be trapped at the GBs in n-Au and modify their state as leading to the large increase in the modulus at 6 K. In contrast, the SAD of the modulus is independent on the radiation defects probably trapped at the GBs. We surmised that the SAD of the n-Au might reflect the characteristic of the crystallites in the n-Au rather than that of the GBs. A further study is now in progress.

References

[1] H. Gleiter, Prog. Mater. Sci. **33**(1989) 223.

[2] P. G. Sanders, J. A. Eastman and J. R. Weertman, Acta Mater. **45**(1997)4019 : P. G. Sanders, C. J. Youngdahl and J. R. Weertman, Mater. Sci. Eng. **A234-236**(1997)77.

[3] X. Y. Qin, X. R. Zhang, G. S. Cheng and L. D. Zhang, Nanostruct. Mater. **4**(1998)661.

[4] S. Sakai, H. Tanimoto and H. Mizubayashi, Acta Mater. **47**(1999)211.

[5] S. Sakai, H. Tanimoto and H. Mizubayashi, Scripta Mater., **45**(2001) 1313.

[6] H. Tanimoto, H. Mizubayashi, R. Masuda, S. Okuda, T. Iwata, H. Takeshita and H. Naramoto, phys. stat. sol. (a), **132**(1992)353.

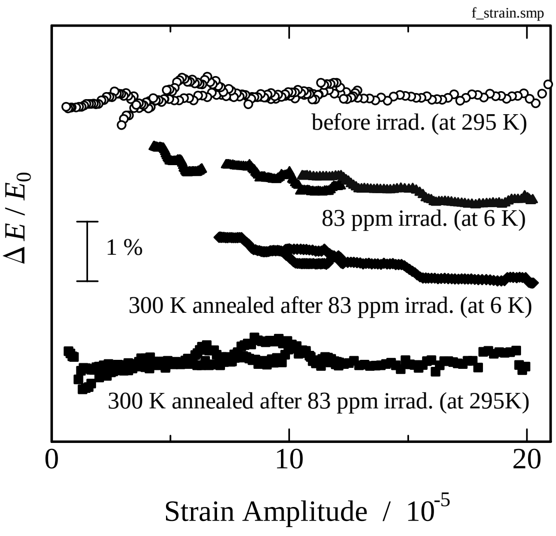

Figure 1. Strain amplitude dependence in the Young's modulus, *E*, observed for n-Au before and after electron irradiation. E_0 is the *E* observed at the smallest strain.

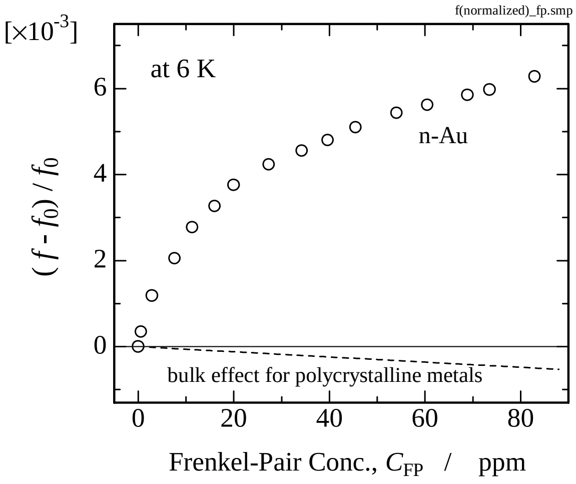

Figure 2. Change in the resonant frequency, *f*, observed during low-temperature 2MeV electron irradiation, where f^2 is proportional to E. For the comparison, the bulk effect observed for the polycrystalline metals is also shown.

3.4 Fabrication of microstructures in rutile TiO_2 single crystal using structural change induced by swift heavy-ion bombardment

M. Fujimaki[1], K. Awazu[1], N. Kobayashi[1], T. Nakanishi[2], K. Nomura[2], Y. Ohki[2], S. Ishii and K. Shima

It is known that a latent track, which is heavily damaged cylindrical zone, is made by the passage of swift heavy ions in many insulators. A visible hole is observed at the latent track by etching done after ion bombardment, because of an enhanced etching rate at the track [1]. Since this phenomenon has a possibility to fabricate micro- or nano-structures in an insulator, further investigation has been carried out.

Titanium dioxide (TiO_2) is a well-known insulator and is attracting much attention because it has many ways of applications in optics and electronics. For example, it is used as a catalyst, an optical prism, an isolator and as a photonic crystal. A photonic crystal, which has a spatially periodic permittivity modulation, realizes several valuable photonic devices such as a super-prism, a sharp-bend optical waveguide, and a high-*Q* cavity. Therefore, we used rutile TiO_2 single crystal as a sample and have tried to establish the methods of fabricating micro- or nano-stractures into the sample.

The rutile TiO_2 single crystals used have a purity higher than 99.99 %, density of 4.25 g/cm^3 and plane index of (100). They were synthesized by the Verneuil flame-fusion method and were supplied by Nakazumi Crystal Laboratory. They were cut into plates and epitaxially polished to a thickness around 500 μm. Their root-mean-squared roughness is less than 0.8 nm. Ion irradiation was carried out using a 12-MV tandem accelerator at the University of Tsukuba Tandem Accelerator Center (UTTAC), in a vacuum with a residual pressure below 1×10^{-3} Pa at room temperature. To survey the surface morphology and the structural changes after the ion bombardment, we used a scanning electron microscope (SEM, Hitachi S-2500CX), a high-resolution electron microscope (HREM, Hitachi H-9000NAR) and an X-ray diffractometer (Rigaku FR-MDG). A mask was put on the sample to restrict the irradiated area during the ion bombardment. The step height was measured between the irradiated area and the non-irradiated area with a DEKTAK II A profilometer, where the experimental error was ± 10 %. For etching, we used hydrofluoric acid.

We irradiated ions to the sample to a dose over 5.0×10^{13} cm^{-2}. The ions irradiated are 120-MeV I^{11+}, 40-MeV I^{7+}, 120-MeV Br^{11+}, 50-MeV Br^{7+}, 110-MeV Cu^{10+}, 84.5-MeV $Cu^{17.4+}$, 15-MeV $Cu^{10.6+}$, and 100-MeV Ti^{10+}. When the step height between the irradiated and non-irradiated areas was measured, an expansion was observed in the irradiated area for all the ions we used. Since the density of rutile phase is the largest among the crystal phases of TiO_2, it is considered that this expansion is caused by a structural change. Figure 1 (a) shows a SEM picture of the surface step between the irradiated area (lower right)

---

[1] National Institute of Advanced Industrial Science and Technology (AIST)
[2] Waseda University

and the non-irradiated area (upper left) after the surface was etched following the irradiation of 110-MeV Cu^{10+} ions to a dose of 8.0×10^{13} cm^{-2}. The irradiated area was etched to a depth of 8.1 μm, while non-irradiated area was not etched at all, regardless of the hydrofluoric acid concentration. The depth does not get deeper even when the etching time or dose increases. This tendency was seen for all the ions examined. It should be also noted that the etched surface is very flat and the roughness of the boundary wall, which was formed by etching, is very small as shown in Fig. 1 (a). Figures 1 (b) and (c) are the SEM pictures of the surface which was etched after it had been irradiated by 110-MeV Cu^{10+} ions to a dose of 8.0×10^{13} cm^{-2} through a 13-μm thick gold mesh. The mask shapes were properly transcribed on the rutile TiO_2 single crystal. By using this technique we can fabricate micro- or nano-structures in dielectric materials such as a rutile TiO_2 single crystal.

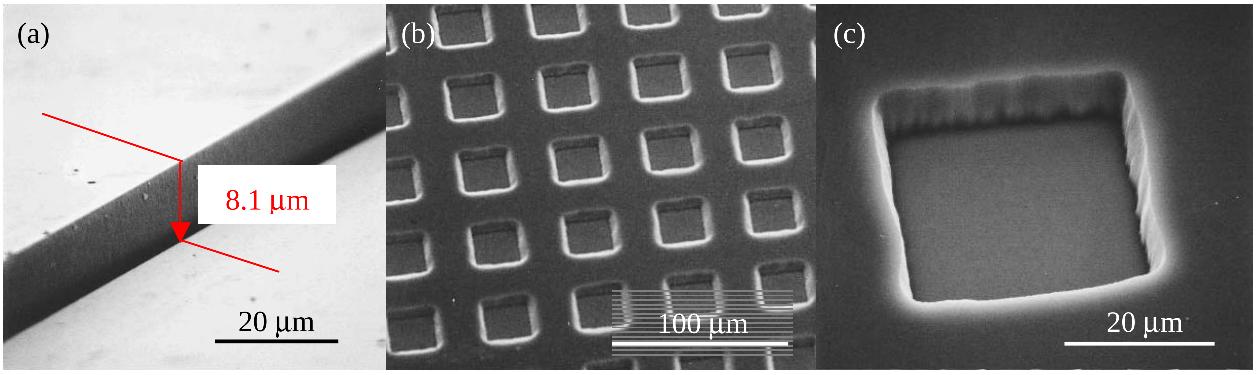

Fig. 1. SEM pictures of the TiO_2 surface etched by 20 % hydrofluoric acid for 30 min. Irradiation with 110-MeV Cu^{10+} ions to a dose of 8.0×10^{13} cm^{-2} had been done on the sample prior to the etching through a 1-mm thick silicon plate masking the upper left area during the irradiation (a) or through a 13-μm thick gold mask [(b) and (c)].

References

[1] K. Awazu, S. Ishii, K. Shima, S. Roorda and J. L. Brebner, Phys. Rev. B **62**, 3689 (2000).

3.5 Measurement of retained deuterium density in metals after deuteron implantation

N. Kawachi, N. Yoshimaru and Y. Tagishi

We have developed a new method of measurements of implanted deuterium atoms by observing emitted protons from the nuclear reaction $^{2}H(d,p)^{3}H$ between implanted deuterium atoms and incident deuterons [1]. A drastic difference in the time dependence of the proton yield was observed between single and polycrystalline targets [1]. We made measurements to estimate the density of deuterium atoms after deuteron implantation. It is difficult to obtain the density of deuterium atoms near the mean penetration with the method described in the paper [2], because the cross section of the reaction $^{2}H(d,p)^{3}H$ near the range is too small for calculating correctly the concentration of deuterium atoms.

Experiments were performed with the same experimental setup as described in [2] using two deuteron beams with energies of 100 keV and 50 keV at UTTAC. Samples for the implantation were single and polycrystalline targets of tantalum, palladium and copper. A method for estimating the distribution consists of the following three steps.

Step 1. *(deuteron implantation at 50 keV)*: A target was prepared by deuteron implantation at an energy of 50 keV in an area of 3 mm in diameter. The implantation flux was approximately 2×10^{13} D/cm^{2}·s. Approximately 6×10^{17} D/cm^{2} deuterons were implanted in the target material.

Step 2. *(irradiation of analyzing beam at 100 keV)*: After the implantation, a deuteron beam with a higher energy of 100 keV was delivered to the target material. A slit of 1 mm in diameter was placed to define a smaller irradiation area in the center of the implanted area in step 1. In order to switch the deuteron beam energy from 50 keV for implantation to 100 keV for analysis, the irradiation was interrupted for a short time (~ 400 s). The dose delivered by the analyzing beam was 6×10^{15} D/cm^{2}, which was large enough to obtain an adequate number of emitted protons for analysis of implanted deuterium atoms.

Step 3. *(evaluation of deuterium atoms implanted at 100 keV)*: The protons detected in Step 2 includes not only protons which were emitted from the $^{2}H(d,p)^{3}H$ reaction with deuterium atoms implanted in Step 1 at 50 keV, but also from protons caused by implanted deuterium atoms during Step 2 at 100 keV. To subtract the proton yield from the irradiation at 100 keV, the same dose of 6×10^{15} D/cm^{2} was irradiated on the same size as the virgin material. The energy spectrum of the emitted protons from this area was subtracted from the spectrum obtained in Step 2. The distribution of deuterium atoms implanted at 50 keV was derived with this substraction.

The number of emitted protons in Table 1 is proportional to trapped and retained deuterium atoms in target metals. This result supports the reported data in [1], where a large difference of emitted proton yields between single and polycrystalline Ta and Pd target is obtained and no difference in case of those in Cu. It is clear that the number of retained deuterium atoms appears to the time dependence of the proton yields and there are little deuterium atoms trapped in single crystal Ta.

Deuterium atoms are possible to solute into both Ta and Pd single and polycrystalline metals because of its minus enthalpy. The accumulating deuterium atoms should be sensitive to the number of deuterium trapping with impurities. It is difficult to discuss to what extent the difference of the time dependence of the proton yield is caused by deuterium atoms trapped with impurities in metals. Only a difference of tantalum single crystal impurities between <100> and <111> could be checked with catalog data. It considered being due to appear the difference of the retained deuterium atoms in the <100> and the <111> Ta single crystal. Copper has plus enthalpy to hydrogen solution at infinite dilution, so that the implanted deuterium atoms cannot exist stably. However, radiation damage should be produced at near surface region in case of both single and polycrystalline target. The damage might play some role on similar yield curves of emitted protons, which indicates the same concentration of deuterium atoms in single and polycrystalline Cu.

References

[1] N. Kawachi et al. UTTAC annual report **69**(2000)59

[2] N. Kawachi, T. Katabuchi, et al. Nucl. Instrum. Methods Phys. Res. B **190**(2002)195

	Poly-crystal	Single crystal	
Tantalum	13296 (count)	<100> <111>	335 308
Palladium	6357	3725	
Copper	15789	14441	

Table 1 The number of emitted protons from the implanted targets with 50 keV deuterons, using a probe beam of 100 keV deuterons. This number indicates the trapped and retained deuterium atoms in the target metals.

3.6 TOF spectra of dissociated molecules by photon/HCI impact in crossed-beam apparatus for cluster fission experiment

H. Sasaki, Y. Takanashi, M. Imanaka, I. Arai and S. M. Lee

We have developed a TOF mass spectrometer system to measure the mass to charge ratio of the products generated by collision between a highly charged ion(HCI) and a neutral molecule or cluster. In this report, we introduce this system and show preliminary spectra of collision products observed with benzene target irradiated by laser and HCI.

A schematic view of the system is illustrated in Fig. 1. The HCI beam is provided from an electron cyclotron resonance ion source[1] and separated according to mass to charge ratio by the 90 degree analyzer magnet. We used a Xe^{20+} beam extracted by a voltage of 15 kV the current of which was 1 μA. The charge selected beam is chopped into a pulsed beam with a time duration of 200 ns long by a pulsing electric field generated by the deflecting electrode. To make a pulsed high voltage swing from 0 V to 2.8 kV on the electrode, we use a high speed push-pull switch(Bhelke Electronic, HTS31-GSM). The pulsed ion beam passes through the diaphragm of ϕ1 mm and intersects the target chamber. The base pressure of the target chamber is 10^{-8} torr. We put the benzene vapor into the target chamber up to the pressure of 1.0×10^{-6} torr. The extraction region consists of an ionization region and acceleration region. After a HCI beam has passed the ionization region, an extraction field can be pulsed with a high speed push-pull switch and the ions of collision products enter the acceleration region. In the acceleration region there are applied two electric field with different gradients from each other. The two stage extraction can focus the flight time of the ion which was produced with the same m/q but at the different position in the ionization region. An acceleration voltage of 2700 V is applied in a region of 5 cm in length giving a field gradient of 107 V/cm for the first acceleration region, while the same voltage is applied in a region of 4 cm giving a field gradient of 525 V/cm for the second acceleration. The intermediate electrodes (1 cm apart from each other) in the acceleration region ensure a good homogeneity of electric field necessary for a high mass resolution. The path of the ions is corrected by the electrostatic steerer and focused by the Einzel lens. The ions fly in the field free region of 2 m and finally go into the detector. We used a micro channel plate detector with a cup-type electron conversion dynode. We measured TOF spectra by using a trigger signal of the extraction pulse switch as a start signal and an output signal of the detector as a stop signal, both of which were lead to a 2 GHz multi-stop time to digital converter(P7886E, FAST ComTec).

Fig. 2 shows the result obtained in collision with highly charged Xe^{20+} ions. There are the clearly identified peaks of benzene +1, +2, +3 in addition to those of residual gas ions. This fact seems to suggest that benzene is produced in highly charged states with relatively low internal energies. In Fig. 3 is shown the spectrum, where benzene have been irradiated by a YAG laser(4th harmonics, photon energy:4.67 eV). The mass resolution estimated from a peak of benzene +1 is about 1000. It is found that only singly charged ions are produced. The series of dominated peaks for $\mathrm{C}_n\mathrm{H}_m^+$ ions is thought to be caused in the course of evaporation process of parent hydro-carbons with an increased internal temperature.

Now, we are planning to produce a highly charged cold metal cluster and measure its appearance size and fission pattern[2].

References

[1] T. Kurita, Doctor thesis, University of Tsukuba(2001).

[2] F. Chandezon, S. Tomita, D. Cormier, P. Gübling, C. Guet, H. Leibius, A. Pesnelle and B. A. Huber, Phys. Rev. Lett. **87**, 153402(2001).

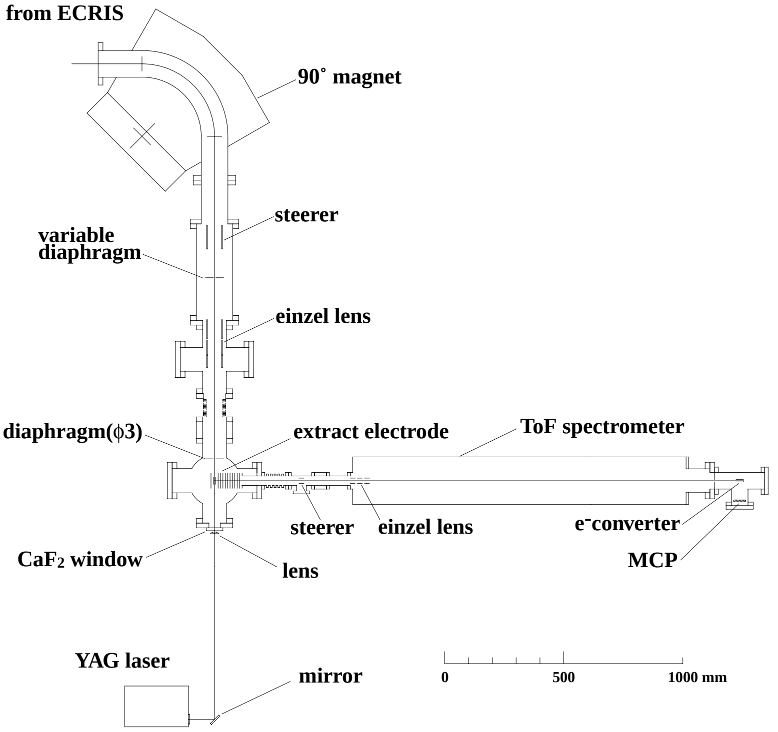

Fig. 1: Top view of beam line and TOF system

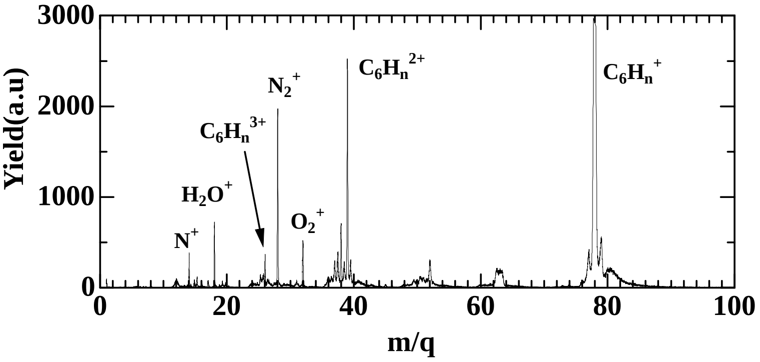

Fig. 2: Mass/Charge distribution of collision products observed with benzene molecule irradiated by Xe^{20+}.

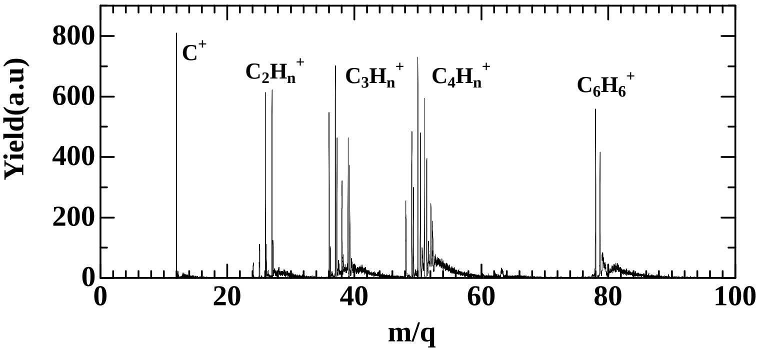

Fig. 3: Mass distribution of benzene molecule and its fragment irradiated by a YAG laser. The fluence of laser pulse is 4 mJ/pulse, its pulse width is 4 ns and its spot size is below 1 mm.

3.7 Cluster abundance spectra of low melting temperature metals produced by bombardment of 6keV Xe atoms

T. Miyazaki, K. Teranishi, H. Sasaki, I. Arai and S.M. Lee

In the previous experiments on sputtering of high melting temperature transition metals with 6keV Xe atoms, we observed that cluster abundance spectra for such metals typically show a power law nature. We successfully described the observed regularities shown via such a power law nature in the cluster abundance spectra with use of a model based on the following assumptions; (1)thermal diffusion along the surface, (2)associated formation of thermally isolated area, the equilibrium temperature being kept much higher than the melting temperature at around the bombardment position, and (3)cluster formation within the thermally isolated area as a result of bond-breaking. Furthermore, a strong correlation between the broken bond probability p, i. e., an only parameter in the model calculation, and the melting temperature for each metal was also reproduced well. However, it was found that the model is not applicable in cases of the metals such as Zn and Mn. The cluster abundance spectra for those metals were expressed by exponential functions quite well. So far, an exponential function-like spectrum was thought to be characteristic in the early stage of gaseous aggregation process. Therefore, it is suggested that a huge number of monomer atoms are released by a certain kind of explosion on the surface [1][2][3].

In the present experiment, we have carried out the same measurements for the low melting temperature metals In, Ga, Sn and Bi and discovered other types of cluster abundance spectra than the previously observed ones. One is expressed by a combination of an exponential function and a power function in the case of In and Ga(see Figure 1), and the other by a combination of an exponential function and a log-normal function in the case of Sn and Bi(see Figure 2).

In the former case, it is expected that an explosive release of monomer atoms occurs just after the bombardment and the cluster formation proceeds via monomer absorption at some later stage. More than 90 % of secondary cations seems to originate in this process and most of thermal energy given by the bombardment of Xe atom is released as well. The exponent of power function is found to be -1.5, which should be compared with the value of -2.7 in the case of high melting temperature metal such as Cu. In other words, larger-sized clusters are produced in this case than in the case of Cu. A possible scenario is as follows;(1)an explosive monomer production takes place at first and (2)a cluster formation via bond-breaking happens on the remnant surface in succession. The temperature of remnant surface should become lower than the one in the case without such an explosive monomer production. The considerable energy is released prior to a thermal equilibrium. As a result, the broken bond probability p becomes small comparatively.

In the latter case, the observation of spectra following to log-normal functions is substantially new. Such spectra is rather common to a cluster formation via cluster coalescence under the course of aggregation process in high density gaseous environment, which is unlikely to occur in a singly driven short time phenomenon such as sputtering. If the underlying process is similar to an aggregation process, the present observation suggests a explosive release of monomer atoms with a high density core.

Figure 3 shows a correlation between a melting temperature and a variable corresponding to a evaporative latent heat, i.e., a first order coefficient in the $\frac{1}{T}$ expansion of saturated vapor pressure. The cluster abundance spectra for the materials with higher melting temperature seem to be expressed by a power function, while those for the materials with smaller evaporative latent heat by an exponential function. In the lower melting temperature region, those for the materials with larger evaporative latent heat show an intermediate nature, i.e. a combination of an exponential function and some other function, i.e., a power function or a log-normal function.

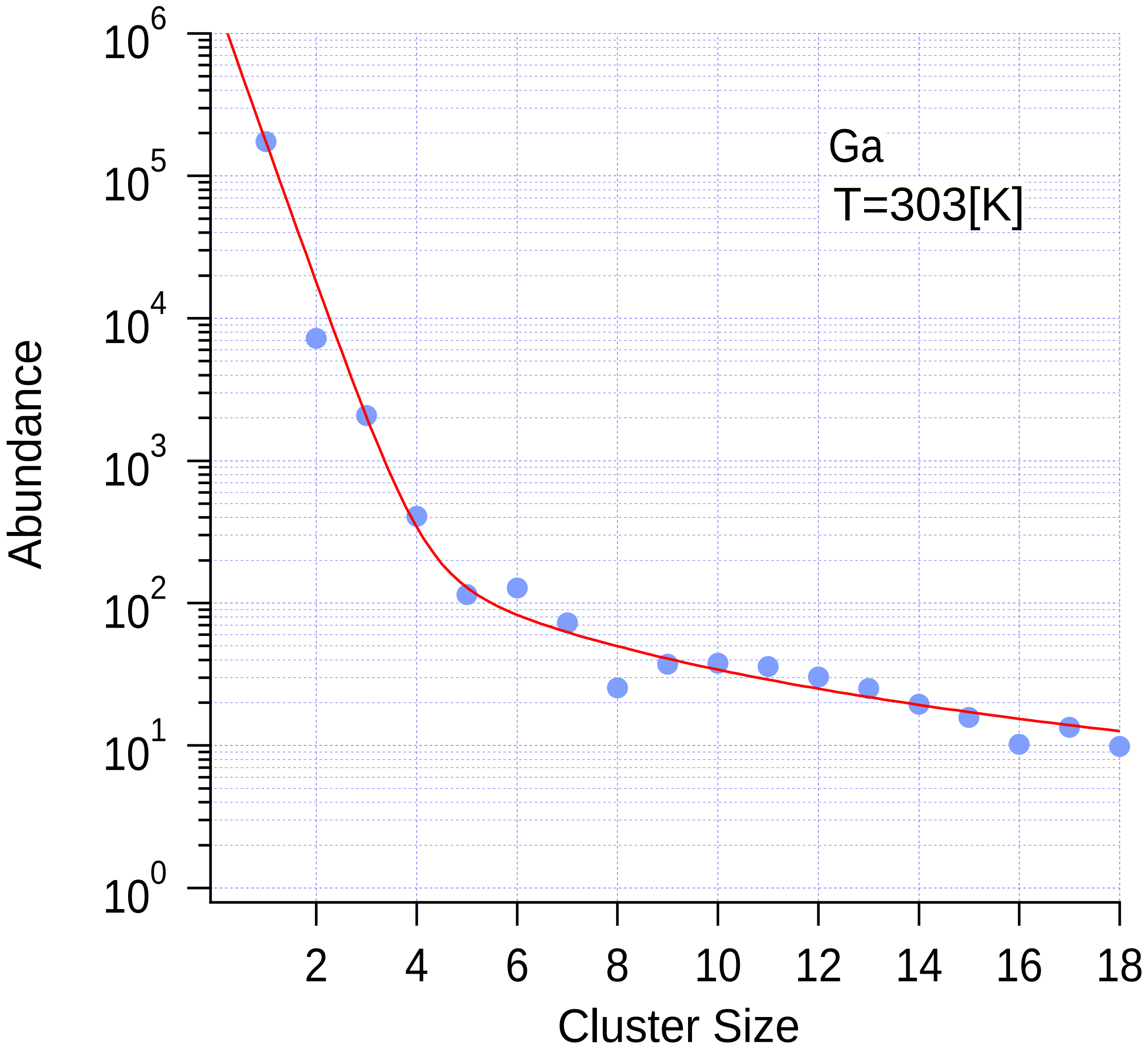

Fig. 1. Abundance spectrum of Ga clusters produced by bombardment of 6keV Xe atoms, which is represented by a combination of an exponential function and a power function(solid line).

References

[1] I. Arai, Desorption 2000 Int. Conf., Saint Malo, France, 3-7(2000), invited talk.

[2] I. Arai et al., Trans. Material Research Society of Japan, **26**, (2001) 1139.

[3] I. Arai et al., Trans. Material Research Society of Japan, **27**, (2002) 193.

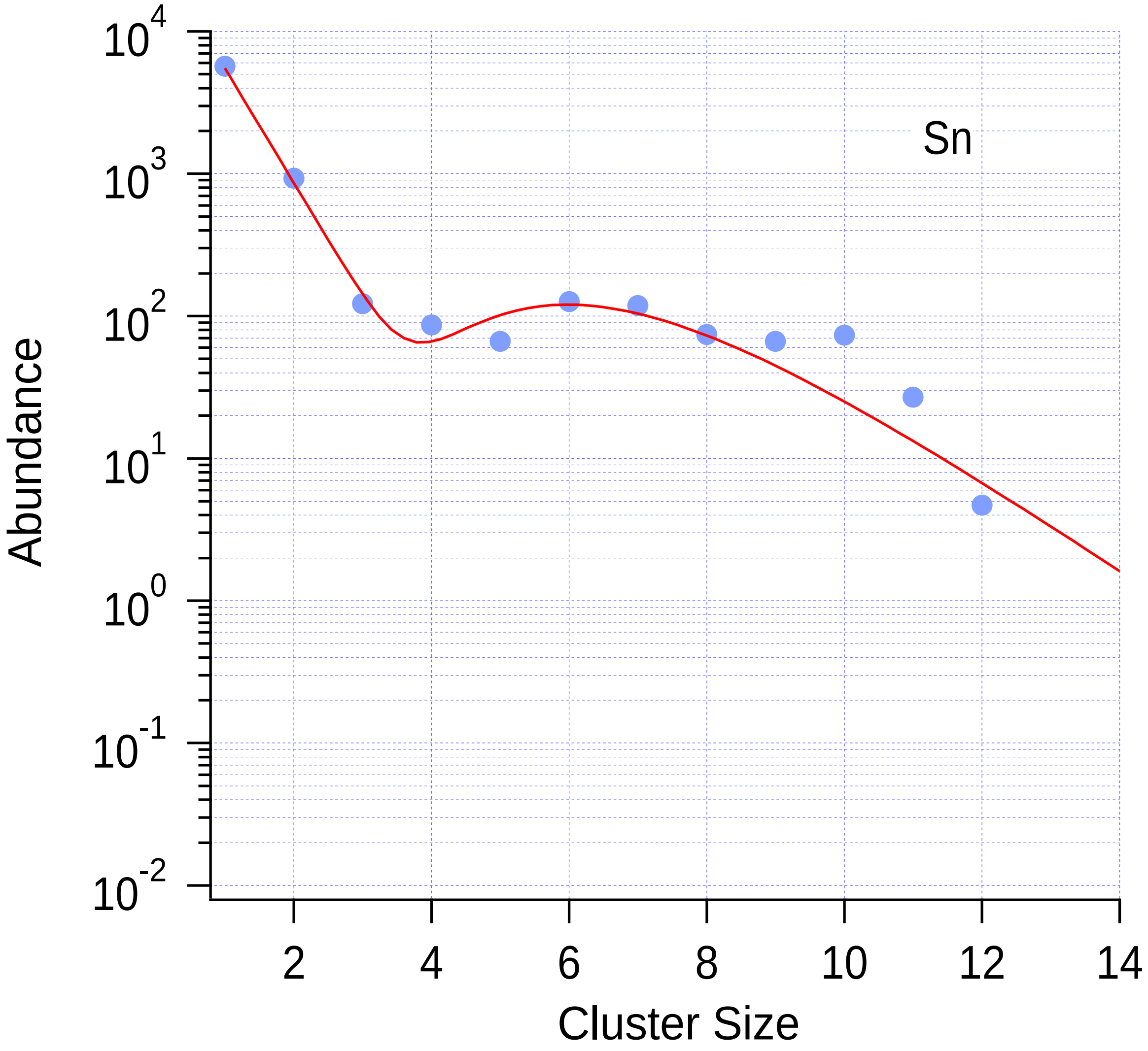

Fig. 2. Abundance spectrum of Sn clusters produced by bombardment of 6keV Xe atoms, which is represented by a combination of an exponential function and a log-normal function(solid line).

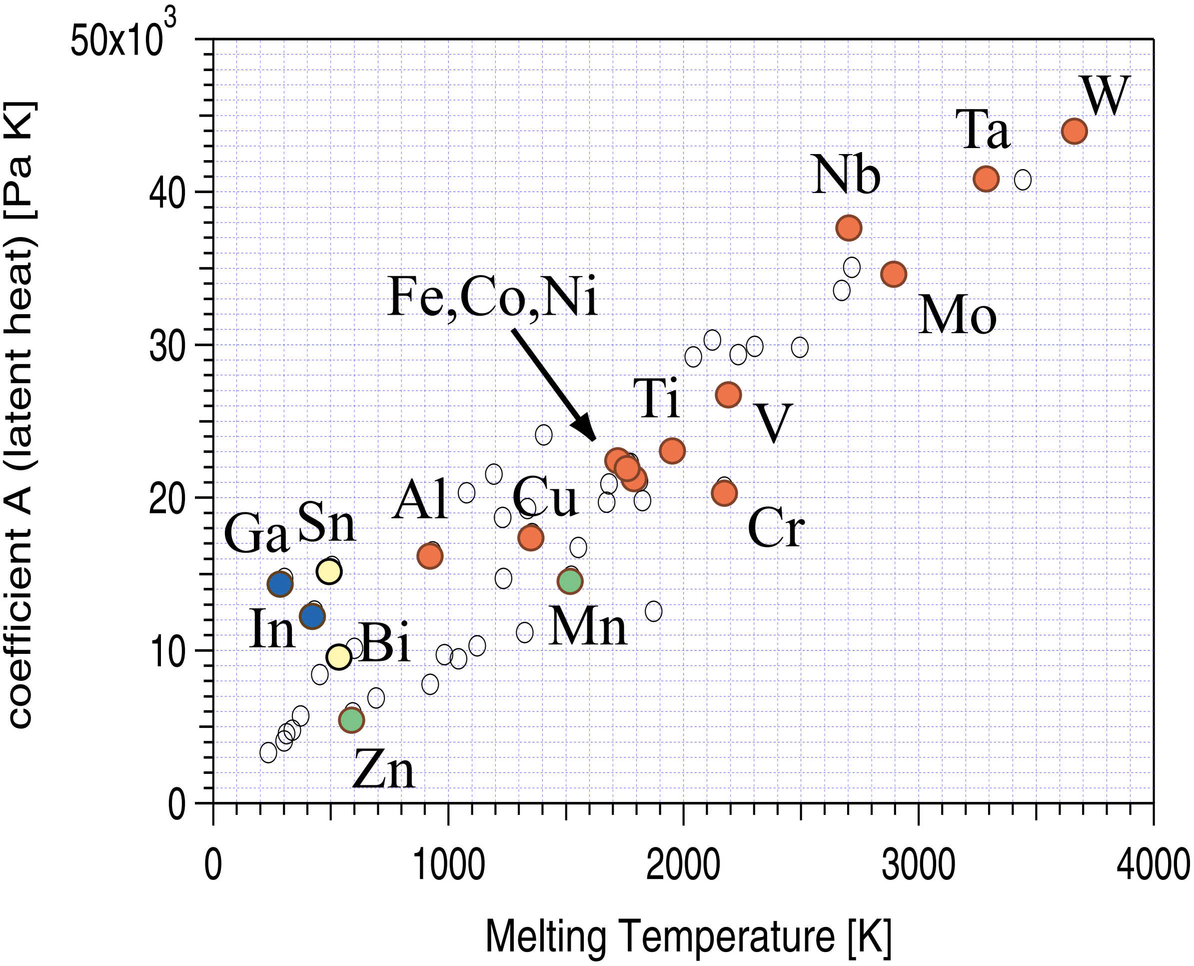

Fig. 3. Correlation between a melting temperature and a variable corresponding to an evaporative latent heat for each element, the spectrum of which is expressed by (1)power function(circles), (2)exponential function(triangles), (3)combination of an exponential function and a power function(diamonds) and (4) combination of an exponential function and a log-normal function (squares).

3.8 Simulations on gold and copper clusters

T.X.Li, I.Arai and S.M.Lee

The knowledge of structural and thermodynamic properties of finite atomic system is essential to the application of clusters and cluster-assembled materials. By using molecular dynamic simulation,we studied the solid-solid transitions and coalescence of gold and copper clusters.

Dynamic simulations on Au_{55} reveal the solid-solid structural transitions among different symmetric configurations, from cube-octahedron to icosahedron and disordered structure, at certain temperatures below the melting point. The latter deformation had not been demonstrated in earlier simulations on small clusters. However, Krakow and his colleagues found in their HRTEM(high resolution transmission electron microscope) study that supported gold clusters less than 10A* in size of ten appear to be disordered[1] .The solid-solid transformations are microscopically demonstrated as processes of collective distortion of atoms and migration of partial atoms. In both cases the cohesive energies of the system go smoothly without any significant barrier during transitions. This result has been sent to some journal for publication.

Multiply twinned particles(MTP) are frequently observed under HRTEM for metal nanoparticles[2]. Our simulation on Cu clusters shows this may because of the thermal stimulation in acouple of sticked clusters.

We use a Gupta-type many body potential to describe the interaction among the atoms. As a function of interatomic distance r_{ij}, the potential is expressed as

$$V = \sum_{j=1}^{n} \left[A \sum_{i(\neq j)=1}^{n} \exp[-p(r_{ij}/r_{0n} - 1)] - \left(\xi^2 \sum_{i(\neq j)=1}^{n} \exp[-2q(r_{ij}/r_{0n} - 1)] \right)^{1/2} \right]$$

In present work, the parameters for Cu are set as A=0.0855, ξ =1.224, p=10.96 and q=2.278, which have been fitted for bulk copper[3]. Two clusters, Cu_{38} and Cu_{75} initially have truncated-octahedron and quasi-crystalline as their most stable structure respectively, are approached to each other and heated up step by step. The structure of sticked large cluster is recorded after along term relaxation in each step.

Fig.1 shows the structural evolution of Cu_{38+75} with increasing temperature. The original shape and struture of both parts are kept very well when they touch each other with zero kinetic energy(Fig.1a). However, as light warming up to 160K causes much compact connection though the internal structure of each part remains unchanged ;and besides, the direction of each crystal has been adjusted to get mached at the interface(Fig.1b). When the temperature is increased to an even higher degree(602K), the two small clusters are reconstructed, as one cansee from Fig.1c, into a multiply twinned particle.The final configuration in our simulation is quite consistent to the experimental observation of gold cluster(2nm) irradiated by electron[2].

References

[1] W.Krakow et al.,Phys. Rev. B49, 10591(1994).

[2] S.Iijima and T.Ichihashi,Phys. Rev. Lett. 56,616(1986).

[3] F.Cleri and V.Rosato,Phys. Rev. B48, 22(1993).

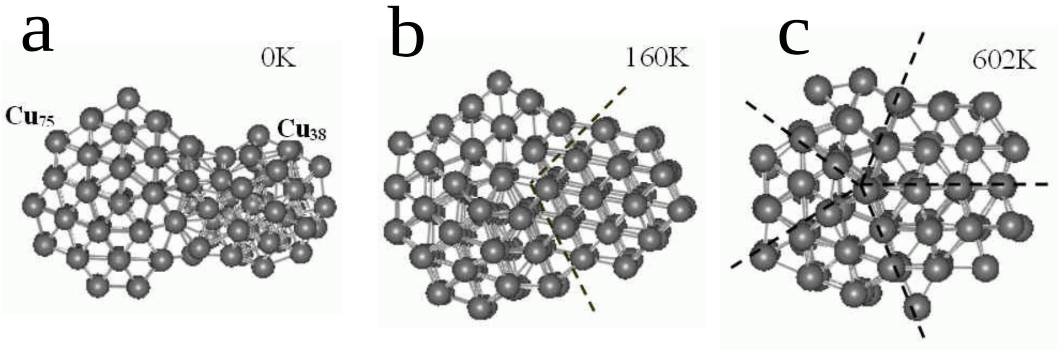

Fig. 1. The structures of two copper clusters (N=38 and 75) after attaching each other and being heated up to a)0K, b)160K and c)602K, respectively.

3.9 Mössbauer Study of α''-$Fe_{16}N_2$ foils prepared by a nitrogen plasma irradiation method

H.Tokano, K.Niizuma[*], Y.Utushikawa[*], K.Yano[*] and E.Kita

In 1972, Kim and Takahashi of Tohoku University reported the synthesis of a polycrystalline film composed of two phases of α-Fe and α''-$Fe_{16}N_2$ by using vacuum deposition. From the volume fraction, they estimated the saturation magnetization of α''-$Fe_{16}N_2$ to be 2200 emu/cc, which largely exceeds the value of Slater-Polling curve[1]. After their announcement, there have been a lot of works to synthesize the α''-$Fe_{16}N_2$ by various methods. However, the reported values of the saturation magnetization are different depending on the researchers and fabrication methods and, hence, the exact value of the saturation magnetization of α''-$Fe_{16}N_2$ phase still remains uncertain. Such uncertainty is caused by the difficulty of forming a large quantity of bulk samples due to the fact that the α''-$Fe_{16}N_2$ phase exists only in non-equilibrium state. Therefore, in the present work, we attempted to form bulk samples of α''-$Fe_{16}N_2$ by nitrogen plasma irradiating method. The analysis by Mössbauer spectroscopy was carried out for the obtained samples in order to discuss the volume fraction and hyper fine field.

Iron nitride foils were prepared by a plasma irradiation method in the atmosphere of N_2+30%H_2 mixture gases using polycrystalline iron foils as raw material. The samples were quenched using liquid nitrogen in order to have transformation to α''-$Fe_{16}N_2$. Mössbauer spectra were taken with a constant acceleration spectrometer at room temperature. The least squares fit of the spectra were carried out assuming Lorentzian line shapes.

Table 1 Mössbauer parameters of Fe-N foils

Sample	site	H_{hf} (kOe)	I.S. (mm/s)	Area (%)	H_{hf}^{ave} (kOe)	Ms(VSM) (emu/g)	Ms(cal.) (emu/g)
no quenched	α-Fe	330	0.0046	52.0	204	139	135
	FeI*	293	-0.0682	4.0			
	FeII*	-	-	-			
	FeIII*	369	0.0165	5.6			
	Singlet	-	0.0315	38.4			
before annealed	α-Fe	332	0.0070	60.5	290	187	190
	FeI*	291	-0.0745	4.3	324		
	FeII*	312	0.1309	15.9			
	FeIII*	369	0.0493	7.4			
	Singlet	-	-0.0504	11.9			
after annealed	α-Fe	330	0.0062	59.6	296	184	186
	FeI**	289	0.0785	11.1	330		
	FeII**	317	0.2193	10.6			
	FeIII**	400	0.1614	10.1			
	Singlet	-	-0.0551	10.1			

*Fe sites of the α'-martensite phase.

**Fe sites of the α''-$Fe_{16}N_2$ phase.

---

[*] Nihon University

Table 1 shows fitting parameters and Figs 1 and 2 show Mössbauer spectra, respectively. The sample without quenching has a strong paramagnetic subspectrum. Therefore, the subspectrum from α’-nitrogen martensite, which are originally composed of those from three sites, can be divided only two spectra in the figure. However, the quenched sample has a weaker paramagnetic spectra and, hence, the spectrum from α’-nitrogen martensite can be clearly divided three subspectra corresponding to three sites.

After annealed, the spectraum become sharper and the subspectrum from α’’-$Fe_{16}N_2$ can be distinctly divided to three sites spectra. The volume fraction of α’’-$Fe_{16}N_2$ estimated from the spectrum area ratio is about 30%. The result of fitting gave hyper fine fields of α’-nitrogen martensite are 291kOe, 312kOe and 369Oke for FeI, FeII and FeIII sites, respectively. The average value of hyper fine field, H_{hf}^{ave}, is 324Oke, which is slightly smaller than that of α-Fe. The values of internal field of α’’-$Fe_{16}N_2$ are 289kOe, 317KOe and 400kOe for FeI, FeII and FeIII sites, and H_{hf}^{ave} becomes 330kOe which is almost equivalent to that of α-Fe. Obtained results show a similar tendency with those of Takahashi and Shoji[2] and are different from the giant magnetic moment claimed by Sugita *et al*[3]. The saturation magnetization, Ms(cal.) was calculated by the assumption that the hyper fine field is proportional to magnetic moment and the hyper fine field of 33.0T corresponds to 218emu/g for α-Fe. The Ms(cal.) values of all samples are in good agreement with those actually measured by VSM. From these results, we conclude that the saturation magnetization of α’-nitrogen martensite synthesized by our method is almost same with that of α-Fe. It is also found that the saturation magnetization of α’’-$Fe_{16}N_2$ is slight larger than that of α’-nitrogen martensite, however, it still remains almost same level with that of α-Fe.

References

[1] T.K.Kim and M.Takahashi, Appl.Phys.Lett.,20,492(1972).
[2] M.Takahashi and H.Shoji, J.Magn.Magn.Mater.,208,145(2000).
[3] Y.Sugita,H.Takahashi,M.Komuro,K.Mituoka and A.Sakuma, J.Appl.Phys.,76,6637(1994).

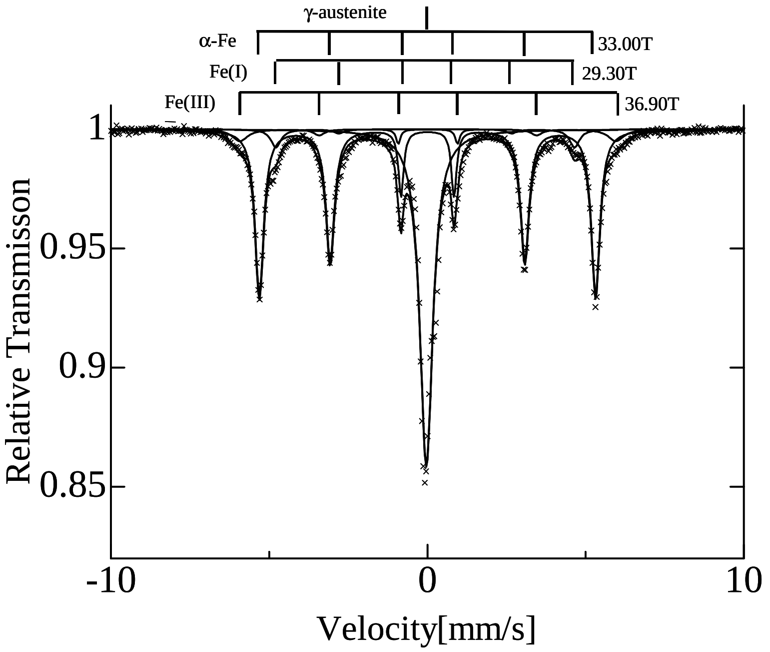

Fig.1 Mössbauer spectrum of an Fe-N foil no quenched.

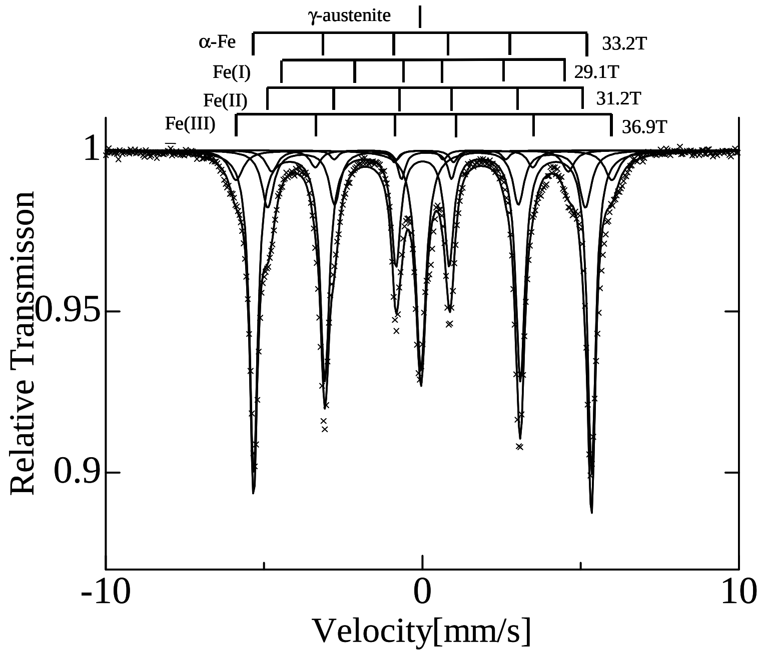

Fig.2 Mössbauer spectrum of an Fe-N foil before annealed.

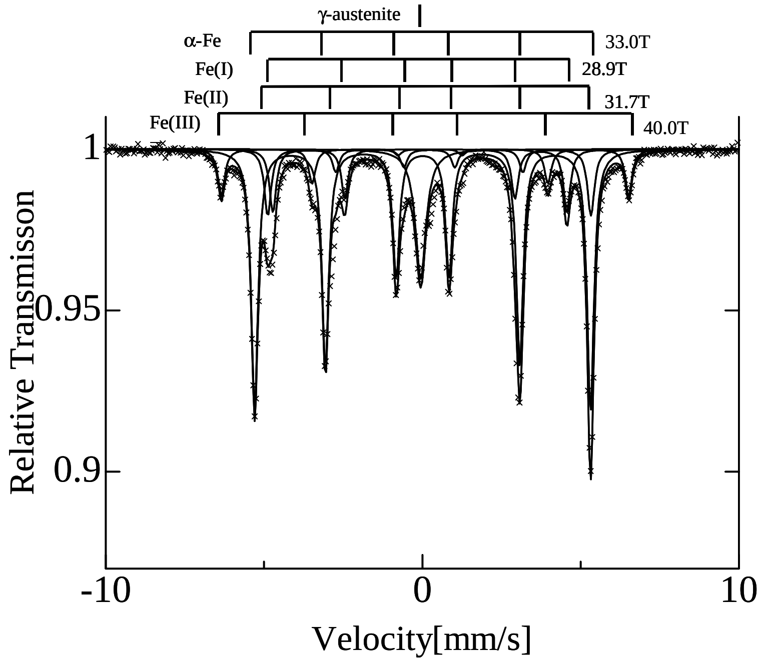

Fig.3 Mössbauer spectrum of an Fe-N foil after annealed.

3.10 Mössbauer study of superconducting $YFeSr_2Cu_2O_{6+\delta}$ compounds

Y. Hata[1], Y. Mihara, T. Mochiku[2] ,J.Suzuki[1], I. Kakeya, K. Kadowaki and Eiji Kita

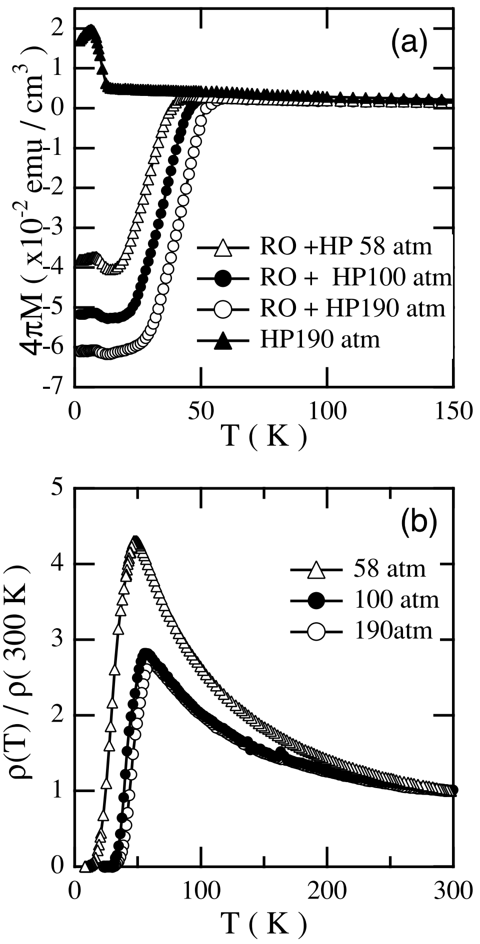

Fig. 1. (a) The temperature dependence of the magnetization of $YSr_2FeCu_2O_{6+y}$(sample 3-5) under magnetic field of 1 Oe. (Field cooled curves), (b)The electrical resistivity data for a $YSr_2FeCu_2O_{6+y}$ compounds. (sample 3-5) These data are normlized with their resistivity at 300 K.

Superconductivity and magnetism are two different ordered states into which substances can condense at low temperatures and in general these state are inimical to one another.Especially ferromagnetism interfere severely with occurrence of superconductivity. Recently, $RESr_2RuCu_2O_8$ (RE = rare earth element) system has been the focus of considerable work because of their interesting magnetic and superconducting properties.[1, 2] In the case of $GdSr_2RuCu_2O_8$, it shows a ferromagnetic transition at 132 K and bulk superconductivity sets in below T_c = 15 - 45 K, depending on the sample preparations and it was believed that ferromagnetism coexists with superconductivity in this compounds.

Comparison with these study, the substitution for Cu site of $YSr_2Cu_3O_{6+y}$ by Fe ion is interesting, however it was reported that they show poor superconductivity with a small Meissner volume fraction and relatively low transition temperature. [3, 4, 5] The distribution of Fe ion at Cu(2) site may suppress the superconductivity and it have been believed that it is impossible to synthesize superconducting $YSr_2FeCu_2O_{6+y}$ compound.

In this report we explore the possibility of synthesizing superconducting $YSr_2FeCu_2O_{6+y}$ by reoxidization annealing and high pressure O_2 annealing technique. ^{57}Fe Mössbauer spectroscopy is used to investigate the distribution and magnetism of Fe ions. $YSr_2FeCu_2O_{6+y}$ samples were prepared by the solid-state reaction of stoichiometric mixture of Y_2O_3, $SrCO_3$, CuO, and Fe_2O_3 powders. The mixture was calcined at 900°C for 24 h in air, ground, and then pressed into pellets. The pellets were sintered at 1000°C for 24 h in air. Then the pellets were subsequently annealed at 800°C for 24 h in N_2 flow, at 300°C for 24 h in O_2 flow, and finally at 350°C for 24 h in high O_2 pressure of 58 ,100, and 190 atm. We call the subsequent annealing in N_2 flow and O_2 flow "reoxidization annealing". Some of as synthesized pellets were directly annealed at 350°C for 24 h in O_2 pressure of 190 atm without reoxidization annealing.

Fig. 1(a) shows field-cooled magnetization of the superconducting samples obtained at the magnetic field of 1 Oe. Superconductivity was observed only in the reoxidized and subsequent high pressure O_2 annealed samples. Temperature dependences of resistivity for superconducting samples are shown in Fig. 1(b). The resistivities are normalized with the values at 300 K of 3.80×10^{-2}, 7.91×10^{-3}, and

---

[1] Advanced Science Research Center, Japan Atomic Energy Institute

[2] Superconducting Materials Center, National Institute for Materials Science

2.15×10^{-2} Ωcm, for sample 3, 4, and 5 , respectively. Superconductivity was confirmed in resistivity. Increasing O_2 annealing pressure, the onset transition temperature of superconductivity increases linearly and approches to 60 K. Semiconducting temperature dependences are observed above the transition temperature.

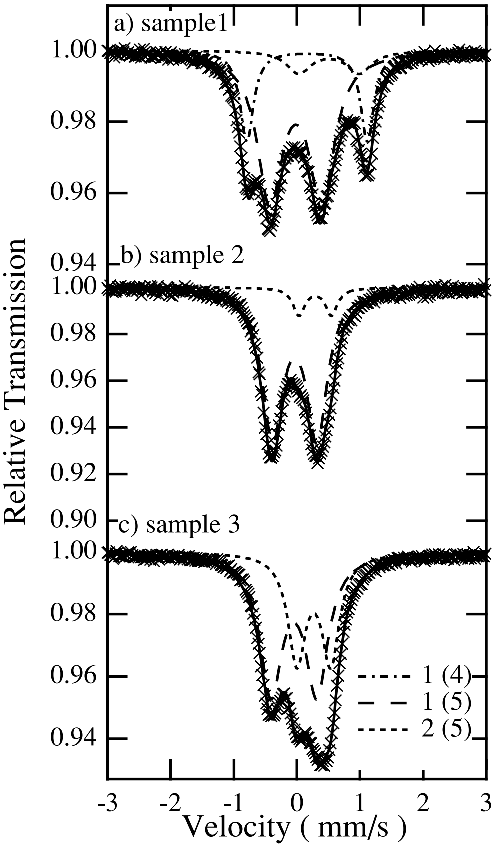

Fig. 2. Room temperature ^{57}Fe Mössbauer spectrums of $YSr_2FeCu_2O_{6+y}$ compounds at various annealing conditions. a) Reoxidization annealed sample,b) Superconducting sample (reoxidized and 190 atm high pressure O_2 annealed sample, c) 190 atm high pressure O_2 annealed sample (without reoxidization annealing).

Figs. 2(a) - (c) show room temperature Mössbauer spectra of the samples. The spectrum of sample 1 (Fig. 2(a)) can be fitted to three doublet and the spectra of sample 2-3 (Fig. 2(b) and (c)) can be fitted to two doublets. Isomer shift (IS) relative to Fe metal, quadrupole splitting (ΔEq), full-width-at-half-maximum (FWHM), and subspectra area (%) are summarized in Table 1. Similar values of isomer shift and quadrupole splitting were reported for $YBa_2Fe_xCu_{3-x}O_{6+y}$ [6, 3] and $YSr_2Fe_xCu_{3-x}O_{6+y}$ [7]. According to their reports, the present spectra of $YSr_2FeCu_2O_{6+y}$ could be assigned as follows. The doublet with highest isomer shift in Fig. 2(a) is due to the Fe ion located at Cu(2) site and other doublets are assigned to the Fe ion located at Cu(1) site. The doublet with larger quadrupole splitting of Cu(1) site is assigned to the Fe ion with four - fold oxygen coordination and the other doublet comes from the Fe ion with the five-fold oxygen coordination. The site notation (i)n in Table 1 denotes the subspectrum assigned to Fe ion in a Cu(i) site in n-fold oxygen coordination. Other spectra of Figs. 2(b) and (c) can be assigned by same way without the doublet 1(4). While the spectra of high pressure O_2 annealed sample (sample 2-3, Figs.2(b),(c)) is fitted with two quadrupole doublets, the spectrum of reoxidization annealed sample (sample 1,Fig.2 (a)) consists of three quadrupole doublets. The absence of the doublet assigned to 1(4) site indicates disappearence of Fe ions which occupy 1(4) site and the high pressure O_2 annealing is effective in spite of such low annealing temperature. From the result of our analysis, the area ratio of the quadrupole doublets shows drastic annealing. In the case of reoxidized samples, the distributions of Fe ion at Cu(1) sites are 90 % and 92 % for reoxidized (sample 1) and high pressure O_2 annealied sample (sample 2), respectively and the latter sample shows superconductivity. Without reoxidization annealing, 38% Fe ion distributes to Cu(2) site. (sample 3) Pissas *et al.* studied O_2 annealed sample and they also reported that the near 50% Fe distribution to the Cu(2) site. [7] This fact suggests that the reoxidization annealing promotes a preferred site occupation of Fe ion at Cu(1) site. It is difficult to analysis the spectrum of as synthesized specimen because the line width of the spectrum is too broad. This may be caused by the disorder of a oxygen surrounding Fe ion at Cu(1) site and this is consistent with the high temperature factor of the oxygen surrounding Cu(1) site observed at a neutron powder diffraction. [4, 8] Increasing annealing pressure of O_2, T_c and Meissner volume fraction increased linearly and it indicates that the high pressure O_2 annealing is also intrinsically necessary for superconductivity of $YSr_2FeCu_2O_{6+y}$.

Using ^{57}Fe Mössbauer spectroscopy we successfully determined the Fe distribution of the

Sample	Site	IS (mm/s)	ΔEq (mm/s)	FWHM (mm/s)	Area (%)
RO	1(5)	-0.017	0.822	0.230	67
(Sample 1)	2(5)	0.508	0.507	0.233	10
	1(4)	0.161	1.910	0.129	23
RO+O_2-HP (190atm)	1(5)	-0.030	0.726	0.205	92
(Sample 2)	2(5)	0.289	0.515	0.113	8
O_2-HP (190atm)	1(5)	-0.048	0.726	0.215	62
(Sample 3)	2(5)	0.267	0.535	0.169	38

Table 1. Mössbauer parameters of $YSr_2FeCu_2O_{6+y}$ at room temperatures. (RO : reoxidized, O_2-HP : high pressure O_2 annealed) The site notation (i)n denotes the subspectrum assigned to Fe in a Cu(i) site in n-fold oxygen coordination.

Fe ion. According to the analysis, it is revealed that the reoxidization annealing suppresses the distribution of Fe ion to Cu(2) site and a high pressure O_2 annealing provides an adequate oxygen to the sample. The mechanism of superconductivity of $YSr_2FeCu_2O_{6+y}$ system is revealed using ^{57}Fe Mössbauer spectroscopy.

References

[1] J. W. Lynn, B. Keimer, C. Ulrich, C. Bernhard, and J. L. Tallon, Phys. Rev. B **61** (2000) R14964.

[2] C. Bernhard, J. L. Tallon, Ch. Niedermayer, Th. Blasius, A. Golnik, E. Brücher, R. K. Kremer, D. R. Noakes, C. E. Stronach, and E. J. Ansaldo, Phys. Rev. B **59** (1999) 14099.

[3] M. G. Smith, J. B. Goodenough, R. D. Taylor, J. J. Neumeier, and J. O. Willis, Physica C **222** (1994) 157.

[4] P. R. Slater, and C. Greaves, Physica C **180** (1991) 299.

[5] T. Den, and T. Kobayashi, Physica C **196** (1992) 141.

[6] M. G. Smith, R. D. Taylor, and H. Oesterreicher , Phys. Rev. B **42** (1990) 4202.

[7] M. Pissas, G. Kallias, A. Simopolos, D. Niarchos, and A. Kostikas, Phys. Rev. B **46** (1992) 14119.

[8] T. Mochiku, Y. Mihara, Y. Hata, S. Kamisawa, M. Furuyama, J. Suzuki, K. Kadowaki, N. Metoki, H. Fujii and K. Hirata, J. Phys. Soc. Jpn. **71** (2002) 790.

[9] I. S. Lyubutin, V. G. Terziev, S. V. Luchko, A. Ya. Shapiro, A. M. Balagurov, and G. A. Bonch Osmolovsky, Physica C **199** (1992) 296.

3.11 The science of 3d transition-metal oxide system

M. Onoda, R. Arai, J. Hasegawa, A. Oyadomari, D. Kasuga, K. Kanbe, K. Sekine, T. Ikeda, T. Ohki, T. Harigae, S. Miyasaka and T. Mutoh

The structural and electronic properties of 3d transition-metal oxides and bronzes have been explored by means of x-ray four-circle diffraction and through measurements of magnetic resonance (NMR and EPR), magnetization, and electronic transport, in order to extract characteristic properties in the correlated electron system, electron-phonon-coupling system, quantum spin-fluctuation system, and novel materials.

At the Tandem Accelerator Center, Varian continuous-wave and Bruker pulse NMR spectrometers have been used. They have been working by a careful maintanance, but it is necessary to renovate them in order to obtain more detailed results. In the last two years, the pulse spectrometer has been partly improved.

In 2001-2002, the following investigations have been performed and a part of them have been published elsewhere [1–7]:

- Correlated-electron and electron-phonon-coupling systems
  - Correlation effect in $SrVO_{3-\delta/2}$ and $Sr_{1-x}Na_xVO_3$
  - Metal-insulator transition in V_6O_{13}
  - Metal-insulator transition in $Cu_xV_4O_{11}$
  - Mixed valence state in $Cu_7V_6O_{19}$
- Quantum spin-fluctuation system
  - Spin-gap state in the δ-$M_xV_2O_5$ (M = Ag, Tl, Na, K and Sr)
  - Geometrical frustration in $Cd_xZn_{1-x}V_2O_4$
  - Superexchange interaction in MV_nO_{2n+1} (M = divalent ion; $n = 1$, 3 and 5); $CdVO_3$, $Cd_{1-x}Ca_xV_3O_7$, SrV_5O_{11}, etc.
- Lithium secondary battery system
  - Li inserition effect in $M_{1+x}V_3O_8$ (M = Li, Na and Ag)
  - High capacity in $Ag_2V_{4-x}Mo_xO_{11}$

In this report, recent progress for the geometrically frustrated system is described briefly [7].

Geometrically frustrated spinel system

The normal spinel-type polaronic insulator MV_2O_4 with V^{3+} exhibits the frustration effect [8]. Here, M is a nonmagnetic divalent ion surrounded tetrahedrally such as Mg or Zn (the so-called *A*-site) and V has an octahedral coordination (*B*-site). As shown in Fig. 1, the network of the V ions is expressed by the linkage of a regular tetrahedron block that has the V ion at each apex as in the case of the pyrochlore-type compounds [9, 10]. On the other hand, LiV_2O_4 with apparent valence of $V^{3.5+}$ is a metal and it has recently been considered as being one of heavy-fermion system at low temperatures [11]. The mechanism of composition-induced metal–insulator transition in the $Li_xMg_{1-x}V_2O_4$ and $Li_xZn_{1-x}V_2O_4$ systems has been investigated from multiple viewpoints [12].

Recently, a tetrahedral mean field (TMF) theory of the magnetic susceptibility for the spinel *B*-sublattice or the pyrochlore lattice was proposed [13]. Here, the use of the exact solution of the susceptibility for a set of four interacting spins with J_{tet} in the corners of an isolated tetrahedron,

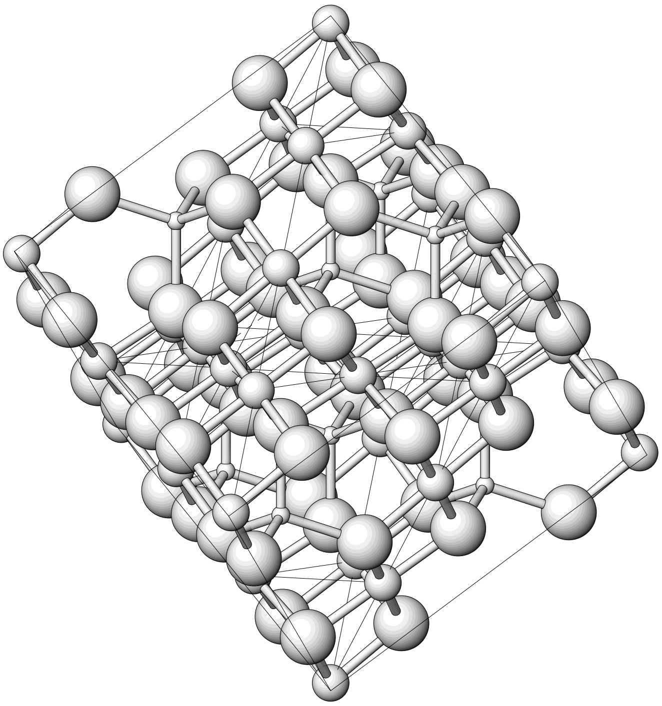

Fig. 1: The crystal structure of ZnV_2O_4 with the oxygen u parameter 0.3855 determined on the basis of the x-ray four-circle diffraction [9], where the small, middle and large spheres represent Zn, V and O atoms, respectively, and the short thin lines indicate the V–V edges of V_4 tetrahedra.

in other words, the spin-singlet *tetramer* is essential, and thus the appearance of a maximum in the susceptibility against temperature has been predicted. The ground-state properties for $S = 1$ were also investigated by breaking up each spin into a pair of $\frac{1}{2}$-spins [14]. It has been postulated that the twofold degeneracy of the spin singlets of the $S = \frac{1}{2}$ tetrahedron is lifted by the Jahn-Teller effect, which leads to the cubic–tetragonal transition with magnetoelastic interaction.

In a preceding report [15], the structural and magnetic properties of CdV_2O_4, which is isomorphous to MgV_2O_4 and ZnV_2O_4, have been described. On the basis of this result, let us see how the V_4-tetramer model [13] explains the susceptibility data above the cubic–tetragonal transition temperature T_{c1}, although they do not exhibit the maximum phenomena in the region where the crystal system is cubic. The susceptibility of the tetramer χ^{tet} for the present system is written

Table 1: The cubic–tetragonal transition temperature T_{c1}, the antiferromagnetic-like transition temperature T_{c2} (K), and the HTSE and TMF parameters for the magnetic susceptibilities of MV_2O_4, where M = Cd, Mg and Zn; the Curie constant C (emu K (mol V)$^{-1}$), the constant susceptibility χ_0 (10^{-4} emu (mol V)$^{-1}$) and the exchange coupling J (K) determined by the HTSE analysis [15]; the exchange coupling inside the tetrahedron J_{tet} (K) based on eq. (1).

M	T_{c1}	T_{c2}	C	χ_0	J	J_{tet}
Cd	97	35	0.98(2)	1.8(2)	44(1)	82.9(1)
Mg	64.5	45	0.93(6)	1.2(3)	92(7)	175.8(1)
Zn	52	44	0.96(6)	1.1(3)	92(7)	174.6(1)

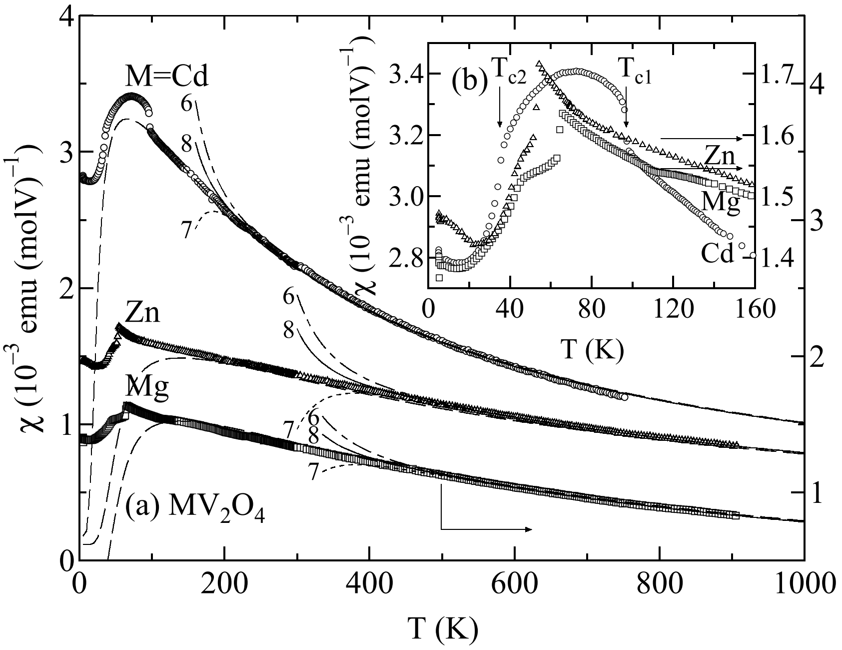

Fig. 2: (a) The temperature dependences of the magnetic susceptibilities χ of MV$_2$O$_4$, where M = Cd, Mg and Zn; (b) the behaviours at low temperatures. The full, dotted and dot-dashed curves in (a) denote results calculated in terms of HTSE of up to 8th-, 7th- and 6th-order, respectively [15]; and the dashed curves indicate fits to the tetramer model, where parameters used are listed in Table 1.

as

$$\chi^{\text{tet}} = \frac{3C}{2T}\frac{x + 5x^3 + 7x^6 + 5x^{10}}{1 + 6x + 10x^3 + 7x^6 + 3x^{10}} + \chi_0 \tag{1}$$

with $x = \exp(-J_{\text{tet}}/T)$, J_{tet} being defined before. Here, an interaction outside the tetrahedron is finally assumed to be zero as will be explained later. The dashed curves in Fig. 2(a) represent fits to eq. (1) with J_{tet} listed in Table 1, where C and χ_0 are fixed to the values determined in terms of the high-temperature series expansion (HTSE) analysis of up to 8th-order [15]. For M = Cd, the agreement between the experimental and calculated results in the cubic phase is satisfactory. In order to clarify the origin of the susceptibility maximum that appears to be reproduced roughly with this model, the low-temperature structure should be determined precisely. On the other hand, for M = Mg and Zn, the data above $T \approx J_{\text{tet}}$ are explained by this model, but it is difficult to fit those below J_{tet}. For all of the compounds, J_{tet} is twice J within a standard deviation, which is equivalent to the condition for the high-temperature limit in the TMF model. It should be noted that a finite interaction outside the tetrahedron that has been introduced in reference [13] does not improve the agreement significantly.

In summary, the susceptibility behaviour in the cubic phase of CdV$_2$O$_4$ with T_{c1} = 97 K and J = 44 K agrees well with that of the spin-singlet tetramer with $J_{\text{tet}} = 2J$. On the other hand, for the isomorphous compounds MgV$_2$O$_4$ and ZnV$_2$O$_4$ with $J_{\text{tet}} > T_{\text{c1}}$, it is difficult to fit all of the susceptibility data in the cubic phase in the framework of the present tetramer model. Therefore, in the vanadium spinel with $S = 1$, the application of this model is limited to the temperature region above $T \approx J_{\text{tet}}$, and the present bound state may be regarded as *pseudotetramers.* In other words, this restriction may justify the use of apparently *isolated* tetramer model for the regular spinel B-sublattice. In order to understand the magnetic properties for the cubic phase at temperatures below J_{tet}, further theoretical investigations are necessary.

References

[1] M. Onoda and K. Kanbe: J. Phys.: Condens. Matter **13** (2001) 6675.

[2] M. Onoda and R. Arai: J. Phys.: Condens. Matter **13** (2001) 10399.

[3] A. Fujimori, M. Onoda *et al*: J. Elec. Spec. Relat. Phenom. **117** (2001) 277.

[4] K. Okazaki, A. Fujimori and M. Onoda: J. Phys. Soc. Jpn. **71** (2002) 822.

[5] N. Nishiguchi, M. Onoda and K. Kubo: J. Phys.: Condens. Matter in press.

[6] M. Onoda and J. Hasegawa: J. Phys.: Condens. Matter in press.

[7] N. Nishiguchi and M. Onoda: submitted to J. Phys.: Condens. Matter

[8] H. Mamiya and M. Onoda: Solid State Commun. **95** (1995) 217.

[9] M. Onoda: unpublished results (1996).

[10] H. Sakai, K. Yoshimura, H. Ohno, H. Kato, S. Kambe, R. E. Walstedt, T. D. Matsuda, Y. Haga and Y. Ōnuki: J. Phys.: Condens. Matter **13** (2001) L785.

[11] S. Kondo S, D. C. Johnston, C. A. Swenson, F. Borsa, A. V. Mahajan, L. L. Miller, T. Gu, A. I. Goldman, M. B. Maple, D. A. Gajewski, E. J. Freeman, N. R. Dilley, R. P. Dickey, J. Merrin, K. Kojima, G. M. Luke, Y. J. Uemura, O. Chmaissem and J. D. Jorgensen: Phys. Rev. Lett. **78** (1997) 3729.

[12] M. Onoda, H. Imai, Y. Amako and H. Nagasawa: Phys. Rev. B **56** (1997) 3760.

[13] A. J. García-Adeva and D. L. Huber: Phys. Rev. Lett. **85** (2000) 4598.

[14] Y. Yamashita and K. Ueda: Phys. Rev. Lett. **85** (2000) 4960.

[15] M. Onoda, N. Nishiguchi, R. Arai, I. Amemiya, K. Kogure, J. Hasegawa, A. Oyadomari, D. Kasuga, K. Kanbe, H. Imai, K. Sekine, A. Tokunaga and T. Banno: *UTTAC Annual Report* (2001) p. 80.

4.1 Suppression of nuclear-cascade gamma-ray background analysis

K. Furuno, A. Tanaka, H. Ohsima, M. Ishizuka, S. Yokose, K. Sasa, and T. Komatsubara

Resonant nuclear reaction analysis(RNRA) using the ^{1}H(^{15}N,$\alpha\gamma)^{12}$C or ^{1}H(^{19}F,$\alpha\gamma)^{16}$O reaction is widely used in hydrogen analysis. Most of investigations reported so far have been performed by means of low energy accelerators, and consequently limited to measurements of hydrogen concentration near the surface of samples.

One of recent important subjects in earth science is the measurement of hydrogen concentration in fluid inclusions confined in minerals or rocks. Since the size of fluid inclusions is in the range from 30 to 100 microns, the energy of ^{19}F beam in the ^{1}H(^{19}F,$\alpha\gamma)^{16}$O reaction must be increased up to about 70 MeV to cover the whole range of a fluid inclusion as large as 30 microns. A serious problem at such high beam energies is that the yield of continuum γ rays due to compound nuclear reactions with carbon, oxygen, and silicon in silicate samples becomes huge background for the 6.13 MeV γ ray originated from the reaction with hydrogen.

The continuum γ rays are comprised of statistical and cascade γ rays emitted from fusion-evaporation residues, so that several number of γ rays are emitted per one nuclear reaction event. The number of γ rays is defined as γ multiplicity M in nuclear physics. On the contrary, the γ multiplicity of $M = 1$ is dominant in the ^{1}H(^{19}F,$\alpha\gamma)^{16}$O reaction for the ^{19}F energies up to 70 MeV, because excited states in ^{16}O higher than 7.15 MeV are above the ^{12}C$+\alpha$ threshold and the probability of γ-ray emission from excited states higher than the threshold becomes very low by virtue of competeing α-particle emissions. This differnce of the γ multiplicity in the compound nuclear reactions other than hydrogen from the ^{1}H(^{19}F,$\alpha\gamma)^{16}$O reaction can be utilized to partly suppress the continuum γ ray background by using a multiple γ-ray detector system operated in the anti-coincidence mode.

A test experiment was performed with the arrangement shown in Fig. 1. A ^{19}F beam delivered by the 12 UD Pelletron tandem accelerator was focused onto a target on the end plate of the Faraday cup. The target was a silica glass of 8 mm in diameter and 0.5 mm in thickness. The surface of the glass was artificially hydrated at a temperature of 450°C and at pressure as high as 60 MPa. To avoid charging up during beam irradiation, the surface of the target was coated with 100 A thick carbon. Four tightly bounded NaI detectors were placed behined the silica glass target.

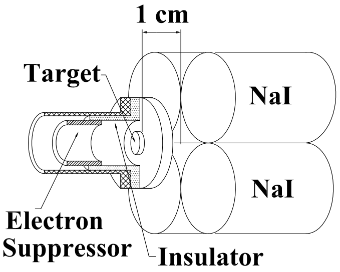

Fig. 1. Target and detectors

This arrangement of the detectors was employed to introduce light for a microscope for observation of samples in the new vaccum chamber under construction. The distance between the target and front ends of NaI detectors was 1 cm. Fig. 2 shows a block diagram of the electronics. Timing signals from four detectors were fed into a linear FAN-IN/FAN-OUT module. The threshold of CFD connected to FAN-IN/FAN-OUT was adjusted at a level slightly higher than one logic pulse height. The output pulses from CFD were coincidence signal when at least two NaI detectors fired, and were converted to anti-coincidence signals by taking $\overline{\mathrm{OUT}}$ in DISC-A connected to CFD. Energy signals from each NaI detector were gated by the anti-coincidence pulses. Gamma rays emitted simultaneously from the compound nuclear reactions hit more than two NaI detectors, and thus they were rejected with some probability which depends on solid angles and detction efficiencies of the NaI detectors.

Typical γ ray spectra obtained in this test experiment are displayed in Fig. 3, and Fig.4. The spectrum in Fig. 3 was observed at the ^{19}F beam energy of 20 MeV. The energy calibration was carried out using standard sources

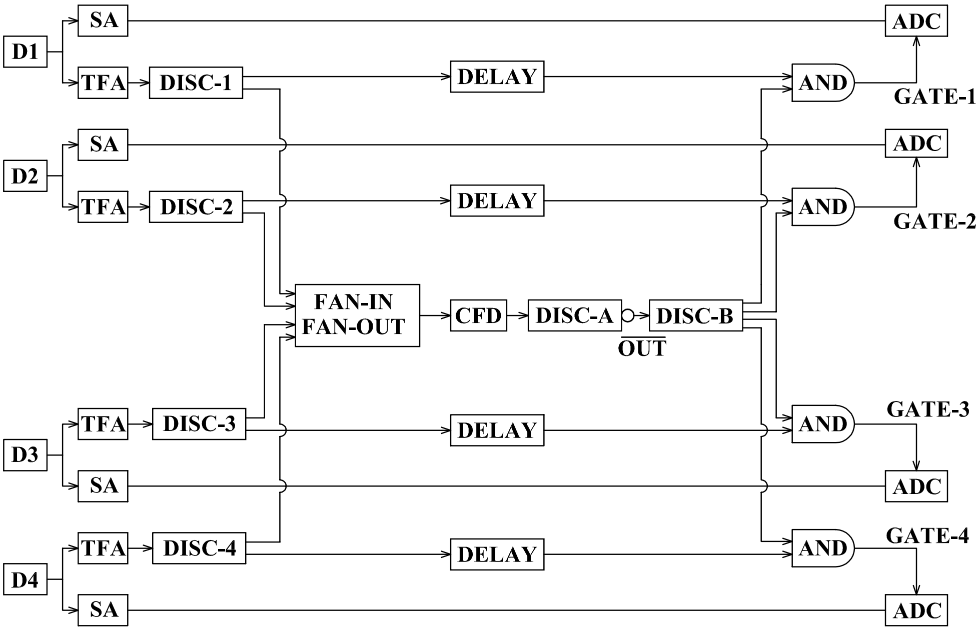

Fig. 2. Block diagram of the γ ray detection system. SA's are spectroscopy amplifiers(EG&G ORTEC model 572). TFA's are timing filter amplifiers(EG&G ORTEC model 474). DISC-1, DISC-2, DISC-3, DISC-4, DISC-A and DISC-B are fast discriminators(LeCroy model 821). The linear FAN-IN/FAN-OUT is the model 428F supplied by LeCroy. CFD is a constant fraction discriminator(EG&G ORTEC model 473A). A 4 channel coincidence module(LeCroy model 622) was used as AND's.

of ^{137}Cs(0.661 MeV), ^{22}Na(1.27 MeV), ^{60}Co(1.33 MeV) and Am+Be(4.44 MeV). At 20 MeV, the center-of-mass energy is much lower than the Coulomb barrier heights between nuclei other than hydrogen and incident ^{19}F nucleus, and the cross section of compound nuclear reactions are very small. The background under the 6.13 and 6.92 MeV γ rays is almost negligible. At a bombarding energy of 33 MeV, however, the background becomes huge as shown in Fig. 4. The upper spectrum is a singles spectrum, while the lower spectrum is observed in the anti-coincidence mode. The resolving time for the 2-fold coincidence was 50 ns. The ratio of the anti-coincidence yield to singles yield was 0.64 for an integrated number of counts between the channels 470 and 570.

This experimental ratio of the yields can be compared with the following theoretical prediction. Let the number of γ-ray detectors and the γ multiplicity be N and M, respectively. We assume that detection efficiencies $\Omega\varepsilon/4\pi$ are identical for all detectors. The probability of p-fold coincidence is given by[1]

$$P_{N,p}^{M} = _N C_p \sum_{l=0}^{p} (-1)^{p-l} {}_pC_l \left[1-(N-l)\frac{\Omega\varepsilon}{4\pi}\right]^M , \tag{1}$$

where $_NC_p$ stands for the number of combinations for taking p out of N.

The probability of singles events is simply given by $M(\Omega\varepsilon/4\pi)$.

The probability that more than two γ rays hit one of the detectors simultaneously and other γ rays do not hit any other detectors can be written as

$$P' = \sum_{q=2}^{M} {}_MC_q \left(\frac{\Omega\varepsilon}{4\pi}\right)^q \left[1-\{N-(q-1)\}\frac{\Omega\varepsilon}{4\pi}\right]^{M-q} . \tag{2}$$

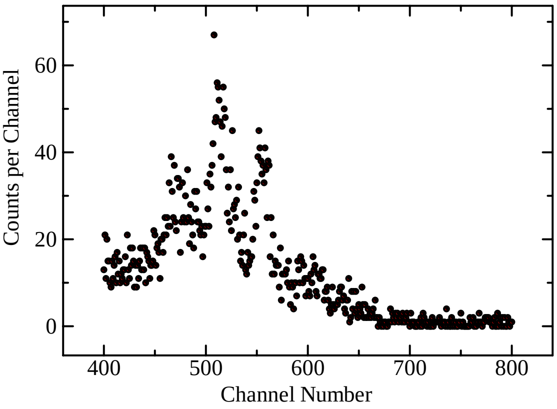

Fig. 3. A gamma ray spectrum observed at 20 MeV

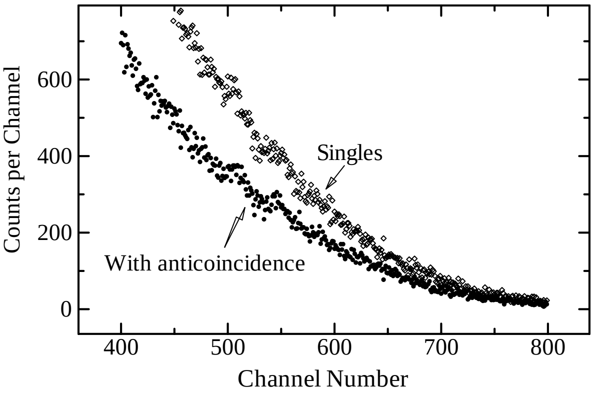

Fig. 4. Gamma ray spectra observed at 33 MeV

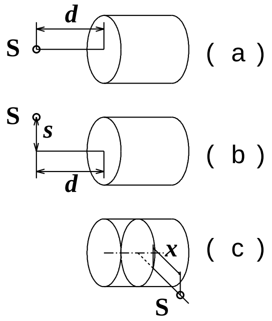

Fig. 5. Source positions with respect to the detector

We estimated the γ multiplicity M to be 5 from the angular momentum carried into the compound nucleus at the ^{19}F beam energy of 33 MeV and reaction Q values. The detection efficiency $\Omega\varepsilon/4\pi$ was estimated in the following manner. In the experimental arrangement shown in Fig. 1, the source is not on the axis of the scintillator. Relative efficiencies were measured for three source positions to the detectors shown in Fig. 5. The first arrangement in Fig. 5(a), the source was placed on the axis and the distance d was changed. The second arrangement in Fig. 5(b) the detector was displaced by the distance s with fixed d. The third arrangement in Fig. 5(c), the source was moved in the radial direction. The experimetal results are plotted in Fig. 6 as functions of distances d, s and x. The efficiency is normalized to unity at the distances of $d = 0.4$ and $s = 0$ cm. The absolute efficiency for this source position was calculated using the following well known formula;

$$\begin{aligned}\frac{\Omega\varepsilon}{4\pi} &= \frac{1}{2}\int_0^{\theta_1}\left[1-\exp\left\{-\mu_l(E_\gamma)\frac{L}{\cos\,\theta}\right\}\right]\sin\theta\,d\theta \\ &+\frac{1}{2}\int_{\theta_1}^{\theta_0}\left[1-\exp\left\{-\mu_l(E_\gamma)\left(\frac{R}{\sin\,\theta}-\frac{d}{\cos\,\theta}\right)\right\}\right]\sin\theta\,d\theta,\end{aligned} \tag{3}$$

where R and L are the radius and length of the scintillator. The angles θ_0 and θ_1 are given by

$$\theta_0 = \tan^{-1}\frac{R}{D} \qquad \text{and} \qquad \theta_1 = \tan^{-1}\frac{R}{D+L}. \tag{4}$$

Substituting numerical values of $d = 1$ cm, $L = 7.6$ cm, $R = 3.8$ cm, we obtained the efficiency to be $(\Omega\varepsilon/4\pi)_{\rm axis} = 0.134$. We took the total linear absorption coefficient to be $\mu_l(E_\gamma) = 0.13$ [cm^{-1}] at a γ-ray energy of 6.13 MeV from the table reported by Strom and Israel[2]. The result shown in Fig. 6 indicates that the effciecy drops to 0.35 at $s = 5.4$cm. Multiplying this factor by the efficiency on axis(0.134), we obtained the detection efficiency of 0.047. With this efficiency, the probabilities of $P^M_{N,p}$ and $P_{\rm singles}$ $(M(\Omega\varepsilon/4\pi) + P')$ were estimated to be 0.0992 and 0.251, respctively. Thus, the ratio of anticoincidence counts to the singles counts is calculated to be 0.6. This result is in reasonable agreement with the experimental ratio of 0.64. If we use BGO detectors instead of NaI detectors, the ratio would be improved to 0.5.

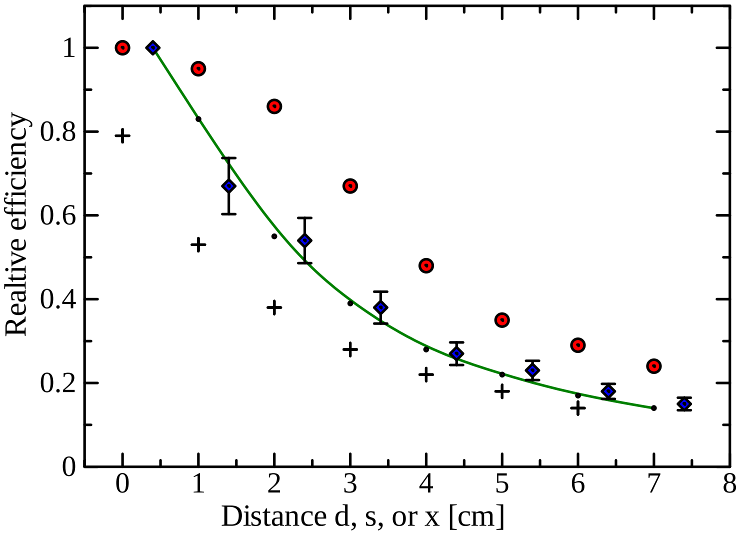

Fig. 6. Detection efficiency as a function of the displacement of the source position. Closed circles are relative efficiencies in the arrangement (b) in Fig. 5 with the distance $d = 1$cm. Closed diamonds indicates efficiencies obtained for the arrangement (a) in Fig. 5. Crosses are the results for the arrangement (c) in Fig.5. The solid curve shows an efficiency for the arrangement (a) calculated with eq. (3).

References

[1] S.Y. Van der Werf, Nucl. Instr. Meth. **B84** (1994) 380-392.

[2] E. Strom and H.I. Israel, Nucl. Data Tables, **A7** (1970) 565-681.

4.2 Hydrogen analysis by proton ERCS technique

T. Komatsubara, K. Sasa, K. Shima, H. Ohshima, H. Kimura, Y. Tajima, T. Takahashi, S. Ishii, Y. Yamato, T. Kurosawa*, K. Furuno

* Institute of Geoscience, Univ. of Tsukuba, Tsukuba, Ibaraki 305-8577, Japan

For applications to geo-scientific researches, hydrogen analysis has been emphasized to be important for the evolution and dynamics of the earth[1, 2]. To develop a hydrogen analysis method for mineral samples, a test experiment of elastic recoil coincidence spectrometry (ERCS) [3, 4] was carried out.

A stacked target which consists of four aluminum foils of 50 μm in thickness and five mylar films was irradiated by proton beam at 17 MeV. Thickness of the mylar film (polyethylene terephthalate, $(C_{10}H_8O_4)_n$) was measured to be 0.79mg/cm^2 which corresponds to 5.7 μm thick. The hydrogen density in the mylar film is calculated to be 33 μg/cm^2.

For detection of proton-proton coincidence events produced from elastic scattering by proton in the mylar films, two Si detectors of 2mm in thickness were placed at ±45° with respect to the beam axis. The distances from the stacked target to the detectors were both 125 mm. Defining slits of 9 mm in diameter were located in front of the detectors. Solid angles of the detectors were both 4.1 msr. Coincidence time window was adjusted to be 40 nsec by using TAC module.

When the stacked sample was irradiated by high energy proton beam a measured spectrum was very complex due to many nuclear reactions. Fig. 1(a) shows a singles spectrum which includes many elastic and inelastic particles from aluminum, oxygen, carbon and hydrogen in the stacked targets. However, the coincidence measurement can select proton-proton elastic scatterings. Projected spectrum of the coincidence events is shown in Fig. 1(b). A small bump in Fig 1(a) is also the coincidence spectrum compared with the singles. Singles and coincidence counting rates were 2400 and 35 cps, respectively, with 0.4 nA of proton beam intensity. The rate of chance coincidence events can be calculated to be 0.2 cps.

As a result of the coincidence measurement, 2-dimensional spectrum is shown in Fig. 2, in which both axis show measured energies by the two detectors. Five lines correspond to scattering protons from each layer of five mylar foils. When a projectile proton is scattered by a proton in the target, the kinetic energy is shared with the recoil proton. Since stopping power for the scattered and recoil protons are twice larger than for the projectile, the sum of energy losses depends on the depth from the ejecting surface. Fig. 3(a) shows a diagonal projection of the 2-dimensional matrix. Energies calculated using stopping powers in reference [5] are compared in Fig. 3(b). Peak positions of sum energies of two protons are well reproduced by the calculation. Measured intensities for the five peaks are shown in Fig. 4 as a function of the depth from the ejecting surface. Exponential decay of the intensity observed in this figure could imply single and/or multiple scatterings of scattered and recoil protons.

From the test experiment, it has clearly turned out that proton density and its depth profile can be measured by the proton-proton ERCS with high energy proton beam.

References

[1] M. Kurosawa, S. Sueno, K. Shima, H. Oshima, S. Ishii, H. Kamiya, S. Kimoto, H. Ohyi, K. Hayashi, Nucl. Inst. and Meth. B 142 (1998) 599

[2] S.H. Sie, G.F. Suter, A. Chekhmir, T.H. Green, Nucl. Inst. and Meth. B 104 (1995) 261

[3] B.L. Cohen, C.L. Fink, J.H. Degnan, J. Appl. Phys. 43 (1972) 19

[4] H.C. Hofsäss, N.R. Parikh, M.L. Swanson, W.K. Chu, Nucl. Inst. and Meth. B 45 (1990) 151

[5] J.F. Ziegler, J.P Biersack, U. Littmark, "The Stopping and Range of Ions in Solids", Pergamon Press, New York (1985); Program SRIM, J.F. Ziegler, IBM-Research

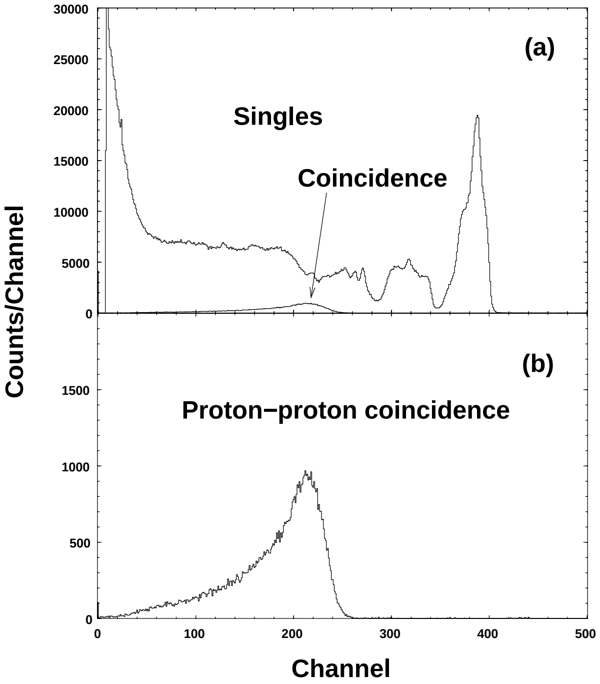

Fig. 1 (a) A singles and a projection of coincidence events of charged particle energy spectra measured by a Si detector. (b) The projection of the coincidence events with expanded scale.

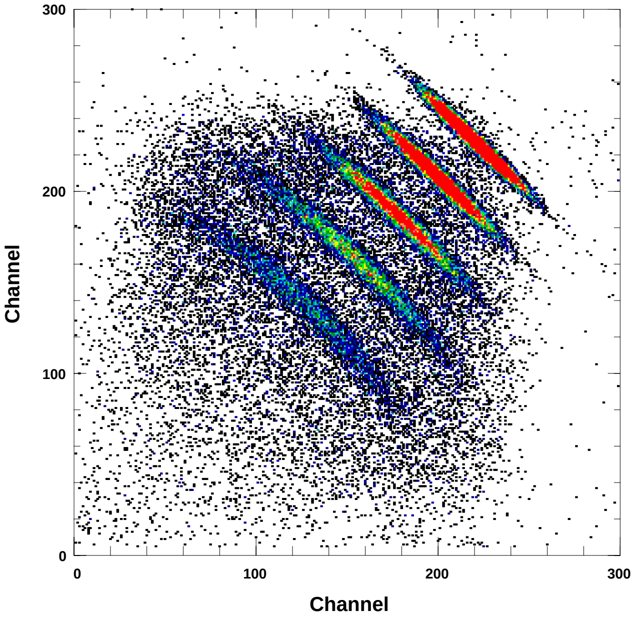

Fig. 2 A 2-dimensional spectrum for a stacked target of 4 aluminum and 5 mylar foils.

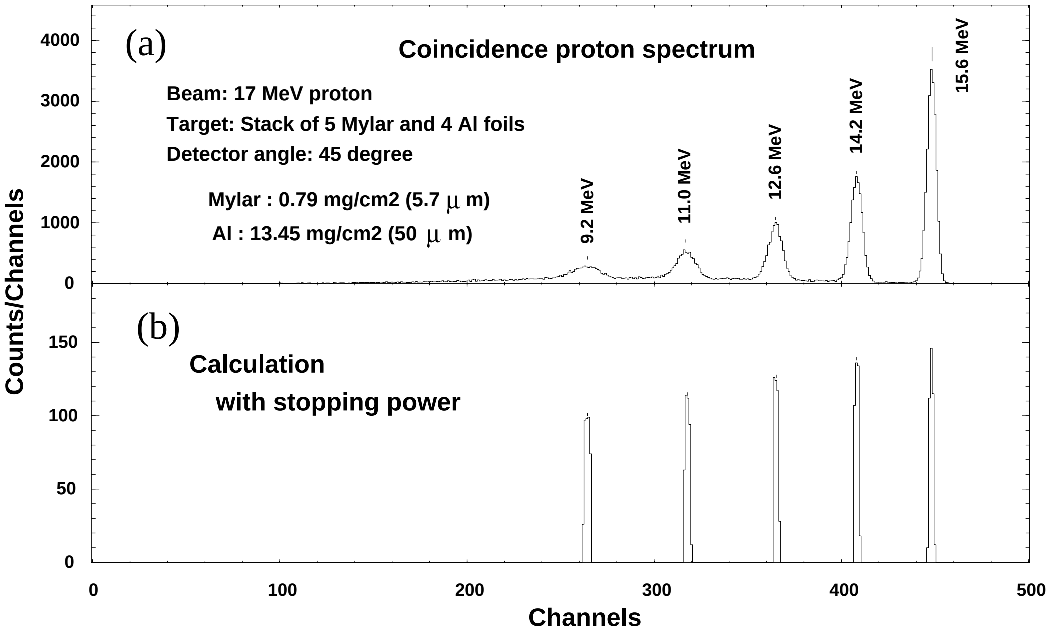

Fig. 3 (a) Diagonal projection of the 2-dimensional spectrum shown in Fig. 2. (b) A result of calculation by use of stopping power of incident and recoil protons. Sum of energies of scattered and recoil protons are shown in a unit of MeV.

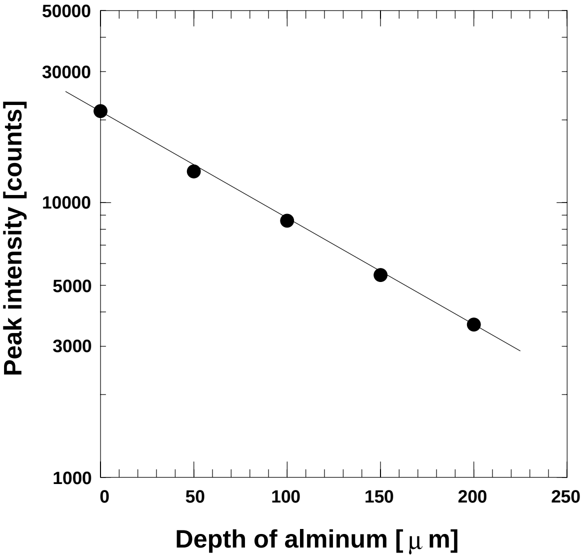

Fig. 4 Measured intensity corresponding to 5 mylar foils as a function of distance from the ejecting surface.

4.3 Status of Tsukuba AMS system

Y. Nagashima, R. Seki, T. Takahashi, T. Matsuhiro, K. Sasa, and H. Kume[1]

In this year, AMS group has made great efforts towards achieving higher precision and reproducibility on the ^{36}Cl measurements. As one of the instrumental improvements, the high-voltage power supply for the electrostatic deflector located just after the ion-source einzel lens has been replaced by new one because of the lack of its stability.

In order to investigate the influence of nuclear power plants on an environment, ^{36}Cl in soils was extensively studied. The ^{36}Cl is very suitable isotope to see the long-term environmental changes due to such human activities as man made nuclear activities because of both its very long halflife of about 0.3 million years and very low natural abundance less than 10^{-14} in the ratio of ^{36}Cl to ^{35}Cl. The soils were sampled in the area of Tokai and in the Tsukuba area. Fig. 1 shows a horizontal distribution of 36Cl in Tokai village. The mark JCO shows the location of a JCO nuclear fuel company in which a critical nuclear accident occurred on September 30, 1999. The results indicate that the JCO accident fortunately caused little radioactive contamination in the environment in the vicinity of JCO. In contrast with JCO area, it was clearly demonstrated that the ^{36}Cl to ^{35}Cl of Tokai samples are 10 - 100 times as large as that of Tsukuba samples, and that the ratios in the coastal area were much higher than those in the inland area. These experimental evidences imply environmental pollution brought by the human activities related to a nuclear power. Many facilities for nuclear research and plant are constructed and are operated in the coastal area of Tokai village, but not so many in the inland area. In order to understand the origin of this high ratio of ^{36}Cl/Cl, we continue to measure the ^{36}Cl contents in many samples taken from a site of other nuclear plants.

The DS86 dosimetry system has been used for survivors of the Hiroshima and Nagasaki atomic bombs since 1987. In the thermal neutron evaluation, a systematic discrepancy has been observed between ^{152}Eu data measured by Shizuma and Nakanishi and the calculation based on the DS86. As one of the contribution to understand the source of the discrepancy, the measurements of ^{36}Cl in granite samples has been commenced with the Tsukuba AMS system. Seventeen bombed granite samples were chosen and analyzed. These granites are sampled at the location of 146 - 1400m distance from hypo-center. In addition to the bombed granites, 7 un-bombed granite samples were prepared for background estimation because ^{36}Cl was also created in the granite itself as an in-situ formation. Each granite sample was separated into 4 blocks and each block was sent to 4 laboratories. One laboratory at Kanazawa takes the responsibility for ^{152}Eu measurement. Remaining 3 laboratories, Tsukuba, Munchen and LLNL, bear the responsibility for ^{36}Cl measurement. The ratios of ^{36}Cl to ^{35}Cl of 14 samples have been measured. It seems that there is little discrepancy between the DS86 calculation and the ^{36}Cl measurement. The investigation is still going on. It is expected that the origin of the discrepancy will be made clear after finishing of the inter-comparison measurements by 4 laboratories.

---

[1] National Institute for Environmental Studies

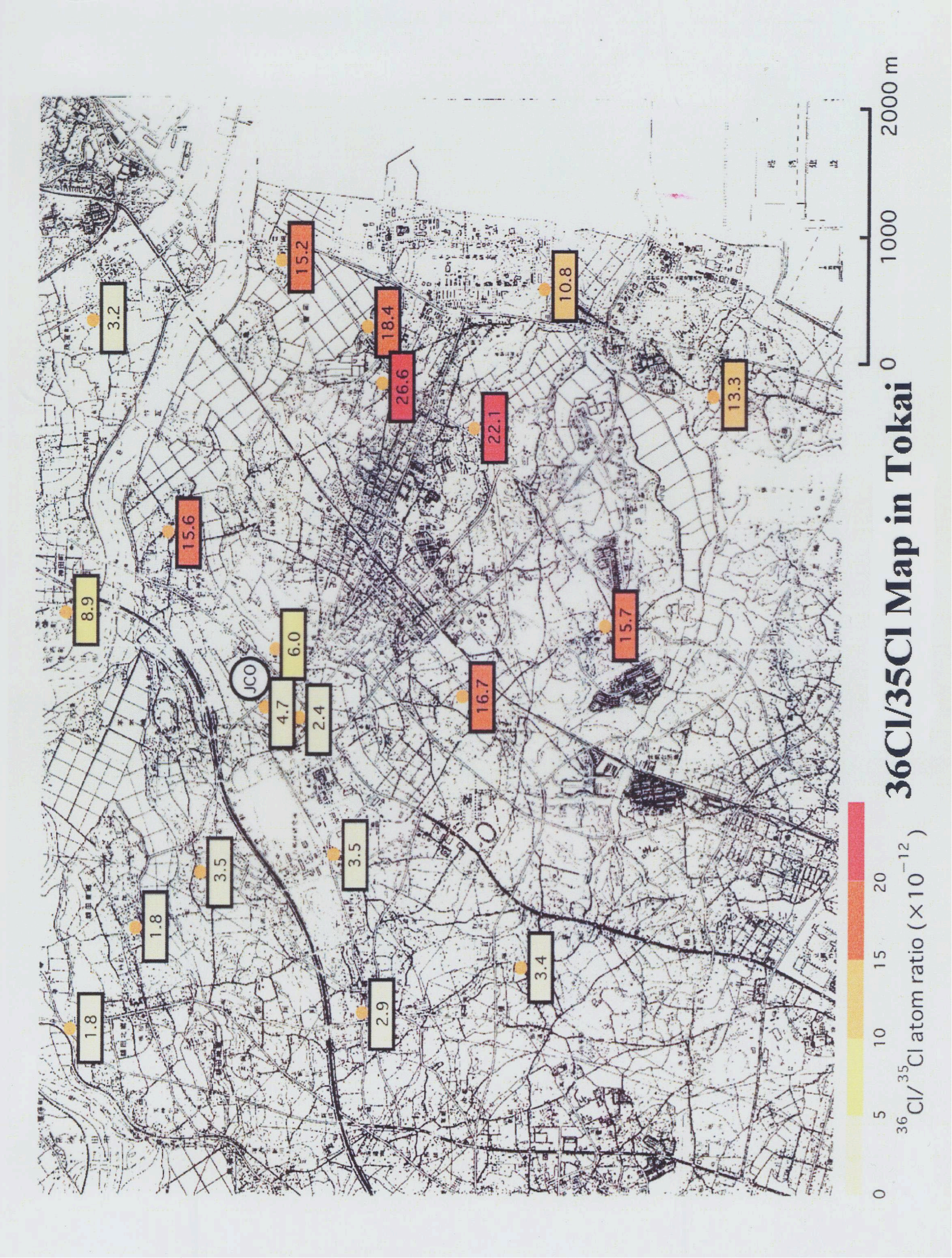

Fig.1 ^{36}Cl/^{35}Cl ratio map in Tokai village

5. LIST OF PUBLICATIONS

NUCLEAR PHYSICS----EXPERIMENT

C.B. Moon, S.J. Chae, J.H. Ha, T. Komatsubara, Y. Sasaki, T. Jumatsu, K. Yamada, K. Satou, K. Furuno
Level structure of ^{120}Cs
Nucl. Phys. A696 (2001) 45-63.

T. Shizuma, K. Matsuura, Y. Toh, Y. Hayakawa, M. Oshima, Y. Hatsukawa, M. Matsuda, K. Furuno, Y. Sasaki, T. Komatsubara, Y.R. Shimizu
Multi-quasiparticle states and K-forbidden transitions in ^{183}Os,
Nucl. Phys. A696 (2001) 337-370.

C.B. Moon, T. Komatsubara, K. Furuno
Rotational bands built on the proton h(11/2) orbital in ^{121}Cs
Journal of the Korean Physical Society 38 (2001) 83-87.

Y.H. Zhang, T. Hayakawa, M. Oshima, Y. Toh, J. Katakura, Y. Hatsukawa, M. Matsuda, N. Shinohara, T. Ishii, H. Kusakari, M. Sugawara, T. Komatsubara
Doubly decoupled structure in odd-odd 178-186Ir nuclei,
Chinese Physics Letters 18 (2001) 27-29.

Y.H. Zhang, T. Hayakawa, M. Oshima, Y. Toh, J. Katakura, Y. Hatsukawa, M. Matsuda, N. Shinohara, T. Ishii, H. Kusakari, M. Sugawara, T. Komatsubara, K. Furuno
Search for signature inversion in the $\pi i_{13/2}$ x $\nu i_{13/2}$ band in odd-odd ^{178}Ir
Chinese Physics Letters 18 (2001) 1323-1326.

X.H. Zhou, Y. Zheng, Y.H. Zhang, Z. Liu, Q.Y. Pan, Z.G. Gan, T. Hayakawa, M. Oshima, Y. Toh, T. Shizuma, J. Katakura, Y. Hatsukawa, M. Matsuda, H. Kusakari, M. Sugawara, K. Furuno, T. Komatsubara,
In-Beam Study of ^{145}Tb,
Eur.Phys.J. A 12 (2001) 253.

Y.H. Zhang, T. Hayakawa, M. Oshima, J. Katakura, Y. Hatsukawa, M. Matsuda, H. Kusakari, M. Sugawara, T. Komatsubara, K. Furuno
Configuration-dependent band structures in odd-odd ^{180}Ir
Phys.Rev. C65 (2002) 014302.

K. Nishio, H. Ikezoe, S. Mitsuoka, K. Satou, S.C. Jeong
Effects of nuclear deformation on fusion probability in the reactions of ^{82}Se + ^{nat}Ce and ^{76}Ge + ^{150}Nd near the Coulomb barrier.
Phys.Rev. C63 (2001) 044610.

T.Katabuchi, K.Kudo, K.Masuno, T.Iizuka, Y.Aoki and Y.Tagishi,
Polarization transfer for the ^{2}H(d,p)^{3}H reaction at $\theta=0^\circ$ at a very low energy
SPIN 2000, 14th Int. Spin Physics Symp. Osaka Japan 2000, AIP conf. Proceedings 570, p.694-698, 2001

T.Katabuchi, K.Kudo, K.Masuno, T.Iizuka, Y.Aoki and Y.Tagishi,
Polarization transfer coefficient $K^{y'}_{y}$ in the $^{2}H(d,p)^{3}H$ reaction at $\theta=0^{\circ}$ at very low energies
Phys. Rev. C 64 (2001) 047601-1-047601-3.

N.Kawachi, T.Katabuchi, M.Yamaguchi and Y.Tagishi,
Real-time measurement of implanted deuterons by using the nuclear reaction $^{2}H(d,p)^{3}H$
15th Intern. Conf. on Ion Beam Analysis, Cairns, Australia (2001), Nucl. Instrum. Methods B190 (2002) 887.

NUCLEAR PHYSICS----THEORY

T. Une ,
Study of tilted rotation based on the method of variation after projection,
Prog. Theor. Phys. 106 (2001) 941.

HIGH ENERGY NUCLEAR PHYSICS

T. Abbott, Y. Miake, et.al.,
Systematics of midrapidity transverse energy distributions in limited apertures from p + Be to Au + Au collisions at REL at relativistic energies.
Phys.Rev.C63 (2001) 064602, Erratum-ibid.C64 (2001) 029901.

K. Adcox, S. Esumi, A. Kiyomichi, Y. Miake,M. OnoM. Suzuki, H. Tsuruoka,et.al.,
Measurement of midrapidity transverse energy distribution from S(NN)**(1/2) = 130-GeV Au+Au Collision at RHIC.
Phys.Rev.Lett.87 (2001) 052301.

K. Adcox, S. Esumi, A. Kiyomichi, Y. Miake,M. OnoM. Suzuki, H. Tsuruoka,et.al.,
Suppression of hadrons with large transverse momentum in central Au+Au collisions at S(NN)**(1/2)= 130-GeV.
Phys.Rev.Lett.88 (2002) 022301.

M.M. Aggarwal, Y. Miake, et.al.,
Direct photons in WA98.
Nucl.Phys.A698 (2002) 135-142.

L. Rosselet, Y. Miake, et.al.,
One-, two- and three-particle distributions from central Pb+Pb collisions at 158-A-GeV/c.
Nucl.Phys.A698 (2002) 647-650.

W.A. Zajc, S. Esumi, A. Kiyomichi, Y. Miake,M. OnoM. Suzuki, H. Tsuruoka,et.al.,
Overview of PHENIX results from the first RHIC run.
Nucl.Phys.A698 (2002) 39-53.

M.M. Aggarwal, Y. Miake, et.al.,
Transverse mass distributions of neutral pions from ^{208}Pb induced reactions at 158-A-GeV.
Eur.Phys.J.C23 (2002) 225-236.

Y. Miake,
High PT Project of PHENIX,
Yonsei-Tsukuba Workshop, Yonsei, Korea, Aug.20-22, 2001

D. Adamova, S. Esumi et al.
New results from CERES.
Nucl.Phys.A698 (2002) 253-260.

I.G. Bearden, S. Esumi et al.
Two Kaon correlations in central Pb + Pb collisions at 158 A GeV/c.
Phys.Rev.Lett.87 (2001) 112301.

Mikhail L. Kopytine, S. Esumi et al.
Event texture search for critical fluctuations in Pb + Pb collisions.
Nucl.Phys.A698 (2002) 651-654.

I.G. Bearden , S. Esumi et al.
One-dimensional and two-dimensional analysis of 3 PI correlations measured in Pb + Pb interactions.
Phys.Lett.B517 (2001) 25-31.

ATOMIC AND SOLID STATE PHYSICS, AND CLUSTER SCIENCE
H.Kudo, T.Kumaki, K.Haruyama, Y.Tsukamoto, S.Seki, H.Naramoto,
Structural analysis of bent KCl and NaCl crystals with ion-induced electron spectroscopy.
Nucl. Instrum. & Methods B174 (2001) 512-518.

H.Kudo, K.Haruyama, T.Kinoshita, K.Narumi, H.Naramoto and S.Seki,
Carbon KLL Auger electron emission from HOPG bombarded by 1 MeV H^+
15th Intern. Conf. on Ion Beam Analysis (Cairns, Australia, July, 2001), Nucl. Instrum. Methods B190 (2002) 160.

Ion-Induced Electron Emission from Crystalline Solids,
H. Kudo,
Springer Tracts in Modern Physics, vol. 175, Springer, Berlin, Heidelberg, 2002.

M. Imanaka, T. Kurita, M. Tsukada, I. Arai, S.M. Lee and T. Nakagawa,
Effect of a biased electrode on operation of electron cyclotron resonance ion source using liquid He free superconduction solenoid coils,
Rev. Scientific Instruments, 73 (2002) 592-594.

I. Arai, H. Sasaki, J. Hirose, K. Teranishi and S.M. Lee,
Abundance spectra of clusters for various metals in sputtering and their formation mechanism,
Transactions of Materials Research Society of Japan, 27 (2002) 193-196.

M. Imanaka, T. Kurita, T. Nakagawa, H. Sasaki, S.G. Lee, I. Arai and S.M. Lee,
Highly-charged ion beam for study of cluster physics,
Ibid., pp181-184

M. Imanaka, T. Kurita, M. Tsukada, T. Nakagawa, S.M. Lee,
The effect of a biased electrode of ECR ion source using liquid He free superconducting solenoid coils ,
The 9th Intern. Conf. on Ion Sources, Oakland, California USA, Sep. 2001.

S.M. Lee,
Atomic cluster and nanoscience,
Invited lecture, Natural science division, Academy of Science, Democratic People's Rep. of Korea, June 20, 2001.

M. Onoda and K. Kanbe,
Crystal structure and electronic properties of the $Ag_2V_4O_{11}$ insertion electrode,
J. Phys.: Condensed Matter, 13 (2001) 6675-6685.

M. Onoda and R. Arai,
The spin-gap state and the linear-chain state in $¥delta$-phase $Ag_xV_2O_5$ with a double-layered structure,
Journal of Physics: Condensed Matter, 13 (2001) 10399-10416.

A. Fujimori, M. Onoda et al,
Electronic structure of Mott-Hubbard-type transition-metal oxides,
J.Electron Spectroscopy and Related Phenomena, 117 (2001) 277-286.

K. Okazaki, A. Fujimori and M. Onoda,
Temperature-dependent electronic structure of VO_2 in the insulating phase,
J. Phys. Soc. Japan, 71 (2002) 822-825.

M. Nishikawa, Kazunaga Ono, Eiji Kita, H. Yanagihara, T. Erata and A. Tasaki
Magnetic properties and structures of Fe,Co/MgF_2 multilayered films.
J. Magn. Magn. Mater., 238 (2002) 91-100.

Tanimoto, H., Koda, Y., Sakai, S., Kita, E. and Mizubayashi, H.
Thermal Stability of Nanocrystalline structure FCC metals.
Proc. of the 22nd Riso Intern. Symp. on Materials Science : Science of Metastable and Nanocrystalline Alloys, Structure, Properties and Modelling, Riso National Laboratory, Roskilde, Denmark, 3-7 Sept., 2001, ed. by A.R. Dinesen et al., p. 401-406.

Sakai, S, Tanimoto, H, Otsuka, K., Yamada, T., Koda, Y., Kita E. and Mizubayashi, H.
Elastic behaviors of high density nanocrystalline gold prepared by gas deposition method
Scripta Mater. 45 (2001) 1313-1319.

ION BEAM APPLICATION

K. Sasa, H. Ohshima, Y. Yamato, T. Komatsubara, T. Katabuchi, K. Shima, K. Furuno, M. Kurosawa, N. Yanagisawa.
Hydrogen analysis of mineral samples at University of Tsukuba.
15th Intern. Conf. on Ion Beam Analysis (Cairns, Australia, July, 2001), Nucl. Instrum. Methods in Physics Research, B 190 (2002) 287-290.

6. THESES

Ph. D. Theses

T.Kurita	Developement of ECR ion source using liquid helium free superconducting solenoid coils.
K.Ono	Magneto-optical propeties and tunneling conduction of Fe,Co/MgF_2 Fe,Co/MgF_2 granular multilayers.

M. Sc. Theses

M.Ono	Azimuthal anisotropy of particle emission in Au +Au collisions at RHIC-PHENIX.
H.Tsuruoka	Development of collision detector for p+p collision measurements at RHIC-PHENIX.
K.Kanbe	Crystal structure and transport mechanism of $Ag_2V_4O_{11}$, and the application to the secondary ion battery.
T.Iiduka	The $^{6}Li(d,\alpha)^{4}He$ reaction at an incident energy of 90 keV.
S.Yokose	Lifetime measurement of the ground-state rotational band in ^{165}Ho.
A.Negishi	Formation Process of Transition Metal Silicide
A.Oyadomari	Basic properties of the Li ion battery system $Ag_{1+x}V_3O_8$
D.Kasuga	Electron correlation in the perovskite-type $SrVO_3$ system
K.Takeda	Electron loss from channeled ions
T.Nakanishi	Fabrication of microstructures in rutile TiO_2 single crystals by swift heavy-ion irradiation

7. SEMINARS

Date	Speaker and Title
2001	
June 6	T.R.Saitoh (Max-Planck-Inst. Heidelberg) ; Physics with gamma-rays; nuclear, nucleon and astrophysics.
June 13	I.Arai (Univ. of Tsukuba); Growth of nanostructures on surface.
June 20	K.Awazu ; Fabrication of microstructures in rutile TiO_2 single crystal using structural change induced by swift heavy-ion bombardment.
July 4	M.Kurosawa ; Quantitative trace element analysis of single fluid inclusion in quartz by PIXE.
July 11	Y.Nagashima (Univ. of Tsukuba) ; Accelerator Mass Spectrometry.
July 18	K.Kondo (TARA, Univ. of Tsukuba) ; Interaction in optical high field with ultrashort high peak power.
July 25	H.Kudo (Univ. of Tsukuba); Surface phenomena induced by bombardment of Fast ions.
Sept. 12	K.Sasa ; Report on Ion Beam Analysis 2001.
Sept. 19	Y.Aoki (Univ. of Tsukuna); What is the blanketting material of nuclear fusion reactor ?
Sept. 26	T.Hayakawa, T.Shizuma, T.Yamauchi, T.Arisawa (JAERI); Study plan of the nuclear astrophysics and nuclear isomer using photon sources.
Oct. 3	M.Tomizawa (KEK); Accelerators of JAERI/KEK high intensity accelerator project and JAERI/KEK RI beam facility based on ISOL.
Oct. 10	T.Sakae (Univ. of Tsukuna);Proton cancer treatment in Univ. of Tsukuba.
Oct. 24	T.Komatsuba (Univ. of Tsukuba); Report of the 1st Joint Meeting of the Nuclear Physics Division of APS and JPS, Hawaii.
Oct. 31	H.Miyatake (KEK) ; Joint RNB Project of KEK-JAERI.
Nov. 7	T.Kanai (HIMAC) ; Physical and biological background of heavy ion Radiotherapy.
Nov. 14	J.Kasagi (Tohoku Univ.);Nuclear resonances in nuclei studied with GeV photons.
Nov. 28	Y.Gono (Kyushu Univ.) ; Recent development of gamma-ray detection system.
Nov. 29	M.Yamaguchi (Univ. of Tsukuba); Development of proton polarimeter and breakup effects of deuterons in (d, p) reaction.
Dec. 5	Y.Kawachi (Univ. of Tsukuba); Real time measurement of implanted deuterons by using the ^{2}H(d,p)^{3}H reaction.
Dec. 12	T.Nishitani (JAERI); Nuclear fusion and Nuclear Data — ITER Project.
Dec. 19	T.Iizuka (Univ. of Tsukuba); The ^{6}Li(d, α)^{4}He reaction at an incident deuteron energy of 90 keV.
Dec. 20	S.Kubono (Tokyo Univ.); Explosion process of universe—— approach from nuclear physics.
Dec. 26	H.Yokomizo (JAERI); Outline and status of the high intensity proton accelerator Project.

2002

Jan. 9	M.Ogawa (Tokyo Inst. Technology); Increase of stopping power of high density plasma for fast heavy ions.
Jan. 23	M.Ono (Univ. of Tsukuba); Measurement of azimuthal anisotropy of particle emission in Au+Au collisions at RHIC-PHENIX. H.Turuoka (Univ. of Tsukuba); Design and manufacturing of the trigger and start counter for p + p collisions at RHIC-PHENIX.
Jan. 24	A.Negishi (Univ. of Tsukuba); The formation of transition metal silicide clusters observed by FT-ICR mass spectrometry. S.Yokose (Univ. of Tsukuba); Lifetime measurement of the ground-state rotational band in ^{165}Ho.
Jan. 30	T.Ishii (JAERI); Nuclear structure of neutron access Ni region using the deep-inelastic scattering. Y.Saito (JAERI); Acceleration of cluster ions to MeV energy region.
Feb. 13	S.Ezumi (Univ. of Tsukuba); QGP formation in heavy-ion collisions at SPS energies and recent news from RHIC experiments.
Feb. 27	N.Sakamoto (Nara Women's Univ.); Status of the tandem accelerator at NWU. Y.Shimizu (Kyushu Univ.) ; A tunneling phenomenon in nuclear structure.
March 6	T.Miyazaki (Univ. of Tsukuba); Emission of cluster from liquid
March13	M.Nakamura (Kyoto Univ.); Basics of the accelerator mass spectrometry
March20	Y.Iseri (Chiba-Keizai Junior Coll.); Determination of S17 based on CDCC analyses for ^{7}Be(d, n)^{8}B

8. SYMPOSIUM

Ion Beam Analysis of Materials

January 16, 2002

Tandem Accelerator Center, University of Tsukuba

Opening, *K.Shima (Univ. of Tsukuba)*
Reconsideration of the neutron doze in atomic bomb in Hiroshima, *K.Shizunma (Hiroshima Univ.)*
Ion-induced electron spectroscopy sensitive to the structure analysis, *H.Kudo (Univ. of Tsukuba)*
Behavior of hydrogen in carbon foils, *I.Sugai* (KEK)
Hydrogen analysis in rocks by ERDA using high-velocity proton beams, *T.Komatsubara (Univ. of Tsukuba)*
PIXE at NMCC, *K.Sera (Iwate Medical Univ.)*
Application of Ion beam analysis to mineral samples, *M.Kurosawa (Univ. of Tsukuba)*
Development and application of ion micro-beam technology at TIARA in JAERI, *T.Kamiya(JAERI Takasaki)*
Development of micro-beam facility for hydrogen analysis at UTTAC, *K.Sasa (University of Tsukuba)*
Closing remarks, *K.Furuno (Univ. of Tsukuba)*

9. LIST OF PERSONNEL

Accelerator Center

K. Furuno	Director, Professor
K.Shima	Associate Professor
T.Komatsubara	Assistant Professor
K.Sasa	Assistant Professor
T.Katabuchi	Research Associate
S.Ishii	Mechanical Technician
H.Kimura	Computer Technician
H.Oshima	Electric Technician
Y.Tajima	Mechanical Technician
T.Takahashi	Electric Technician
Y.Yamato	Electronics Technician
Li Tian-Xin	Research Fellow
K.Taga	Administrative Stuff

Steering Committee

K.Furuno	Chairperson, Tandem Accelerator Center
Y.Kajiwara	Inst. of Geoscience
R.Kanzaki	Inst. of Biological Sciences
T.Komatsubara	Tandem Accelerator Center,
H.Kudo	Inst. of Applied Physics
S.M.Lee	Inst. of Physics
M.Onoda	Inst. of Physics
R.Seki	Inst. of Chemistry
K.Shima	Tandem Accelerator Center
Y.Tagishi	Inst. of Physics
K.Yabana	Inst. of Physics
K.Yasuoka	Inst. of Basic Medical Sciences

Scientific Guests and Fellows

C.B.Moon	Hoseo Univ., Korea
Zhang Yu-Hu	IMP, Lanzhou
K.Awazu	National Lab. Advanced Industrial Science and Technology
M.Fujimaki	National Lab. Advanced Industrial Science and Technology
T.Nakanishi	Waseda Univ.
K.Nomura	Waseda Univ.
Y.Hata	JAERI
I.Daitou	Nagoya Univ.
Wang Li	Nagoya Univ.
T.Mizota	Tsukuba Nano-Tech.
H.Ishihara	KEK

Research Members

Inst. of Physics

Y.Aoki I.Arai S.Esumi K.Furuno T.Katabuchi
T.Komatsubara S.M.Lee Y.Miake N.Okumura M.Onoda
S.Satou K.Sasa Y.Tagishi T.Une S.Katoh

Inst. of Geoscience

R.Anma T.Katou M.Kurosawa

Inst. of Applied Physics

A.Uedono E.Kita H.Kudo K.Shima

Inst. of Chemistry

R.Seki

Inst. of Materials Science

H.Ikeda T.Koyano S.Kuroda H.Mizubayashi K.Takita
H.Tanimoto

College of Medical Technology and Nursing

Y.Nagashima

Tandem Accelerator Center

K.Itoh Li Tian-Xin

Venture Business Lab.

T.Miyazaki

Graduate Students

Doctoral Degree Programs in Physics

Ma Ying-Jun H.Sasaki N.Kawachi T.Jou M.Yamaguchi
Y.Sasaki S.G.Lee M.Imanaka K.Satoh J.Hirose
R.Arai M.Ono, H.Tsuruoka Y.Takechi J.Hasegawa
K.Takeda A.Kiyomichi S.Sakai A.Danmura T.Yamada
K.Sekine W.Iwazaki T.Suguri H.Masui M.Nakazumi

Doctoral Degree Programs in Engineering

K.Ono N.Umeda K.Suzuki S.Sakai N.Ookubo
Li Changqing

Doctoral Degree Programs in Education

T.Tsukada

Master's Degree Programs in Sciences and Engineering

S.Yokose T.Iizuka A.Negishi A.Oyadomari D.Kasuga
K.Kanbe Y.Kouda Y.Mihara T.Iida H.Satoh
C.Sakurai M.Ishizuka M.Aramaki K.Teranishi N.Umezawa
Y.Kuroki T.Banno I.Arano S.Numazawa

Doctoral Degree Programs in Agriculture Sciences

S.Kaburagi

Undergraduates

H.Arai
T.Ikeda
N.Kariya
K.Shiga
S.Takagi
A.Tanaka
H.Koubai
S.Miyasaka
M.Nagata
N.Yagi
T.Ohki
T.Suzuki
N.Yoshimaru
A.Hatanaka
M.Konno
T.Mutoh
T.Nomiyama
T.Matsuhiro
T.Harigae
H.naitoh
S.Kaminaga